Universitat de Girona

DENSITY FUNCTIONAL THEORY TO THE RESCUE OF TRANSITION-METAL CHEMISTRY

Frederico F. Martins

Universitat de Girona

DOCTORAL THESIS

DENSITY FUNCTIONAL THEORY TO THE RESCUE OF TRANSITION-METAL CHEMISTRY

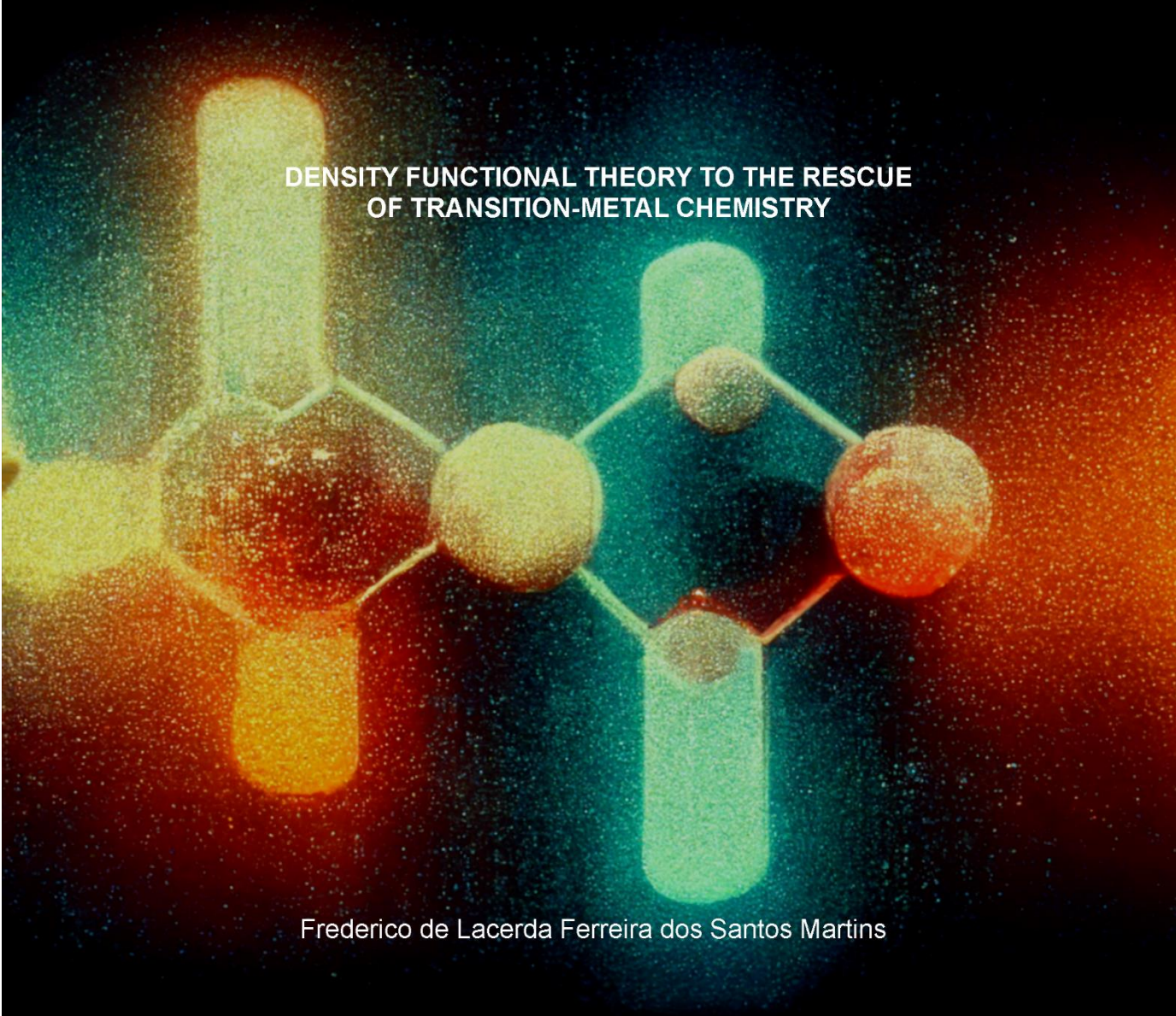

Frederico de Lacerda Ferreira dos Santos Martins

2023

DOCTORAL THESIS

DENSITY FUNCTIONAL THEORY TO THE RESCUE OF TRANSITION-METAL CHEMISTRY

Frederico de Lacerda Ferreira dos Santos Martins

2023

DOCTORAL PROGRAMME IN CHEMISTRY

Supervised by: Prof Dr Marcel Swart

Tutor: Prof Dr Marcel Swart

Presented to obtain the degree of PhD at the University of Girona

FULL LIST OF PUBLICATIONS

This thesis is based on the following publications:

a. **F. F. Martins**, S. Banerjee, L. Que, M. Swart, "A quantum-chemical view of the Sanders-Loehr series of diiron complexes", *to be submitted*.
b. **F. F. Martins**, M. Swart, "Electronic properties and redox chemistry of N-confused metalloporphyins", *Journal of Porphyrins and Phthalocyanines* **2023,** DOI: 10.1142/S1088424623500918.
c. **F. F. Martins**, P. Mondal, A. R. McDonald, M. Swart, "*In silico* optimization of a high-valent Ni oxidant", *to be submitted*.
d. W. A. Donald, S. Svane, R. O'Hair, **F. F. Martins**, M. Swart, C. J. McKenzie, "Gas phase structures of non-heme iron complexes and their intra- and inter-molecular reactivity", *to be submitted*.
e. **F. F. Martins**, V. Krewald, "Cooperative Dinitrogen Activation: Identifying the Push-Pull Effect of Transition Metals and Lewis Acids in Molecular Orbital Diagrams", *submitted to European Journal of Inorganic Chemistry, under review*.

Other publications:

1. R. T. Marques, **F. F. Martins**, D. F. Bekis, A. I. Vicente, L. P. Ferreira, C. S. B. Gomes, S. Barroso, V. Kumar, Y. Garcia, N. A. G. Bandeira, M. J. Calhorda, P. N. Martinho, "The halogen effect on the magnetic behaviour of dimethylformamide solvates in $[Fe(halide\text{-}salEen)_2]BPh_4$" *Magnetochemistry* **2022**, 8(12), 162, DOI: 10.3390/magnetochemistry8120162 (cover: https://www.mdpi.com/2312-7481/8/12).

2. A. Sánchez-González, N. A. G. Bandeira, I. K. Luzuriaga, **F. F. Martins**, S. Elleuchi, K. Jarraya, J. Lanuza, X. Lopez, M. J. Calhorda, A. Gil, "New Insights on the Interaction of Phenanthroline Based Ligands and Metal Complexes and Polyoxometalates with Duplex DNA and G-Quadruplexes" *Molecules* **2021**, 26(16), 4737, DOI: 10.3390/molecules26164737.

3. **F. F. Martins**, A. Sánchez-González, J. Lanuza, H. N. Miras, X. Lopez, N. A. G. Bandeira, A. Gil, "Probing the Catalytically Active Species in POM-catalysed DNA-model Hydrolysis", *Chemistry – A European Journal* **2021**, 27, 8977, DOI: 10.1002/chem.202004989 (cover: https://doi.org/10.1002/chem.202101593).

4. P. N. Martinho, **F. F. Martins**, N. A. G. Bandeira, M. J. Calhorda, "Spin Crossover in 3D Metal Centers Binding Halide-Containing Ligands: Magnetism, Structure and Computational Studies", *Sustainability* **2020**, 12(6), 2512, DOI: 10.3390/su12062512.

Outreach publications:

i. F. F. Martins, M. Swart, "Ferramentas Computacionais para o Estudo de Activação C-H com Catalisadores Biomiméticos", Boletim da Sociedade Portuguesa de Química 2022, 46, DOI: 10.52590/M3.P701.A30002512.

LIST OF ABBREVIATIONS

Abbreviation	Description
BDFE	Bond dissociation free energy
CCSD(T)	Coupled-cluster with perturbative triple excitations
COSMO	Conductor-like screening model
cPCET	Concerted proton-coupled electron transfer
CPCM	Conductor-like polarizable continuum model
DFA	Density functional approximation
DFT	Density functional theory
DLPNO	Domain based local pair natural orbital
EPR	Electron Paramagnetic Resonance
GGA	Generalized gradient approximation
GTO	Gaussian-Type Orbital
HAT	Hydrogen atom transfer
HF	Hartree-Fock
IBO	Intrinsic bond orbital
QUILD	Quantum-regions interconnected by local description
TD-DFT	Time-dependent DFT
TMetC	Transition-metal complex
sMMO	Soluble Methane MonoOxygenase
STO	Slater-type orbital
ZORA	Zeroth order regular approximation

Universitat de Girona

Prof. Marcel Swart, from the Universitat de Girona,

I DECLARE:

That the thesis entitled "Density Functional Theory to the Rescue of Transition-metal Chemistry", presented by Frederico de Lacerda Ferreira dos Santos Martins to obtain the doctoral degree, has been completed under my supervision and meets the requirements to opt for International Doctorate.

For all intents and purposes, I hereby sign this document.

Prof. Marcel Swart

Girona, July 2023

Para os meus Josézito e Aurélia.

"Each, according to his own inclination follows his own purpose, often in opposition to others; yet each individual and people, as if following some guiding thread, go toward a natural but to each of them unknown goal; all work furthering it, even if they would set little store by it if they did know it."

- Immanuel Kant, 1784

ACKNOWLEDGEMENTS

Quero começar por agradecer à minha família e amigos pelo seu apoio contínuo e sem os quais este doutoramento teria sido bastante penoso. Seria injusto nomear apenas alguns, mas segue um destaque especial para a minha família mais próxima e os babuínos do RSPT.

I am immensely grateful to my supervisor, Prof Marcel Swart, for providing me with invaluable resources, knowledge, and networking opportunities throughout my time as a PhD student. The work presented here is a unique combination of our complementary sets of skills, and I couldn't have achieved it without his guidance and support. I would also like to express my gratitude to Prof Vera Krewald, who graciously hosted me in Darmstadt and engaged in stimulating scientific discussions that broadened my understanding of CompChem.

Furthermore, I would like to acknowledge Dr Lorenzo D'Amore. His scientific expertise and life knowledge have been a significant source of inspiration and guidance throughout my PhD journey.

Last but not least, I would like to thank my colleagues from the IQCC and the Parc UdG. It has been an incredible experience to share this journey with such a talented and supportive group of people, and I will always cherish the memories and moments we shared.

Thank you all!

This PhD was possible due to the funding provided by Agencia Estatal de Investigación, AEI/MCIN (PRE2018-083883). The main fellowship and additional funds also from the AEI/MCIN (CTQ2017-87392-P, PID2020-114548GB-I00; 10.13039/501100011033) should be greatly acknowledged. The research stay in Darmstadt was possible thanks to the HPC3-Europa programme (INFRAIA-2016-1-730897, HPC17DSB70). Computational resources provided by the Universitat de Girona (via IQCC), the Barcelona Supercomputing Center, Technische Universität Darmstadt (Lichtenberg) and HLRS Stuttgart (Hawk; via HPC3-Europa) were equally key for the development of the present work.

INDEX

LIST OF FIGURES

LIST OF TABLES

SUMMARY

Density functional theory (DFT) was postulated almost 60 years ago and equipped chemists with a powerful framework to simulate, *in silico*, the behavior of chemical systems. Despite its widespread utility, DFT methods have encountered difficulties in accurately modeling the reactivity of transition-metal complexes, due to, e.g., their unique open-shell electronic structures, multireference character and associated consequences. However, these complexes play a crucial role as essential constituents of materials with exceptional functionality, enabling the execution of complex reactions that would otherwise be exceedingly challenging, akin to those facilitated by enzymatic cofactors.

Remarkably, this work unintentionally demonstrates the capabilities of DFT to overcome the existing obstacles posed by transition-metal chemistry. In Chapter 4, we explore the relationship between vibrational frequencies, structure, and magnetic properties in oxo-bridged diiron complexes reminiscent of the cofactor found in the soluble methane monooxygenase enzyme. Chapter 5 employs DFT-based techniques to locate electrons in highly delocalized π-systems of metalloporphyrins, shedding light on their influence on the Soret band of these complexes. Chapter 6 emphasizes the significance of the initial guess in studying reactivity, as we encountered challenges in achieving the desired C-H activation reactivity within a Nickel-halide complex, likely due to an erroneous potential energy surface minimum obtained. In Chapter 7, we demonstrate the usefulness of time-dependent DFT calculations in accurately predicting the UV-Visible spectra of high-valent iron-oxo

complexes, enabling their identification. Lastly, Chapter 8 investigates cooperative molecular nitrogen activation using a transition-metal Rhenium complex and Lewis acids, providing insights into the observed phenomena through the lens of molecular orbital theory.

Overall, this thesis aims to showcase the enduring relevance and practicality of DFT methods in contemporary research. While employing DFT to elucidate chemical problems, we remain aware of its limitations and often employ alternative approaches to mitigate these challenges.

RESUM

La teoria del funcional de densitat (DFT, per les seves sigles en anglès) va sorgir fa aproximadament 60 anys, dotant els químics d'un marc computacional poderós per simular el comportament dels sistemes químics en un entorn virtual. Malgrat la seva àmplia utilitat, els mètodes de DFT han trobat dificultats per modelar adequadament la reactivitat dels complexes de metalls de transició, a causa de, e.g., les seves estructures electròniques de capa oberta, caràcter multireferència i les conseqüències associades. No obstant això, aquests complexes juguen un paper crucial com a components essencials de materials amb funcionalitat excepcional, permetent dur a terme reaccions complexes que, d'altra manera, serien extremadament desafiants, similars a les facilitades pels cofactors enzimàtics.

D'una manera sorprenent, aquest treball demostra de manera fortuïta la capacitat dels mètodes DFT per superar els obstacles existents en la química dels metalls de transició. Al Capítol 4, explorem la relació entre les freqüències vibracionals, l'estructura i les propietats magnètiques dels complexes de di ferro amb ponts oxo, semblants al cofactor present en l'enzim monooxigenasa soluble en metà. Al Capítol 5, utilitzem tècniques basades en DFT per localitzar els electrons en sistemes π altament deslocalitzats de metal·lo porfirines, aclarint la seva influència en la banda Soret d'aquests complexes. El Capítol 6 posa de relleu la importància de l'estimació inicial en els estudis de reactivitat, ja que ens enfrontem a desafiaments per obtenir la reactivitat desitjada de l'activació de l'enllaç C-H en un complex níquel-halur, probablement a causa d'un mínim espuri en la superfície d'energia potencial obtinguda. Al Capítol 7, demostrem la utilitat dels càlculs de DFT dependents del temps per obtenir

amb precisió els espectres UV-Visibles de complexes de ferro-oxo de valència alta, permetent la seva identificació. Finalment, el Capítol 8 explora l'activació cooperativa del nitrogen molecular amb un complex de reni de metall de transició i àcids de Lewis, explicant els fenòmens observats des del punt de vista de la teoria dels orbitals moleculars.

En general, aquesta tesi pretén posar de manifest la vitalitat i la rellevància contínua dels mètodes de DFT en la recerca actual. Emprant aquests mètodes per esbrinar problemes químics, som conscients de les seves limitacions i sovint recorrem a solucions alternatives per superar aquests desafiaments.

RESUMEN

La teoría del funcional de la densidad (DFT, por sus siglas en inglés) surgió hace aproximadamente 60 años, proporcionando a los químicos un marco computacional poderoso para simular el comportamiento de los sistemas químicos en un entorno virtual. A pesar de su amplio uso, los métodos de DFT han enfrentado dificultades para modelar adecuadamente la reactividad de los complejos de metales de transición, debido a, e.g., sus estructuras electrónicas abiertas, caracter multireferencia y las consecuencias asociadas. Sin embargo, estos complejos desempeñan un papel crucial como constituyentes esenciales de materiales con funcionalidad excepcional, lo que permite llevar a cabo reacciones complejas que de otro modo serían extremadamente desafiantes, similares a aquellas facilitadas por cofactores enzimáticos.

De manera sorprendente, este trabajo demuestra de manera fortuita las capacidades de los métodos DFT para superar los obstáculos existentes en la química de metales de transición. En el Capítulo 4, exploramos la relación entre las frecuencias vibratorias, la estructura y las propiedades magnéticas en complejos de di hierro con puentes oxo, similares al cofactor presente en la enzima mono oxigenasa soluble en metano. El Capítulo 5 utiliza técnicas basadas en DFT para localizar electrones en sistemas π altamente deslocalizados de metal porfirinas, arrojando luz sobre su influencia en la banda Soret de estos complejos. El Capítulo 6 enfatiza la importancia de la suposición inicial en el estudio de la reactividad, ya que enfrentamos dificultades para lograr la reactividad deseada de activación de enlaces C-H en un complejo de níquel-haluro, probablemente debido a un mínimo espurio en la superficie de energía potencial obtenida. En el Capítulo 7, demostramos la utilidad de los

cálculos de DFT dependientes del tiempo para predecir con precisión los espectros UV-Visibles de complejos de hierro-oxo de alto valencia, lo que permite su identificación. Por último, el Capítulo 8 investiga la activación cooperativa de nitrógeno molecular mediante un complejo de renio de metal de transición y ácidos de Lewis, proporcionando información sobre los fenómenos observados desde la perspectiva de la teoría de orbitales moleculares.

En general, esta tesis tiene como objetivo mostrar la relevancia y practicidad duraderas de los métodos de DFT en la investigación contemporánea. Al emplear la DFT para dilucidar problemas químicos, somos conscientes de sus limitaciones y a menudo utilizamos enfoques alternativos para mitigar estos desafíos.

Chapter 1

Introduction

1. INTRODUCTION

1.1. Transition-metal chemistry and society

Transition-metal complexes (TMetCs) – molecules that arise upon mixed (ionic and covalent) binding between transition elements and ligands – have proven themselves useful in solving many of the critical problems of human society. Their special reactivity and electronic properties that arise from the *d* (often unpaired) electrons of the metal ion and the tunable ligand field that affects their distribution and energies render this class of molecules ideal to serve as functional component in novel materials or catalytic species for intricate reactions that involve the functionalization of otherwise inert bonds. This is well evidenced as TMetCs are found in many IUPAC "Top Ten Emerging Technologies in Chemistry"[1, 2] solutions (sustainable ammonia,[3] solar fuels,[4] fluorescent sensors,[5] MOFs,[6] to name a few).

Nature, with its several years old potential well,[7] also found transition-metal catalysts to be the most efficient in performing many of the life-sustaining reactions such as the oxidation of strong C-H bonds, and these are found in enzymatic cofactors.[8] One approach to make new able catalysts is to mimic the metal environment in such enzymes, while trying to dispose of the large amino acid backbone which has mostly a directing function via stereochemical hindering or weak electrostatic interactions. However, in order to develop such biomimetic catalysts, the mechanism of operation of these enzymes needs to be exceptionally well known and it is extremely hard to study with current experimental techniques[9] due to the transient lifetime of the intermediates and

transition states involved. Hence, the current method of choice is to use spectroscopic techniques to register the spectra of these transient chemical species and combine this information with a quantum chemical method such as Density Functional Theory[10] (DFT) to correctly identify their geometry and electronic properties (Figure 1.1).

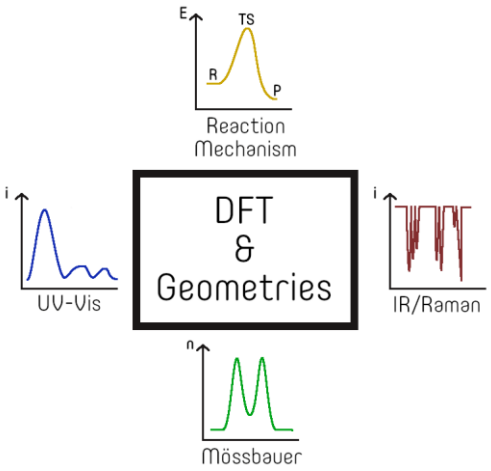

Figure 1.1 Capabilities of DFT in transition-metal chemistry that will be used throughout the present thesis.

One very good example of the usefulness of these processes arose from the study of the soluble methane monooxygenase (sMMO) enzyme.[11] It is known for converting methane into methanol, meaning it can oxidize even one of the strongest of C-H bonds. The oxidation of methane, in particular, is extremely important for the petrochemical industry, and thus for society, as the energy contained in the gas is much easier and cost-efficient to transport over large distances if it is converted to a liquid form.[12] The mechanism for this reaction

involves the formation of high-valent iron intermediates upon oxygen – readily available in blood, but also in the atmosphere – activation. This has prompted chemists to synthesize transition-metal compounds that mimic the cofactor in such enzymes to obtain a molecule capable of performing the same conversion.[13, 14] DFT has been important in the description of the reactivity of these synthetic analogues as has been demonstrated in recent work by Guo, Swart, Que and coworkers.[15] The dioxygen activation step of the reaction carried out by sMMO was known to generate a peroxodiiron(III) species (P) from previous Electron Paramagnetic Resonance (EPR)[16] and Mössbauer[17] studies. However, the active species for C-H oxidation was believed to be a so-called "diamond core" diiron(IV) complex (Q)[18] and the transformation from P to Q was unknown.

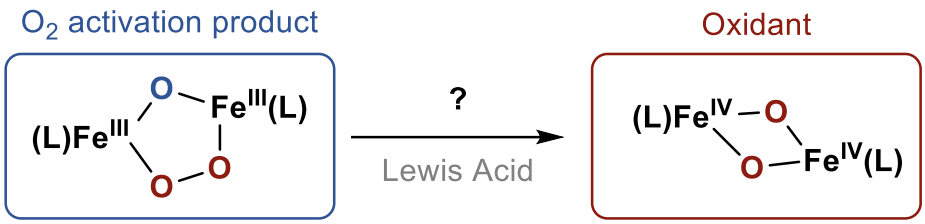

Scheme 1.1 Trapped intermediates P and Q of the oxidation reaction carried out by sMMO.

While a few synthetic models for nonheme dioxygen activation enzymes had been obtained in the past,[13, 19, 20] none showed this P to Q conversion. In this work, the experimental team was successful in synthesizing a P analogue from the Fe(II) complex $[Fe^{II}(Me_3NTB)(CH_3CN)](CF_3SO_3)_2]$ (Me_3NTB = tris((1-methyl-1H-benzo[d]imidazol-2-yl)methyl)amine) that bears a rigid

tetradentate amine ligand. Q was obtained for the first time in the laboratory upon treatment of that P analogue with scandium triflate ($Sc(OTf)_3$, Scheme 1.1). The identification of both species P and Q resulted from a combination of spectroscopic methods and DFT calculations. When experimental efforts alone were deficient in explaining this P to Q conversion, DFT showed that the Lewis Acid was more prone to interacting with the peroxo-bridge, leaving the oxygen labeled in blue in Scheme 1.1 free for reduction and facilitating a putative peroxo rotation that would result in Q. The ca. 47 kcal mol^{-1} difference between the interaction of the scandium ion with the oxo or peroxo bridges was rationalized with the analysis of the corresponding steric interactions.

The strategy elucidated here has been used to find able synthetic catalysts for many oxidation reactions,[21] including with first-row metals other than iron[22-24] such as manganese,[25] copper[26] and cobalt.[27]

1.2. TMetC Spectroscopy with DFT

DFT is extremely useful as many intermediates and transition states live long enough to be characterized experimentally via spectroscopic techniques, but not long enough for a proper structural (crystallographic) characterization. As DFT allows for the simulation of various spectra provided a molecular structure,[28, 29] it can thus act as a bridge between spectrum and structure for the design of appropriate mechanistic proposals. The calculation of harmonic vibrational frequencies leads to the simulation of Raman and Infra-red spectra.[30] Mössbauer parameters can be estimated from the electron densities at the Mössbauer-active metal centres.[31] The time-dependent formulation of

DFT (TD-DFT) allows for the computation of electron excitation energies and thus of the simulation of UV-Visible electronic spectra.[32] Hence, the combination of all of these techniques provides a powerful tool to understand otherwise elusive chemical phenomena and is, nowadays, indispensable in transition-metal chemistry.[33-37]

To showcase the capabilities of DFT to solve spectroscopy-related problems, three examples will be presented here with varying metal environments (Figure 1.2).

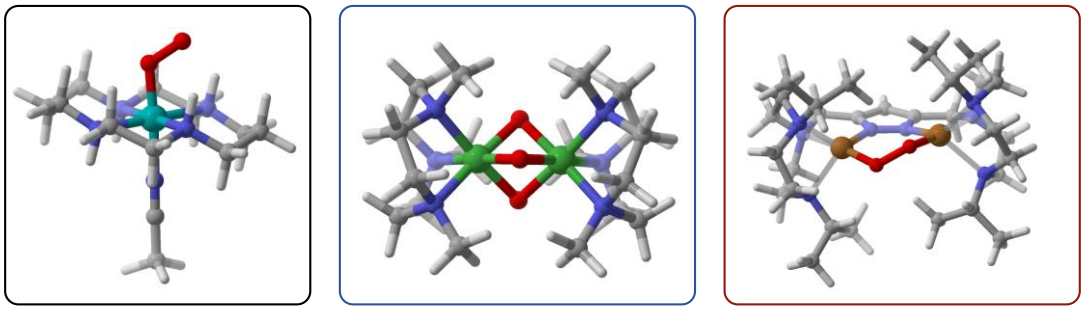

Figure 1.2. DFT structures for the Cyclam-Fe^{III}-superoxo (left),[38] 1,4,7-trimethyl-1,4,7-triazacyclononane-diNi^{IV}-oxido (center)[39] and tris(2-pyridylmethyl)amine-diCu^{II}-peroxo (right)[40] complexes.

The first example, which is not far from the sMMO synthetic analogue explored in the first section, is that of the study of the Fe(II)-cyclam synthesized by Ray and coworkers.[38] This complex that was capable of activating O_2, generating an Fe^{IV}=oxo species, was characterized using several spectroscopic techniques (UV-vis, Mössbauer) and single crystal X-ray crystallography, however a transient intermediate detectable at 253.15 K was impossible to crystallize

(Figure 1.2, left). The structural and spectroscopic data of the stable intermediate was used to validate the DFT method that was later used to identify the transient intermediate. They were able to obtain the correct ground-state (by a ca. 17 kcal mol^{-1} discrepancy), bond distances (Table 1.1), stretching frequencies (shifted by 24 cm^{-1}) and Mössbauer parameters (0.03 and 0.68 mm s^{-1} differences for the isomer shift and quadrupole splitting respectively). The same computational method was then used to identify the elusive compound as an antiferromagnetically coupled Fe^{III}-superoxo species. The end-on binding mode of the superoxo moiety was only possible to identify via the DFT optimization of the different options.

Table 1.1. Comparison between the bond lengths obtained for an Fe(IV)-oxo and a putative Fe(III)-superoxo species with two experimental techniques and a DFT methodology.[38]

	Compound	**Bond**	**Length (EXAFS) / Å**	**Length (Crystal) / Å**	**Length (DFT) / Å**
Validation	Fe^{IV}-oxo	Fe=O	1.67	1.70	1.64
		Fe-N_{MeCN}	2.10	2.04	2.07
		Fe-N_{Ligand}	2.01	2.00	2.03
		Fe-C_{Ligand}	2.87	2.91	2.89
Test	Fe^{III}-superoxo	Fe-O(-O)	1.74	-	1.76
		Fe(-O)-O	2.79	-	2.66
		Fe-N_{MeCN}	2.00	-	1.99
		Fe-N_{Ligand}	2.00	-	2.03
		Fe-C_{Ligand}	2.94	-	2.92

Now that the efficacy of such theoretical methods has been shown for the infamous iron, one can move towards other metals. Browne and coworkers reported[39] the formation of a Ni oxidant upon treatment of the tri-chloro bridged $[(L)_2Ni(II)_2(\mu\text{-}Cl)_3]Cl\cdot(H_2O)_5$ complex, L = 1,4,7-trimethyl-1,4,7-triazacyclononane, with sodium hypochlorite. This oxidant species could be detected by UV-vis, resonance Raman, Nuclear magnetic resonance, EPR and X-ray absorption spectroscopies, but quickly decayed to two mononuclear Ni^{II} complexes with three acetonitrile ligands and was thus extremely hard to crystallize. While it was clear that the chloride bridges had somehow been substituted by some oxygen-containing moiety, the nature of such bridges (oxido vs peroxo vs oxo) and the electronic configuration of the metals was unidentified. DFT calculations showed that the tris-μ-oxido-diNi^{IV} complex (Figure 1.2, center) was 4.46 and 42.2 kcal mol^{-1} more stable than the peroxy(diNi^{III})-and mono-μ-oxo(diNi^{III})-bridged analogues, respectively. The identification of the transient oxidant as the high-valent diNi^{IV} species was further confirmed by an excellent agreement between the Raman spectra simulated by DFT and that obtained experimentally. The results of the mixed labeling experiments and DFT with varying ratios of ^{16}O:^{18}O can be observed in Table 1.2.

Table 1.2. Comparison between resonance Raman peaks obtained by DFT and mixed labeling experiments with varying oxygen isotope ratios.[39]

	Isotope ratio $^{16}O:^{18}O$				
	3:0	**0:3**	**1:2**	**2:1**	
Experiment	631	623	613	599	Raman shift
DFT (diNi^{IV})	638	630	622	609	/ cm^{-1}

The final example comes from a study on the binding of alkali metals to a μ-1,2-peroxo dicopper(II) complex (Figure 1.2).[40] DFT calculations were first successful in predicting an unexpected unusually high affinity of the Lewis basic peroxo to the Li^+ cation which was later confirmed as the compound was able to abstract this alkali metal when encapsulated in 15-crown-5. TD-DFT results were then shown to match the experimentally obtained UV-vis spectrum and as such the molecular orbitals involved in the excitations were identified. The vibrational frequencies obtained via DFT were key in identifying which vibrational modes were affected by the alkali metal-peroxo interaction which turned out to be the O-O stretching. The DFT calculated Raman peaks were merely 17-29 cm^{-1} apart from the experimental results and the oxygen isotope-induced shifts were calculated with even greater accuracy, of 4-10 cm^{-1}. Additionally, the difference in energy between the two possible spin states (S=0 and S=1) was also obtained and a few Generalized Gradient Approximation functionals were benchmarked (a smaller set can be found in Table 1.3). OPBE was the only functional capable of correctly assigning the spin state for all diCu-alkali metal adducts but failed to predict the spin-state for the bare complex. This is not surprising as DFT calculations have an accuracy of 1-2 kcal mol^{-1} and the spin-state splitting here was of ca. 1 kcal mol^{-1}. The density functional

approximation with mPW exchange and Perdew correlation was found to perform the worst.

Table 1.3. Benchmarking of Density Functional Approximations for the calculation of spin-state splittings in the diCu-peroxo complex and corresponding alkali metal adducts.

	$E_{(S=0)}$-$E_{(S=1)}$ / kcal mol^{-1}		
Functional	**diCu-peroxo**	**diCu-peroxo-Li$^+$**	**diCu-peroxo-Na$^+$**
OPBE	-0.77	0.25	0.06
S12g	-1.15	0.14	-0.11
mPWxPc	-1.56	-0.20	-0.38

These recent examples were included here to show that DFT is still a powerful tool to tackle transition-metal spectroscopy problems and will very likely continue to be used in the future.

1.3. Reaction mechanisms with DFT: C-H activation

DFT is also useful for the determination of reaction mechanisms as it allows for the identification of a reasonable thermodynamic (reaction energies, ΔG) and kinetic (reaction barriers, $\Delta G^{\ddagger}$) path from reactants to products upon evaluation of the relative energies of the calculated species.[41] Although transition-state theory is extremely useful for the description of most multiple-step chemical reactions that occur, especially in solution, it does not enable the rationalization of the chemical phenomenon associated with the infamous metal-catalyzed C-H bond functionalization (and other inert bonds) as the different possible mechanisms occur over the same reactants, transition-state

and products. Other analytical methods are thus required to circumvent this limitation and lead to a faster and inexpensive screening of future potential industry-scalable catalysts.

While it is usually clear when a C-H bond is broken and the activation occurs in a single kinetic step, its mechanism is often arguable or elusive because the electron made available from the C-H breakage can either contribute to the new X-H bond that is formed (hydrogen atom transfer, HAT) or be transferred to the activating metal instead (concerted proton-coupled electron transfer, cPCET).[42] Formally, HAT involves the abstraction of a hydrogen radical from donor to acceptor (proton) and in cPCET a proton and an electron are transferred concomitantly but separately i.e. to different acceptors. The controversy over the nomenclature of these reactions is out of the scope of the present thesis and will not be addressed.

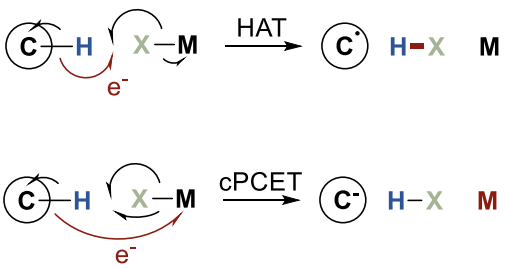

Scheme 1.2. Hydrogen atom transfer and (concerted) proton-coupled electron transfer mechanisms with metal (M) complexes. X is a highly electronegative moiety.

The experimental method of choice to distinguish between both mechanisms is the analysis of the kinetic isotope (hydrogen/deuterium) effect[43] as HAT reactions should have a rate constant dependance of 0.5 of the concentration

of the substrate, according to Marcus theory.[44, 45] These burdensome experiments, however, may easily be substituted by DFT calculations which allow the user to follow the electron flow along the reaction. This can be performed through the analysis of the charge displacements[46] in the relevant atoms or of the localized orbitals along the reaction coordinate.[47] The efficacy of these methods was proven for the same enzyme-catalyzed reactions, albeit being developed by different authors: the taurine dioxygenase and the lipoxygenase oxidation reactions, and they are good benchmarks as they seem to happen via different pathways. While the former is thought to occur via HAT,[48] the latter should follow a cPCET mechanism.[49]

Klein and Knizia showed[47] how the localized Intrinsic Bond Orbitals (IBOs) can be used to aid with this problem. They identified the α and β orbitals involved and followed them along the reaction coordinate. As can be observed in Scheme 1.3, in the case of a HAT mechanism, the orbital is located at/near the transferred hydrogen at all times, while during a cPCET reaction the orbital moves from the hydrogen (reactant) to the metal-oxo bond (transition state) and finishes at the metal atom (product).

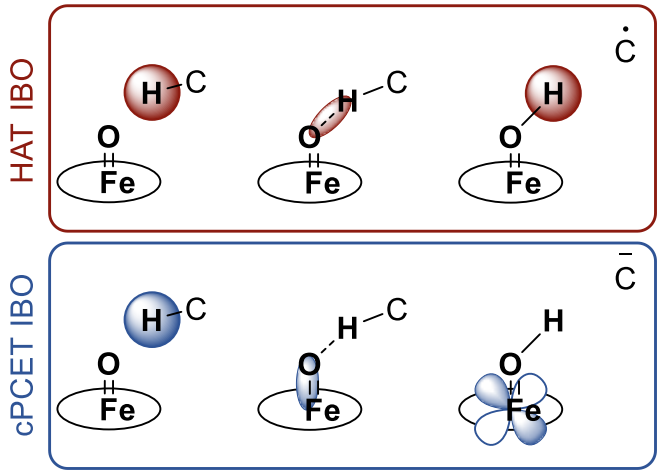

Scheme 1.3. IBO representation for a hydrogen abstraction by Fe=O via HAT (top) and cPCET (bottom) along the reaction coordinate.

This methodology has been used to rationalize the C-H activation mechanism of an oxocobalt(III) complex[50] and a Co_4O_4 cubane cluster,[51] but perhaps the most interesting case study was that of a copper(III)-hydroxo compound, studied by Cramer, Tolman and coworkers,[52] that the authors noticed could perform the hydrogen abstraction via both mechanisms, depending on the substrate. The proton of 9,10-dihydroanthracene was removed via HAT and that of 2,4,6-tri-*tert*-butylphenol via cPCET by the same metal complex, as acceptor.

1.4. Reaction mechanisms with DFT: N_2 activation

A different chemical bond which is as important as it is hard to break is the triple covalent bond of the nitrogen molecule that is abundantly found in the atmosphere of our planet. Its strong nature derives from its lack of dipole moment, strong π and σ bonding interactions that lead to a dissociation

enthalpy of ca. 225 kcal mol^{-1} and high ionization potential of ca. 16 eV.[53] This great challenge is worth undertaking, however, as nitrogen reduction is necessary for the generation of ammonia and other feedstock for the pharmaceutical industry.

Ammonia is produced today via the Nobel-prize winning Haber-Bosch process,[54] which relies on huge amounts of limited and polluting fossil energy.[55] It is required at such a scale, that its production is responsible for approximately two percent of the total energy consumption in the world.[56] The fact that this huge amount of energy consumed nowadays is reliant on fossil fuels led IUPAC to choose "sustainable ammonia" as a top ten emerging technology in chemistry, in 2021.[2]

One of the ways of achieving this sustainable production of ammonia is to use first-row transition-metal complexes to capture nitrogen from the air and promote its reduction to ammonia and other amines or hydrazine. Thermal activation of N_2 – decrease in N-N bond strength as confirmed by vibrational spectroscopy – with TMetCs is correlated with the acidity of the metal and involves the shift of electron density from the metal to the nitrogen ligand, upon coordination.[57] However, photochemical[58] and electrochemical[36] activation has also been successfully performed. They stem from one of two processes, or ideally the combination of both: population of N-N antibonding orbitals or depopulation of N-N bonding orbitals. These processes occur with a light stimulus in the case of the former and application of an electric potential in the latter. However, these are mostly conceptual studies, and consistent N_2 activation and functionalization is far from an industrial application today.

Unsurprisingly, the idea of using TMetCs for nitrogen functionalization again came from Nature. Researchers noted that nitrogenase enzymes were capable of breaking the N-N bond at mild conditions and identified the active center of the enzyme to be a cofactor containing iron, sulfur and molybdenum.[59] This prompted the development of synthetic clusters with these metals.[60] A few selected examples of nitrogen activating molecules or nitrogen reduction catalysts can be found in Figure 1.3, however the work of many others should be equally highlighted.[33, 61-64]

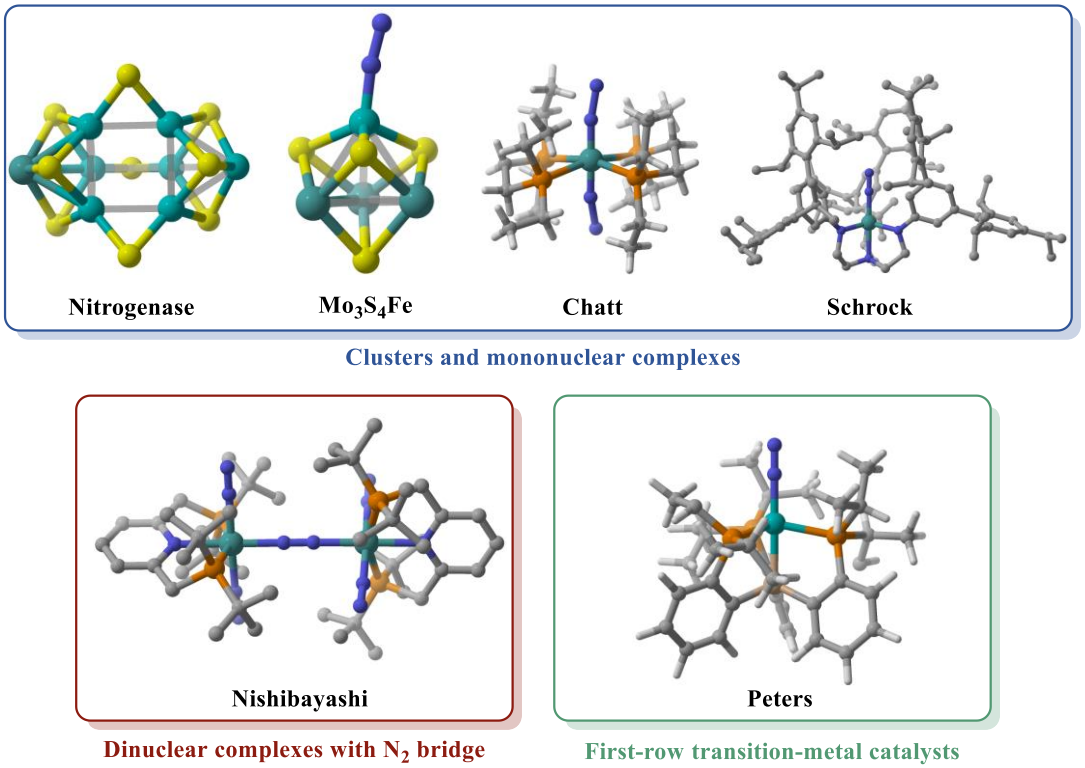

Figure 1.3. Nitrogen activating molecules. Top, from left to right: FeMo nitrogenase cluster,[65] FeS synthetic cluster,[60] Chatt[66] and Schrock catalysts.[67]Bottom: Nishibayashi[68] and Peters catalysts.[69, 70]

DFT has also been useful to explain nitrogen reduction reactivity. Krewald has authored extensive literature[58] on the rationalization of the photochemical activation of N_2. Ye and coworkers published a study[70] where DFT was used to explain the unusual Mössbauer shifts measured experimentally[71] upon reduction of the Peters catalyst. They found that a reduction in Fe-N bond length was due to unexpected ligand to metal π-backbonding. Vyas and coworkers published two[72, 73] computational studies using a standard DFT methodology and transition-state theory to study the successive protonation and reduction steps of nitrogen reduction by iron catalysts.

Chapter 2

Objectives

2. OBJECTIVES

The overall objective of the present work is to provide examples of workflows using DFT to solve transition-metal chemistry problems, probing its accuracy and versatility. In each of the separate chapters, different topics were approached with this objective in mind:

Chapter 4 – Spectroscopy to structure in oxo bridged iron dinuclear compounds:

- Understand the nature of the apparent relationship between structure and vibrational spectra of di-iron oxo bridged complexes
- Provide a means of predicting relevant properties (geometrical and magnetic features) in such complexes from their vibrational spectrum

Chapter 5 – Electronic properties of N-confused metalloporphyrins:

- Demonstrate that DFT can describe strongly delocalized systems
- Study the effect of N-confusion and metal coordination on porphyrinic systems

Chapter 6 – Ni-halide C-H activation:

- Show how DFT can provide insight into the mechanism of reactions involving proton transfer (HAT/CPET)
- Predict, from kinetic parameters, the behavior of analogous compounds

Chapter 7 – High-valent Iron species characterization:

- Identify key species in gas phase reactions from thermodynamic parameters and spectroscopy (UV-Vis, IR)

Chapter 8 – Cooperative effects between transition-metals and Lewis acids for the activation of dinitrogen:

- Elucidate the role of electron-withdrawing species in nitrogen activation via analysis of molecular orbitals and thermodynamic parameters

Chapter 3

Methodology

3. METHODOLOGY

3.1. Computation in chemistry

As mentioned beforehand, the description of chemical systems via computational methods has many advantages. However, the choice of methodology is not trivial. A recent Perspective[74] has tackled precisely this issue and attributed the chaos to the large number of options available nowadays and the antisymmetric property of wave functions, the main contributor to computing cost. This contradicts the idea that, for instance, DFT is a "black-box" method where the user needs no prior physical-chemistry knowledge to obtain qualitative or quantitative information on the chemical systems they intend to study. While others have tried to review and improve the method that is considered to be "failproof" at a certain moment in time,[75] it seems more sensible to let experts find and use the appropriate method for the specific system and property that need to be interrogated, at least until the true functional is discovered.

While the heaven of chemical accuracy is generally agreed to be the Coupled-Clusters theory with triple excitations (CCSD(T)),[76] with an error rivaling that of experimental techniques, it is hardly applicable for most interesting molecules due to its high computational cost, that increases exponentially with total number of electrons. A domain-based local pair natural orbital analogue (DLPNO-CCSD(T))[77] that is capable of recovering most of the CCSD(T) correlation energy and thus of delivering extremely accurate results at a cost comparable to DFT has been developed recently, but it is yet to find a general use in the chemistry community. Therefore, the large majority of the chemistry

performed on CPUs to date resorts to the decades-old DFT, and its use continues to increase every year (Figure 3.1).

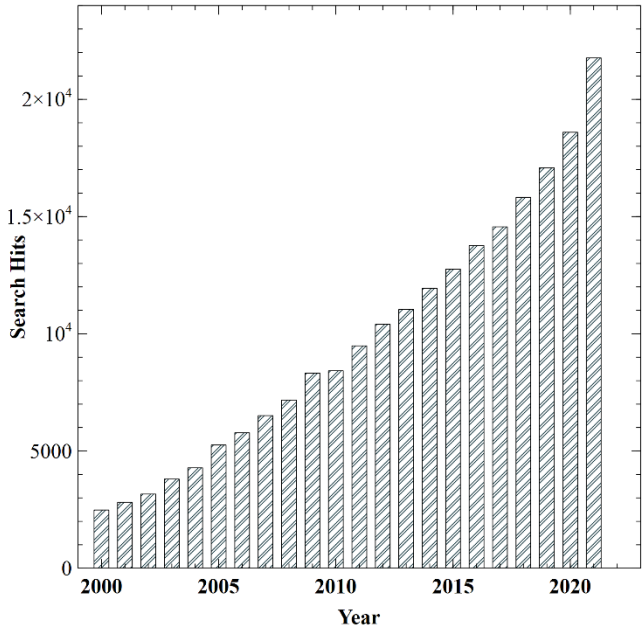

Figure 3.1 Rise of documents found in the Web of Science with "Density functional theory" as Topic. For comparison, "CCSD" returns 560 hits in 2021, and is not systematically increasing throughout the years.

DFT is an exact theory, based on the Kohn-Sham equations, that perfectly describes the ground state of a multi-electron (chemical) system from its density.[78] The expression for the many electron Hamiltonian is the following:

$$\hat{H} = \sum_{i=1}^{N} \left[\frac{1}{2}\nabla_i^2 + v(r_i)\right] + \frac{1}{2}\sum_i \sum_{i \neq j} \frac{1}{|r_i - r_j|} + V_{nn} \quad (3.1.1)$$

Where the first operator corresponds to the electronic kinetic energy and the electrostatic interaction between electrons and nuclei, the second operator to the electrostatic interaction among electrons and V_{nn} to the electrostatic potential among the nuclei. The kinetic energy of the nuclei is ignored due to their much greater relative mass, according to the Born-Oppenheimer approximation. The work of Thomas and Fermi, which was later improved into the theorem by Kohn and Sham that is used today, allowed for the mathematical transformation of the *N*-electron wave function with the Hamiltonian of Eq. 3.1.1 into a simpler formulation for the ground-state that depends solely on the electron density, ρ_σ(r):[79]

$$\left[\frac{1}{2}\nabla^2 + \upsilon(\boldsymbol{r}) + \int d\boldsymbol{r}' \frac{\rho(\boldsymbol{r}')}{|\boldsymbol{r}' - \boldsymbol{r}|} + \upsilon_{xc}^{\sigma}(\boldsymbol{r})\right]\psi_{\alpha\sigma}(\boldsymbol{r}) = \varepsilon_{\alpha\sigma}\psi_{\alpha\sigma}(\boldsymbol{r}) \quad (3.1.2)$$

Hence, the energy of such a system can be calculated via an integration over the whole space (**r**), found in Equation 3.1.3:

$$E = \sum_{\sigma}\int d\boldsymbol{r}\,\tau_\sigma + \int d\boldsymbol{r}\rho(\boldsymbol{r})\,\upsilon(\boldsymbol{r}) + \frac{1}{2}\int d\boldsymbol{r}\int d\boldsymbol{r}'\frac{\rho(\boldsymbol{r})\rho(\boldsymbol{r}')}{|\boldsymbol{r}' - \boldsymbol{r}|} + E_{xc} + V_{nn} \quad (3.1.3)$$

Where τ_σ is the kinetic energy operator, and the electrostatic interactions involving electrons now take into account the electron density (ρ). While all of the terms in Equation 3.1.3 are exact and computable, there is one whose correct formulation is yet to be found and this is the exchange-correlation term (E_{xc}). As such, approximations need to be carried out to reproduce experimental results. These are known as density functional approximations (DFAs). We can thus envision a categorization of such DFAs according to the complexity and, hopefully, accurate description of the E_{xc} term such that better results are obtained. This is the so-called Jacob's ladder of DFAs (Figure 3.2).[78]

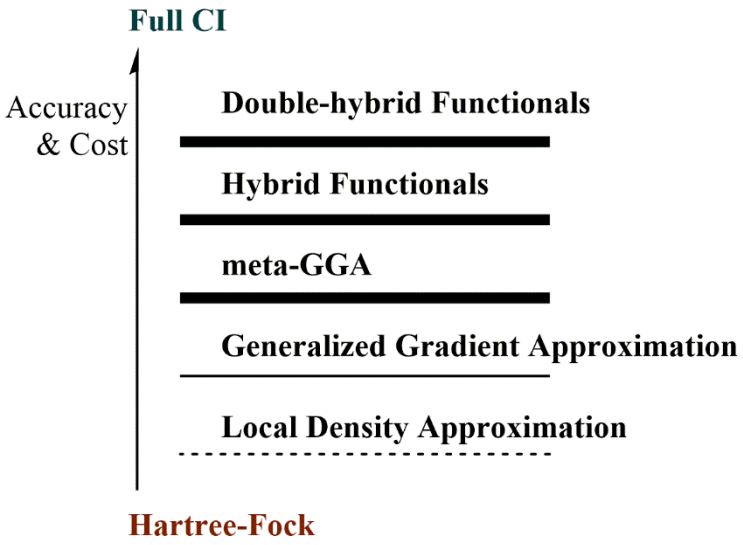

Figure 3.2 Jacob's ladder of DFAs.[80]

While the DFAs from Jacob's ladder respect physical constraints to the localization of the electronic density, some DFAs are obtained via

parametrization of the E_{xc} term to fit known data (either experimental or by comparison to a higher-level computational method such as CCSD(T)). One of such examples involves the mixing of Hartree-Fock (HF) exchange in an arbitrary weight that better matches experiment, giving rise to Hybrid functionals. Several authors have provided guidelines on how to make the best of the potential behind DFAs, while navigating its shortcomings.[80-82]

Here, a Generalized Gradient Approximation-based (GGA) functional was selected: S12g.[83] This DFA combines the uniform electron gas-derived electronic correlation energy of PBE[84, 85] with an expression for the exchange energy that uses empirically obtained coefficients to improve the Dirac exchange term – an idea based on the formulation of OPTX by Handy and Cohen[86] – granting it a description capability of spin state and reaction barriers comparable to OPBE,[87] while including the D3 dispersion correction by Grimme and coworkers by design[88] (Equation 3.1.4; S12g exchange is obtained from parametrization of empirical data). It has consistently performed well in the determination of energetics in open shell systems,[89, 90] despite its low computational cost, and was thus the ideal choice for this work.

$$E_{S12g} = E_{S12g,X} + E_{PBE,C} + E_{disp,D3} \quad (3.1.4)$$

As for the simulation of the atomic orbitals, a linear combination of Slater-Type orbitals (STOs) was used, as opposed to the more common Gaussian-Type orbitals (GTOs). While the discussion of STOs vs GTOs is outside the scope of

this work, and more often than not the choice depends on which are implemented in the software available to the computational chemist and not on a rational decision, the difference in their formulation is still noteworthy (Equations 3.1.5 and 3.1.6).

$$\psi_{STO}(r): N \cdot r^{n-1} \cdot e^{-\zeta r} \quad (3.1.5)$$

$$\psi_{GTO}(r): N \cdot r^{2n-2-l} \cdot e^{-\zeta r^2} \quad (3.1.6)$$

In both these equations, N is a normalization constant, r is the distance from the nucleus, n is a natural number corresponding to the principal quantum number, ζ is a constant related to the nucleus charge. GTOs, which include a constant to account for the orbital angular momentum (l), despite possessing exponential decay at long range like the STOs, have a much faster decay due to the quadratic term r^2. Furthermore, these do not fulfill Kato's cusp condition at $r=0$. Hence, the combination of at least three GTOs is usually required to fulfill the physical restraints that a single STO already does. This drawback is compensated by a mathematical trick that allows for the calculation of four-center integrals via finite sums of one-center integrals,[91] considerably diminishing the required calculation time.

Nevertheless, the set of STOs used here is of triple-ζ quality with two polarization functions, as the latter are key to properly emulate the shape of *d* atomic orbitals present in transition-metals.

3.2. Shortcomings of DFT

An obvious problem with DFT is the self-interaction error, as there is no way to distinguish two-body coulomb interactions from self-interaction when evaluating the electron density in equation 3.1.3.[92] This is contained within the E_{xc} term and is usually not a problem for the calculation of reaction mechanisms as error cancelation is expected when relative energies are analyzed. It is, however, extremely problematic for systems where electron transfer may occur and the electron affinity of the putative acceptor is similar to the ionization potential of the donor, such as in the case of oxoiron complexes performing C-H activation.[93] For spectroscopy simulations, this can be circumvented by finding an experimental "anchor" to which one may compare the computational results. This limitation "by design" is not the only shortcoming of Kohn-Sham DFT, and thus additional corrections may need to be employed, depending on the chemical system that one intends to study.

DFAs are known to be unable to treat London interactions properly, which are of the utmost relevance for the description of non-covalent interactions.[88] Therefore, a functional-dependent correction must be applied. The most common have been developed by Grimme and coworkers and have been improved over the years.[94-96]

Solvent also plays a key role in the stability and reactivity of chemical species. This can be modeled either by adding solvent molecules to the calculation (explicit solvation), which can easily become extremely computationally expensive, or by emulating a charged field around the chemical system in question with appropriate cavity sizes and dielectric constant (implicit

solvation[97]). The former is particularly relevant for reactions where the solvent molecule is actively participating – e.g. water acting as a proton shuttle – although, in these cases, the question of how many molecules should be included always arises (python workflows using ONIOM[98] have now been developed as a workaround to this issue[99]). In most cases, implicit solvation is sufficient to properly compute the interactions between atomic systems and two main models have been used: the polarizable continuum model (PCM)[100] and the conductor-like screening model (COSMO).[101]

Relativistic effects, present in heavy atoms, are also not taken into account by standard DFT methods and as such corrections must often be applied to compute accurate orbital shapes and consequent molecular geometries.[102, 103] One method to include relativistic corrections in DFT is the zeroth-order relativistic approximation (ZORA)[104] where potential-dependent transformations are used to get two-component Hamiltonians from the Dirac Hamiltonian. As the proper description of core electrons is not essential for the analysis of chemical bonds, relativistic effects are often included with an effective core potential.[105]

Finally, vibrational modes below 100 cm^{-1} are numerically inaccurate due to the breakdown of the harmonic oscillator model and thus the quasi-harmonic approximation by Truhlar and coworkers, where these harmonic frequencies are raised to 100 cm^{-1} in order to evaluate the vibrational component of entropy, is usually employed.[106]

3.3. TD-DFT

The Runge-Gross theorem defines the time-dependent extension of the Kohn-Sham equations.[107] It allows for the study of the dynamics of a many-body system upon interaction with a potential such as an electric or magnetic field, from the analysis of the electron density. It is used to simulate, for instance, UV-Vis spectra which requires the absorption of photons.

The idea is to produce a unique link between electron density (ρ), wave-function (ψ) and external potential (υ) over time.[108] Hence, the stationary ground-state Kohn-Sham many-electron system is now best described as:

$$\left[-\frac{1}{2}\nabla^2 + \upsilon_{ext}(\boldsymbol{r_1}) + \upsilon_{Coulomb}(\boldsymbol{r_1}) + \upsilon_{xc\sigma}(\boldsymbol{r_1})\right]\psi_{\alpha\sigma}(\boldsymbol{r_1}) = \varepsilon_{\alpha\sigma}\psi_{\alpha\sigma}(\boldsymbol{r}) \quad (3.3.1)$$

And this external potential is varying through time by means of a harmonic perturbation:

$$\delta\upsilon_{ext}(\boldsymbol{r_1}, \boldsymbol{t}) = \delta\upsilon_{ext}(\boldsymbol{r_1})\cos(\omega \boldsymbol{t})\Theta(t - t_0) \quad (3.3.2)$$

The time-dependent state of the system can finally be written as such:

$$\left[-\frac{1}{2}\nabla^2 + \upsilon_{s\sigma}(\boldsymbol{r_1}) + \delta\upsilon_{s\sigma}(\boldsymbol{r_1}, \boldsymbol{t}) - \alpha\frac{\partial}{\partial t}\right][\psi_{\alpha\sigma}(\boldsymbol{r_1})e^{-\alpha\varepsilon_{\alpha\sigma}t} + \delta\psi_{\alpha\sigma}(\boldsymbol{r_1}, \boldsymbol{t})] = 0 \quad (3.3.3)$$

Chapter 4

Spectroscopy to structure in oxo bridged iron dinuclear compounds

4. Spectroscopy to structure in oxo bridged iron dinuclear compounds

This work has been developed in collaboration with the group of Prof. Lawrence Que Jr., from the University of Minnesota.

4.1. State of the art

Dinuclear oxo-bridged iron motifs are commonly present as cofactors of enzymes that operate in important cellular functions such as cell cycle regulation, respiration and the nutrient cycle.[11, 109, 110] These metal centers catalyze reactions that may also be useful outside of the bio-sphere, including the conversion into methanol of methane,[111] one of the two main greenhouse gases. Thus, it is of great interest to obtain bioinspired synthetic analogues for these enzymes, ideally with similar catalytic activities, albeit with greater atom efficiency and a broader scope of operability conditions. Indeed, these have been sought after in recent years.[13]

The optimization of such synthetic analogues is problematic due to the notorious[13, 18] difficulty in describing the intermediates and transition states involved after dioxygen binding, as a consequence of their extremely short lifetime. Indeed, only a handful of synthetic diiron complexes were stable enough for characterization by X-ray crystallography,[112-123] and much of the knowledge obtained so far resulted from Mössbauer, UV-vis absorption and/or (resonance) Raman spectroscopy.[124, 125] In an attempt to bridge the gap between

the elusive crystal structure and the more easily obtainable vibrational spectrum, Sanders-Loehr and co-workers reported interesting correlations[126] (Figure 4.1) between the Fe-O-Fe angle and Fe-O vibrations as early as 1989, for model compounds that closely resemble enzyme cofactors (Scheme 4.1).

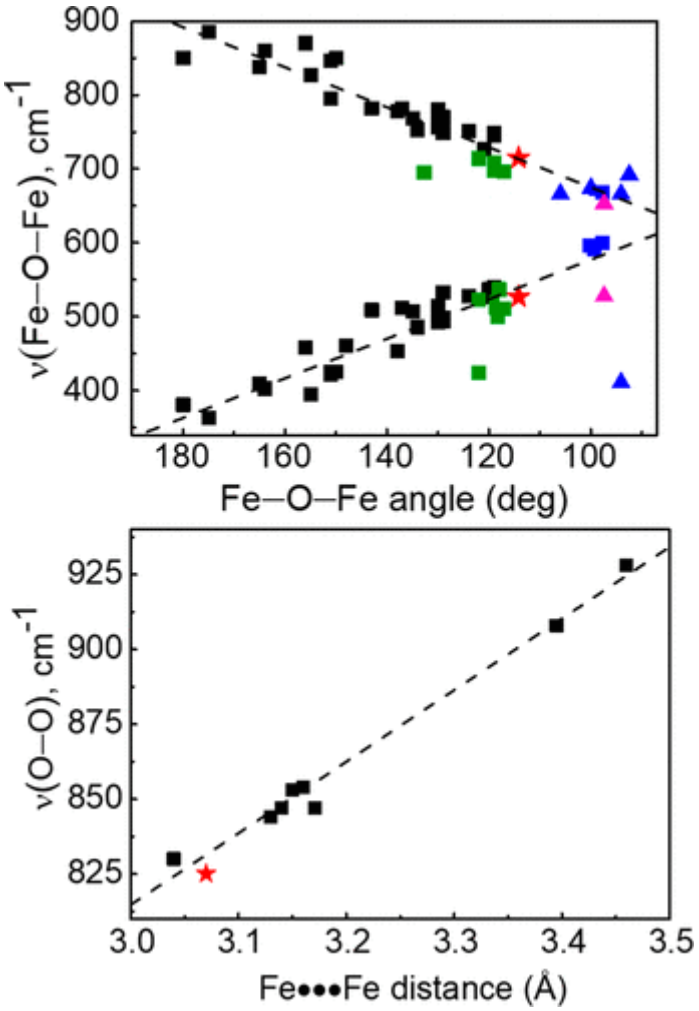

Figure 4.1. Correlation between ν_{sym}(Fe–O–Fe) (bottom) and ν_{asym}(Fe–O–Fe) (top) values of oxo-bridged diiron complexes with their Fe–O–Fe angles. The so-called Sanders-Loehr correlations can be found in black; colored points correspond to later experiments by others. Figure reproduced from original manuscript.[15]

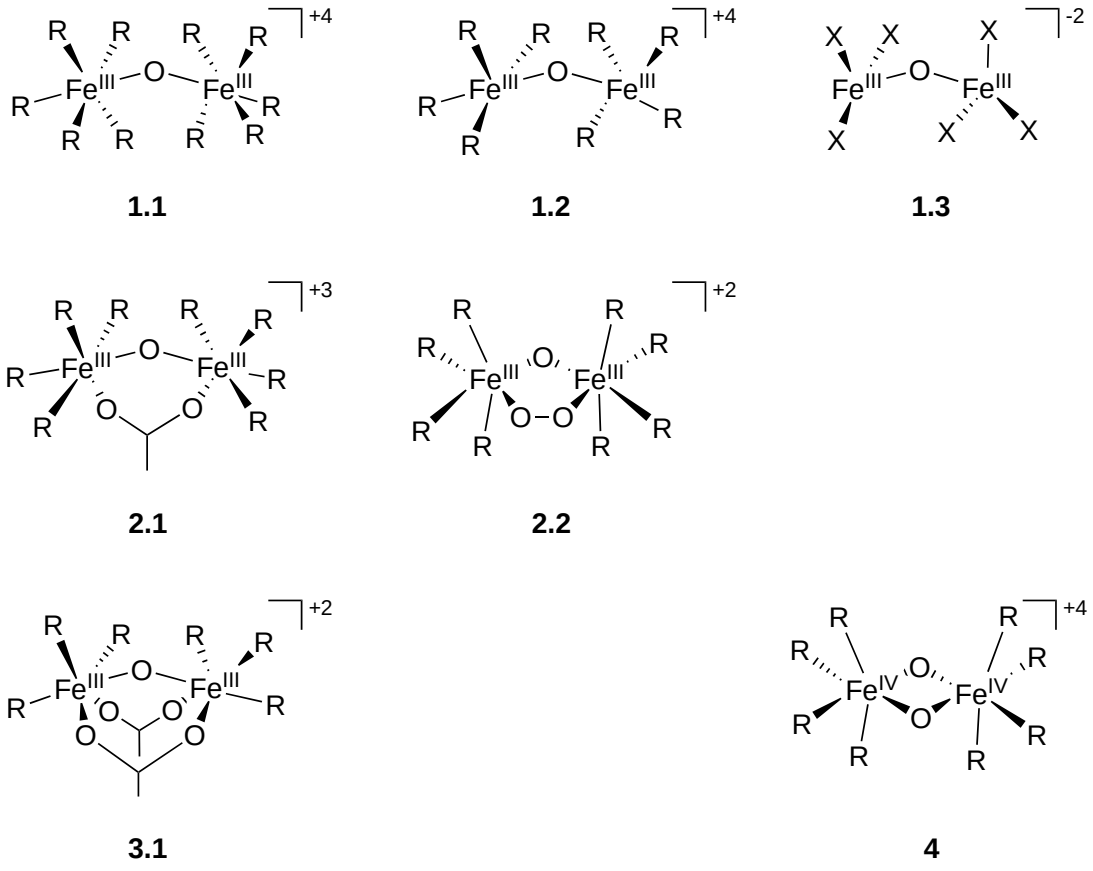

Scheme 4.1. Simplified models of the Sanders-Loehr[126] compounds (1.1-1.3, 2.1 and 3.1) and reaction (oxidation) intermediates models (2.2, 4); in the present study: R=NH3, X=Cl.

The vibrational spectra of mono-, di- and tri-bridged complexes with different ligands (see Scheme 4.1) have been analyzed and compared to protein analogues. The symmetric (ν_{sym}) vibrational mode shows a red-shift to lower frequencies as this angle increases, as observed in resonance Raman spectra when irradiating by light with a wavelength of ca. 360 nm, which is typically associated with an oxo→Fe charge transfer transition.[126] Conversely, the asymmetric (ν_{asym}) vibration, readily observed in the infrared spectrum, shows

a blue-shift to higher frequencies with increasing angle. This behavior has prompted our interest in studying the effect of the Fe-O-Fe angle[127, 128] on both vibrational modes, which have proven to be key for the understanding of the optical and structural properties of diferric compounds.[129]

Here, we put the Sanders-Loehr correlation to the test by using quantum chemistry. We try to expand the limits of the analysis by studying not only the relationship of the vibrational spectrum with the Fe-O-Fe angle, but also with the Fe-Fe distance. As such, we aim to increase the amount of geometrical information one may extract from a "simple" vibrational analysis. We also study whether information on the oxidation and spin states of the Fe atoms may be retrieved by studying the same correlation with Mössbauer parameters, i.e. the isomer shift (IS) and quadrupole splitting (QS). The computational methodology allows for the exploration of the potential energy surface (PES) beyond its minima (X-ray structures), and should provide more insight into these properties. Therefore, we explore if this could provide additional spectroscopic measurements that could be used to pinpoint structural parameters in the coordination sphere of the metal atoms, e.g. the Fe-O-Fe angle or the Fe-Fe distance.

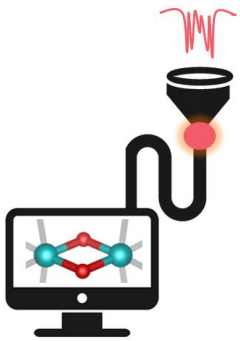

Figure 4.2. Representation of the idea behind this chapter: "feeding" a computer with vibrational spectra sheds light into the structure of the compound (and other magnetic and electronic parameters).

4.2. Computational method

DFT calculations were performed using the ADF/QUILD[130-132] program packages. Scalar relativistic corrections were employed using the Zeroth Order Regular Approximation[104] (ZORA). Solvent effects were included with the Conductor-like Screening Model[133] (COSMO) for acetonitrile in the case of the synthetic analogue models and methanol in the case subjects. Constrained geometry optimizations, frequency and single-point calculations were done with the S12g[83] functional and a triple-ζ basis set with double polarization functions[134] (S12g/TZ2P). Vibrational modes below 100 cm^{-1} were raised to this value when calculating Gibbs energies, to compensate for the breakdown of the harmonic oscillator model.[106]

4.3. Results & discussion

Our density functional theory (DFT) calculations consist of constrained geometry optimizations, which were performed within an interval of 25°/0.25 Å (with 25 steps of 1°/0.01 Å) around the equilibrium angle/distance that was

being constrained; all other coordinates were optimized freely. For the complexes in Scheme 4.1, this spans a range from 2.55 Å to 3.70 Å for the Fe-Fe distance, and from 85° to 180° for the Fe-O-Fe angle. At each of these constrained structures, we then computed the vibrational frequencies and the Mössbauer parameters to analyze the effect of these variations on the characteristic symmetrical (ν_{sym}) and asymmetrical (ν_{asym}) Fe-O vibrational modes,[15, 126] and on the isomer shift and quadrupole splitting.

The geometrical parameters for the DFT equilibrium structures of the diiron complexes are reported in Table 4.1, together with the corresponding experimental values[135-137] of the biomimetic complexes and metalloproteins: hemerythrin (HR)[138] and variants of ribonucleotide reductase (RNR).[139-141] The latter have diiron active sites in which there is an oxo bridge between the two iron centers; however, they differ in the remaining coordination environment. The Fe atoms in HR are each bound to two histidines, and one of each aspartic and glutamic acids. In RNR, the metal atoms are instead bound to two or three glutamic acids and one histidine. It should be noted that in all cases the iron centers are expected to be in the high-spin state, coupled anti-ferromagnetically.

Table 4.1. Geometry data for the PES minima, the experimentally obtained synthetic analogues (SA) and enzymes that bear Fe-O-Fe motifs (enz.): hemerythrin (HR) and ribonucleotide reductase (Ec RNR, Ct RNR). Distances in Å, angles in degrees.

	d(Fe-Fe) (Å)			∠(Fe-O-Fe) (°)			Ref.
	DFT	SA	enz.	DFT	SA	enz.	
1.1	3.52	3.57		166	174		[142]
1.2	3.47			154			
1.3	3.46	3.44		155	160		[137]
2.1	3.23	3.25		128	130		[135]
HR			3.27			129	[138]
Ec RNR			3.22			130	[139]
2.2	3.09	3.07		118	113		[15]
3.1	3.04	3.06		119	122		[136]
Ct $RNR^{IV/III}$			2.92				[140]
4	2.69	2.70		101	97		[15]
Ct $RNR^{IV/IV}$			2.76				[141]

The Fe-Fe distances obtained in our computational models are in very good agreement with experiment, as the largest difference noted is ca. 0.02-0.03 Å (<1%). The same is true for the Fe-O-Fe angles in which the largest deviation (5°) is found for model **1.3**, thus validating the DFT method chosen. An attempt was also made to compare these results to protein X-ray structures bearing Fe-O-Fe cofactors. This is a delicate analysis due to the variability in each cofactor steric arrangement, as proteins are extremely dynamic until frozen. One

hemerythrin structure[138] was found to have eight diiron centers, with Fe-Fe distances ranging from 3.21 Å to 3.32 Å and Fe-O-Fe angles varying between 122 and 133 degrees. The values presented in Table 4.1 correspond to the average and closely match those obtained for model complex **2.1**. The same is true for the structure obtained for *Ec* RNR, further validating our method. The structure of the manganese/iron centers of *Chlamydia trachomatis* RNR (*Ct* RNR, Mn^{III}/Fe^{IV}) is within reasonable agreement to model complex **2.2** (Δ=0.17 Å). The structure of *Ct* RNR in the same oxidation state (Mn^{IV}/Fe^{IV}) was also shown to closely resemble that of model complex **4**, as a mere difference of 0.07 Å was obtained between the protein and the computational model.

Even though our computational method was successful in the description of the structures of the diFe centers in the Scheme 4.1 models when compared to their SAs, the same cannot be said about the calculated vibrational frequencies. The values for the calculated ν_{sym} and ν_{asym} vibrational modes, as well as those reported for the SAs, when available, are shown in Table 4.2. While for complex 2.1 there was only a 6 cm^{-1} difference between the DFT calculated ν_{sym} and corresponding SA, discrepancies up to 86 cm^{-1} were obtained. The result is even worse for ν_{asym}, as the closest result to the SA was again for 2.1, but this time with a 44 cm^{-1} deviation and, in the case of complex 4, a difference as large as large as 230 cm^{-1} was obtained. This result is not surprising as the Scheme 4.1 models ignore the bulkiness of the ligands which can hinder the diFe core vibrations and the data is very limited, as ν_{sym} and ν_{asym} are often not identified as such, even if the Raman spectrum was recorded. This issue had already been identified in previous work by some of us,[15] where the experimentally determined vibrational modes of the SA to complex 4 were compared to the

spectrum obtained via DFT optimization of the full molecule (dftSA) and the DFT optimization of a simpler model in which the large tetradentate ligands were substituted by much smaller and flexible amine ligands (mSA). The calculated ν_{sym} and ν_{asym} for mSA were 30 cm^{-1} higher and 11 cm^{-1} lower, respectively, than those measured for the SA of complex 4.

Table 4.2. Comparison between ν_{sym} and ν_{asym} calculated for the model complexes minima (1.1-4), their respective synthetic analogues (SA) and extreme cases (the last two rows) and respective expected values from the original Sanders-Loehr correlation. Angles in degrees, frequencies in cm^{-1}. NR = not reported.

∠(Fe-O-Fe) (°)			ν_{sym} (cm^{-1})			ν_{asym} (cm^{-1})		
	DFT	SA	DFT	SA	S-L[a]	DFT	SA	S-L[a]
1.1	166		312		396	719		855
		174[b]		NR	373		NR	874
1.2	154		374		430	684		826
1.3	155		376		428	741		828
		160[c]		NR	413		NR	840
2.1	128		451		505	626		764
		130[d]		457	499		770	768
2.2	121		570		525	619		747
		113[e]		NR	548		NR	728
3.1	119		476		531	621		742
		122[f]		540	522		749	749
4	101		739		582	758		699
		97[g]		653	594		528	689

a) ref. [126]; b) ref. [142]; c) ref. [137]; d) ref. [135]; e) ref. [15]; f) ref. [136]; g) ref. [15]

Nevertheless, we have quantified the original[126] S-L correlation, which in the paper is qualitatively shown to be linear but no regression is reported, and have attempted to make ν_{sym} and ν_{asym} predictions based on the Fe-O-Fe angle of both the DFT optimized Scheme 4.1 models and their respective SAs. Although the frequencies obtained with the S-L framework are within appropriate order of magnitude for the structures of PES minima, its shortcomings are evident as there is an average deviation from the true (computed) ν of 18%, reaching a maximum of 27% for the ν_{sym} of model complex **1.1**. Except for the case of the SA corresponding to complex 3.1, the μ-oxo peroxo diFe core, where the prediction matches the measured ν_{asym} perfectly and, it also fails in the same prediction when applied to Fe-O-Fe angles determined by single crystal X-ray crystallography in real molecules. The difference is as large as 31% for the ν_{asym} of the SA of complex 4 or ca. 9% for the ν_{sym} values recorded for the SAs of complexes 2.1 and 4.

Its failure is catastrophic in extreme cases, as can be observed in Table 4.2 for the minimum values (last line), as there is a 29% difference in ν_{sym} and 37% in ν_{asym} between the S-L predicted and the DFT values.

We expect that an analysis of a larger potential energy surface area may provide better insight to the seemingly linear relationship reported by S-L, thus leading to a more accurate prediction tool. This is what we proceeded to do.

An analysis of the relationship between the computed symmetric Fe-O stretch ν_{sym} and the two key structural parameters, Fe-O-Fe angle and the Fe-Fe distance, is shown in Figure 4.3. These graphs show some interesting features that reinforce and contrast the Sanders-Loehr notions: based on experimental

data for diiron(III) systems in their equilibrium structure, an inverse relationship was observed between the symmetric stretch and the Fe-O-Fe angle. Here, however, we show that this relationship does not hold when the diiron complexes are distorted in our constrained optimizations (see Figure 2, top). Instead, for most model complexes ν_{sym} actually increases with increasing angle.

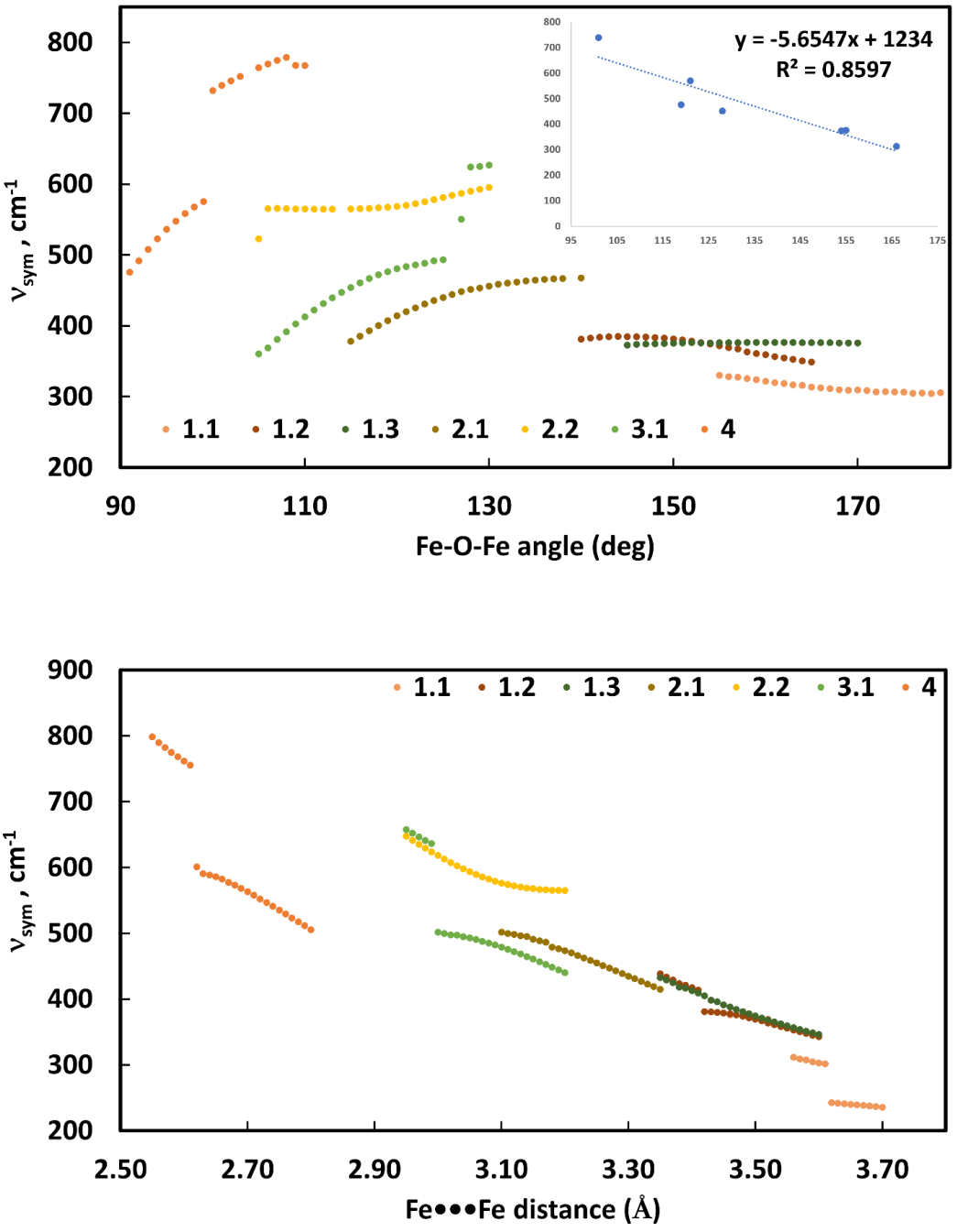

Figure 4.3. ν_{sym} vs geometrical features of the metal core. Inset of top graphic shows the results for the minimum in each PES.

This seemingly contradiction with the Sanders-Loehr results can be resolved if we do not focus on individual complexes and how their symmetric stretch responds to distortions along the Fe-O-Fe angle, but focus on the computed equilibrium structures only (Figure 4.3, top inset). Indeed, this reduced set follows a similar lowering of the symmetric stretch with increasing Fe-O-Fe angle, like the Sanders-Loehr model. Based on the linear fit to the computational data, the following linear correlation was observed:

$$\angle(FeOFe) = \frac{1234.0 - \nu_{sym}}{5.65} \quad (5.3.1)$$

Interestingly, the dependence of the symmetric stretch on the Fe-Fe distance shows the same relationship computationally and from the Sanders-Loehr. I.e., when varying Fe-Fe distances, ν_{sym} exhibited a linear decrease with increasing distance. This is true not only for minima, but also for the whole PES explored. Equation 5.3.2 contains the linear regression of the complete distance range and should provide more accurate results than a simple equilibrium structure analysis:

$$\mathrm{d}(FeFe) = \frac{1617.7 - \nu_{sym}}{357} \quad (5.3.2)$$

The same scrutiny was conducted for ν_{asym}. Results can be found in Figure 4.4.

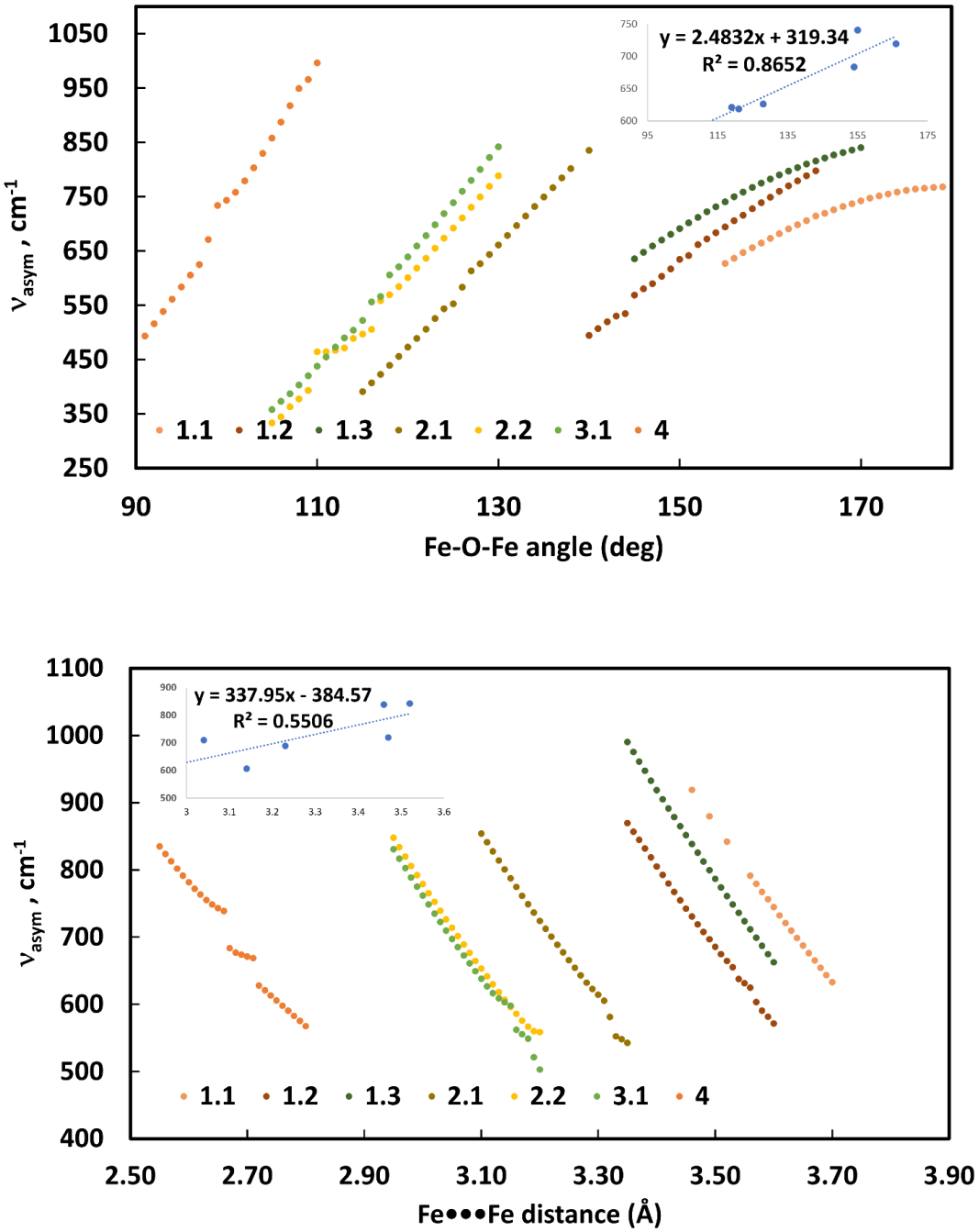

Figure 4.4. ν_{asym} vs geometrical features of the metal core. Inset of top graphic shows the results for the mínima.

In the case of ν_{asym}, the trends are much more discernible: there is a mostly linear increase with Fe-O-Fe angle and a linear decrease with d(FeFe). Although one could consider the linear regression for each complex, it would be difficult to determine any geometrical parameter from the associated frequency. If one ignores the outlier from compound 4 and performs the analysis of the minima (Figure 4.4, insets), the following equations can be derived:

$$\angle(FeOFe) = \frac{\nu_{asym} - 319.3}{2.48} \quad (5.3.3)$$

$$\mathrm{d}(FeFe) = \frac{\upsilon_{asym} + 384.6}{338} \quad (5.3.4)$$

Equation 5.3.4 was obtained with a considerably lower coefficient of determination and thus should be used carefully. The opposite exercise – to obtain unknown asymmetrical frequencies from known geometrical parameters – should prove itself more straightforward. Here, one must analyze which regression to adopt for the appropriate angle/distance range.

Table 4.2 can now be revisited after the reparameterization of the linear correlations. Table 4.3 shows how well the S-L framework compares to the calculated (Scheme 4.1 models) or experimentally recorded (SAs) vibrational frequencies. The reparameterization from this work is included in the table for comparison, including the correlations derived from d(FeFe) which are completely new. In the last row, one can read the average of the deviation of each methodology in modulus.

Table 4.3. Comparison between $\Delta\nu_{sym}$ and $\Delta\nu_{asym}$ (Δ = predicted vibrational frequency – recorded/calculated vibrational frequency) using the S-L framework and the correlations in this work for the model complexes minima (1.1-4), and their respective synthetic analogues (SA) when reported. Frequencies in cm^{-1}.

	∠(Fe-O-Fe)				d(FeFe)	
	$\Delta\nu_{sym}$ (cm^{-1})		$\Delta\nu_{asym}$ (cm^{-1})		$\Delta\nu_{sym}$ (cm^{-1})	$\Delta\nu_{asym}$ (cm^{-1})
	S-L[a]	This work	S-L[a]	This work	This work	This work
1.1	84	-16	136	12	49	86
1.2	56	-10	142	17	5	104
1.3	52	-18	87	-37	7	44
2.1	54	60	138	11	14	81
SA[d]	42	43	-2	-128	1	-56
2.2	-45	-3	128	-7	-55	41
3.1	55	86	121	-7	56	22
SA[f]	-18	5	0	-126	-15	-99
4	-157	-76	-59	-188	-82	-233
SA[g]	-59	33	161	32	1	0
Avg.	62	35	97	57	29	77

a) ref. [126]; d) ref. [135]; f) ref. [136]; g) ref. [15]

There is a ca. 40% decrease in average prediction error when we move from the S-L framework to the correlations developed in the present work. $\Delta\nu_{sym}$ can be even more accurately predicted if the d(FeFe) correlation is used. The same is not true for $\Delta\nu_{asym}$, as even though it improves on S-L, the best predictions are still obtained through the correlation of this vibrational mode and the Fe-O-Fe angle.

The same investigation was performed for the expected Mössbauer isomer shift and quadrupole splitting values. This analysis can be found in Figure 4.5 and Figure 4.6, respectively.

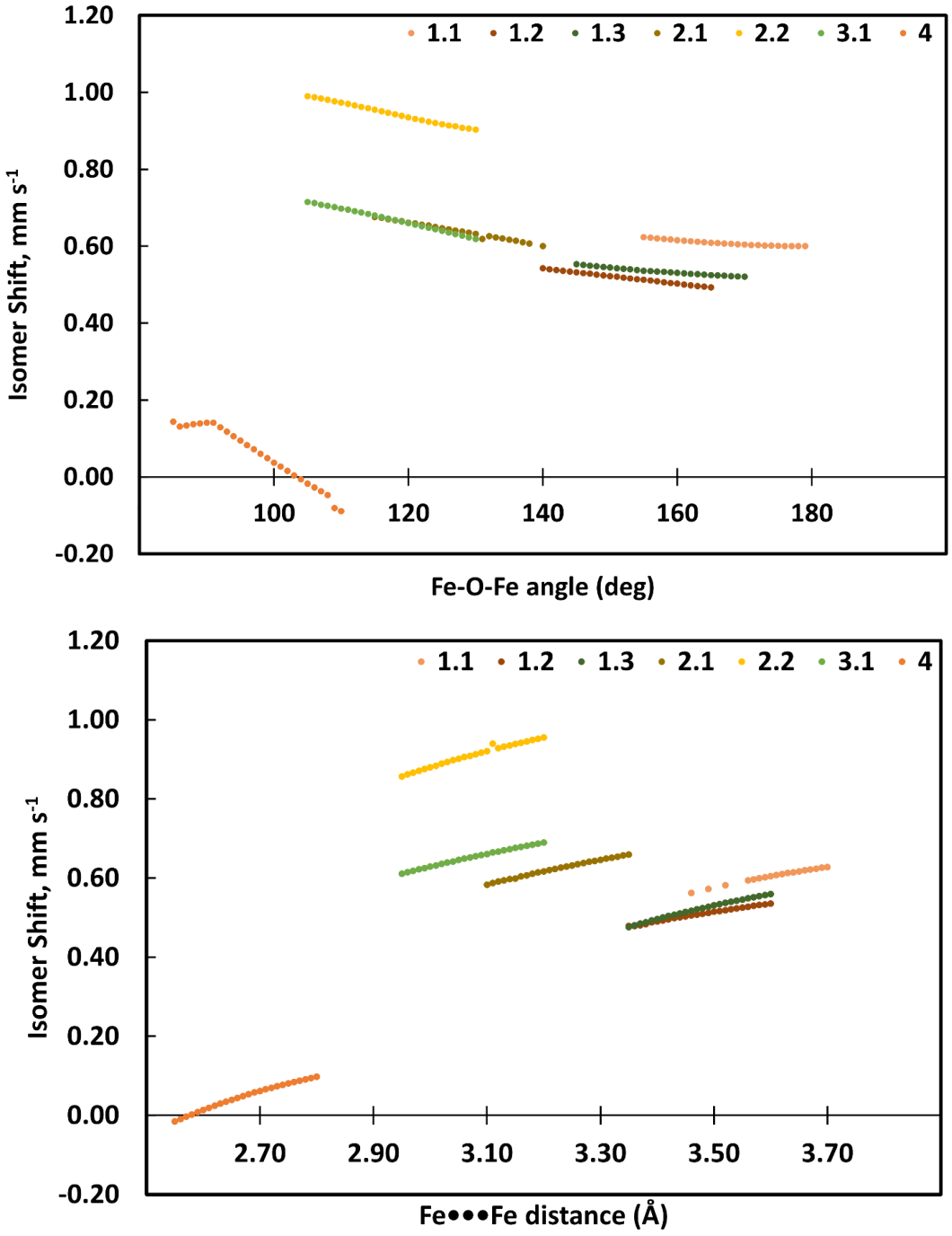

Figure 4.5. Isomer shift vs geometrical features of the metal core.

Two outliers are immediately noted: **2.2** and **4**. For **4**, this is expected since Fe(IV) species have lower isomer shifts than Fe(III) – the oxidation state of all the other complexes. The isomer shifts obtained for the diiron peroxo complex **2.2**, which are greater than the remaining Fe(III) species, had previously been reported and interpreted by others.[15] A general decrease in IS is observed with increasing angle and the opposite occurs for the Fe-Fe distance. The analysis of the minima reveals a linear decrease of IS with both increasing Fe-O-Fe angle and Fe-Fe distance. By removing the outliers, compounds **4** (diamond core, Q) and **2.2** (oxo-peroxo bridges, P) from the data set and analyzing just the minima, Equations 5.3.5 and 5.3.6 are obtained.

$$IS = \left(-0.0023 \times \angle(FeOFe)\right) + 0.9181 \quad (5.3.5)$$

$$IS = \left(-0.2424 \times \mathrm{d}(FeFe)\right) + 1.3855 \quad (5.3.6)$$

The same general relationship between the geometrical parameters and the QS is observed: a decrease with increasing angle and increase with increasing Fe-Fe distance. As in the case of the isomer shift, the analysis of the minima for both angle and distance variation again shows a linear decrease in QS. The equations obtained for the full minima dataset are represented below (Equations 5.3.7 and 5.3.8).

$$QS = \left(-0.0453 \times \angle(FeOFe)\right) + 5.5145 \quad (5.3.7)$$

$$QS = \left(-4.0111 \times \mathrm{d}(FeFe)\right) + 12.2090 \quad (5.3.8)$$

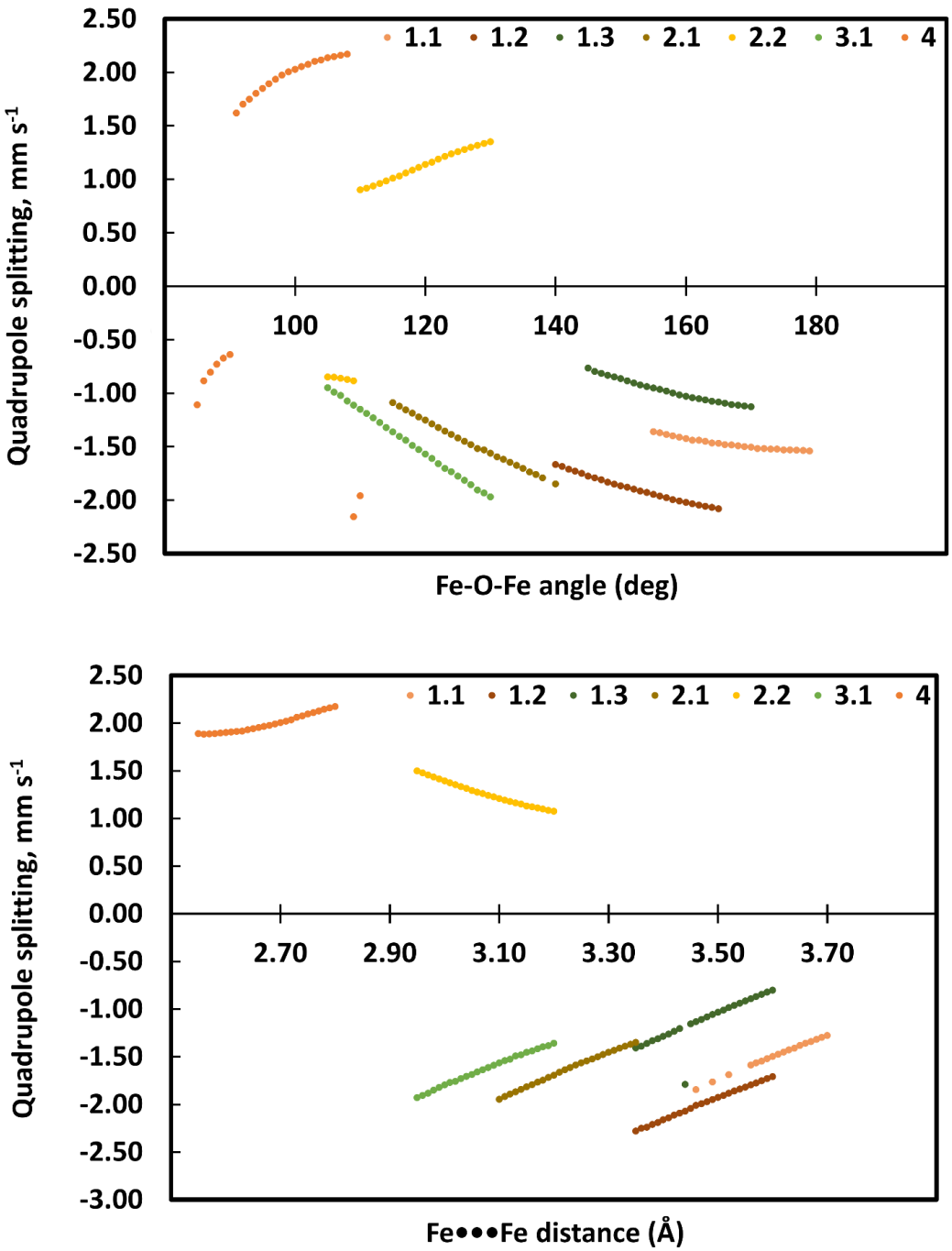

Figure 4.6. Quadrupole splitting vs geometrical features of the metal core.

Upon choosing the regressions with the best coefficient of determination, which were obtained for IS as opposed to QS, and applying a simple mathematical transformation to facilitate the potential use of this data, one can write the more general Equations 5.3.9 and 5.3.10:

$$d(FeFe) = \frac{1.3855 - IS}{0.2424} \quad (5.3.9)$$

$$\angle(FeOFe) = \frac{0.9181 - IS}{0.0023} \quad (5.3.10)$$

It is now time to put these equations to the test! As the complexes reported by Strautmann[143] were reported not to follow the Sanders-Loehr correlation, it is interesting to test them in the scope of this work and to compare such results against those obtained with the S-L model. Another μ-oxo-diiron(III) complex previously studied by some of us with an analogous computational method was also analysed.[144] Although both complexes contain tris(2-pyridylmethyl)amine (TPA) derivatives as ligands, their coordination spheres are different, as, excluding the oxo bridge, the Fe atoms in the Strautmann complex are bound to tetradentate N_2O_2 units of the same ligand, and the irons in the latter complex are instead bound to a pentadentate phenolato N_4O ligand (see Scheme 4.2). We have developed a GUI-calculator to facilitate the use of the correlations presented here (Figure 4.7).[145]

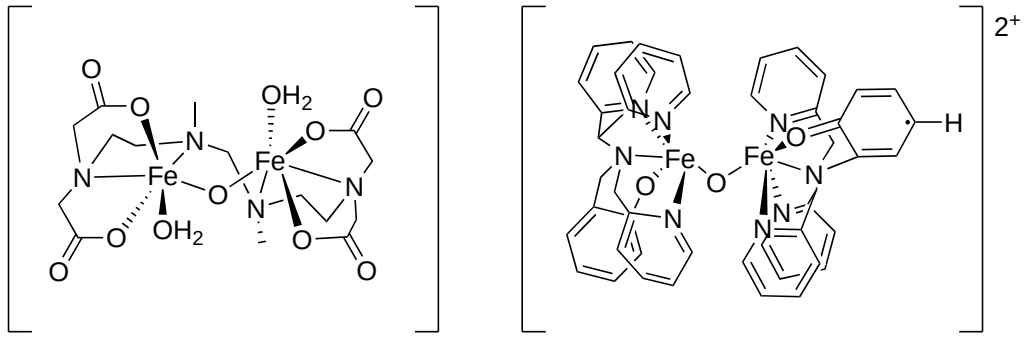

Scheme 4.2. Structures of the complexes selected for the benchmarking of the methods developed here.

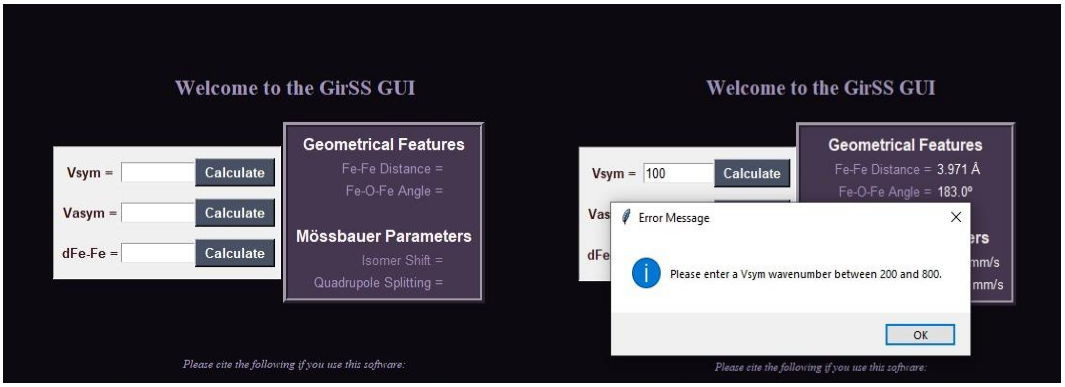

Figure 4.7. GirSS interface (left) and warning pop-up if used incorrectly (right).

The oxo-bridged diiron(III) complex built with the bis-tetradentate N_2O_2 ligand H_4julia, $[Fe^{III}(OH_2)(\mu\text{-}O)Fe^{III}(OH_2)(julia)]$, by Strautmann and co-workers was chosen for method validation among the seven complexes reported due to the small R-factor of its crystal structure (0.0456) and smaller size (Scheme 4.2, left). The lowest energy state is the one in which the irons are in the high-spin state, antiferromagnetically coupled, in line with results for the biological

analogues. The comparison of structural parameters between the experimental and computational models is found in Table 4.4.

Table 4.4. Comparison between the X-ray crystal and DFT (S12g/TZ2P) structures of the Strautmann complex.

	Experiment	**Computational Model**
∠(Fe-O-Fe) / deg	165	151
d(Fe-Fe) / Å	3.52	3.43
ν_{asym} / cm^{-1}	882 / 889	789
IS / mm s^{-1}	0.47	0.49 / 0.43
QS / mm s^{-1}	1.91 / 2.04	2.09 / 2.21

Good agreement was obtained. The Fe-O-Fe angle was found to be only 14 degrees lower than that obtained experimentally and the difference in Fe-Fe distance was of only 0.09 Å, 2.6%. Reasonable agreement is observed in the vibrational frequencies and Mössbauer parameters.

The ν_{asym} reported experimentally was 882 or 889 cm^{-1}, depending on the number of water molecules it contained, seven or six, respectively. With DFT, we identify the 789 cm^{-1} vibrational mode as the one corresponding to ν_{asym}. From Equations 3 and 4, one can expect an Fe-Fe distance of 3.47 Å and an Fe-O-Fe angle of 189 degrees. Although these results are worse than those obtained within the S-L framework (178°), the information obtained for the angle, if read as approximately 180 degrees, is still within reason. Additionally, we provide information on the Fe-Fe distance, which was offset by only 0.04 Å. ν_{sym} is not reported as often as ν_{asym}, and the same is true for this case. The correlations

obtained in this work are much better with the former, which hinders the correct description of these molecules. It is now also possible to try to retrieve information on the oxidation/spin state of the complexes, by means of equations 5.3.5 and 5.3.7 and the experimental values for the Fe-O-Fe angle or equations 5.3.6 and 5.3.8 if the Fe-Fe distance of the crystal structure is studied. There is perfect agreement between both regressions as the value estimated for the IS from both Equations 5.3.5 and 5.3.7 is 0.53 mm s^{-1} and they are also very close to the experimental value reported (0.47 mm s^{-1}). The same agreement is observed for the values of QS obtained from Equations 5.3.7 and 5.3.8 (-1.96/-1.91), and they match well with the experimental values (1.91/2.04).

In this case, the experimental values for the Mössbauer parameters are available, and thus the opposite exercise, in which one estimates geometrical features from the magnetic data, can also be performed. To do so, we apply equations 5.3.9 and 5.3.10 to the observed experimental IS of 0.47 mm s^{-1}. The results provide an estimate of 3.78 Å for d(FeFe) and 195 degrees for the Fe-O-Fe angle. Although this represents an error of ca. 7% for the Fe-Fe distance and ca. 18% for the Fe-O-Fe angle, one should keep in mind that these estimates can be obtained in seconds and no computational expenditure is required.

Our second real-life example is the $[(L)Fe^{III}(\mu\text{-}O)Fe^{III}(L)]^{2+}$ complex,[144] with L = 2-(((di(pyridin-2-yl)methyl)(pyridin-2-ylmethyl)amino)methyl)phenol, which acts as a model system for the active site of galactose oxidase because of its redox non-innocent ligand (Scheme 4.2, right). This polypyridyl complex has been studied by Ligtenbarg and co-workers, who reported a crystal structure that revealed an Fe-Fe distance of 3.47 Å and an Fe-O-Fe angle of 151°.[146] The model presented here predicts an IS of 0.56 mm s^{-1} and QS of -1.33/-1.71 mm s^{-1}.

This is indicative of iron(III) centers, in agreement with that observed experimentally. The prediction of the relevant vibrational frequencies from the mentioned geometrical parameters can be found in Table 4.5.

Table 4.5. Comparison of experimental and DFT values for ν_{sym} and ν_{asym} with those obtained with the Sanders-Loehr relationships (eqs. 5.3.1-4) based on DFT structural parameters. Frequencies in cm^{-1}.

	Exp.	DFT	d(FeFe) model	∠(FeOFe) model
ν_{sym}	411	397	392	340
ν_{asym}	787	789	794	712

The d(FeFe) model, when applied to the DFT-obtained Fe-Fe distance, was able to predict, with good accuracy, both ν_{sym} and ν_{asym}, deviating in both cases by only 5 cm^{-1}. As the DFT calculated frequencies are in this case in close agreement with those obtained experimentally, the model is equally applicable to real complexes (largest difference of 19 cm^{-1}). The same is not true for the ∠(FeOFe) model. With a deviation of 57 cm^{-1} in the case of ν_{sym} and 77 cm^{-1} in ν_{asym}, its performance is much poorer, in the analysis of this compound. Indeed, the coefficient of determination of the regression obtained for ν_{asym} in this latter model was considerably lower (0.55 vs 0.87). For this complex, no magnetic parameters were reported. However, we can put our computational model to the test and apply Equations 5.3.9 and 5.3.10 to the theoretical IS value of 0.56 mm s^{-1} to provide an estimate for the geometrical features of the oxo bridge. We obtain 3.41 Å for d(FeFe) and 156 degrees for the Fe-O-Fe angle. The correlation, thus, is much more accurate in this case, as the error in the Fe-Fe

distance was only of 0.06 Å (smaller than 2%) and of 5 degrees (ca. 3%) in the Fe-O-Fe angle.

Ultimately, using constrained optimizations, we have studied how the vibrations and spectroscopic data depend on the structural parameters, and determined linear correlation parameters for them. We have validated the use of these parameters for two real-life examples of diiron(III) complexes for which a crystal structure and vibrational data are available. Very good results were obtained for the Mössbauer parameters and the Fe-O vibrations, which have been predicted based on the Sanders-Loehr correlations to within 0.05 $mm \cdot s^{-1}$ (isomer shift, quadrupole splitting) and 5 cm^{-1} (ν_{asym}/ν_{sym}). Vice-versa, based on the experimental/computed vibrations and Mössbauer parameters, the structural parameters can be predicted to within ca. 0.05 Å (Fe-Fe distance) and ca. 5° (Fe-O-Fe angle).

Chapter 5

Electronic properties of N-confused metalloporphyrins

5. Electronic properties of N-confused Metalloporphyrins

5.1. State of the art

Porphyrin-like motives found in biological molecules such as the heme group[147], vitamin B12[148] or chlorophylls[149] inspired chemists to synthesize tetraphenylporphyrin (TPP), octaethyl porphyrin (OEP), many derivatives, transition-metal complexes and materials with all kinds of interesting properties.[150] Eventually, studies turned to its isomers and new porphyrinoids have arisen.[151] The first N-confused porphyrin (NCP) (see Scheme 5.1) was synthesized in 1994.[152, 153] Two of its tautomers were later successfully isolated depending on the solvent: NCP-3H and NCP-2H,[154] which, in conjunction with DFT[79] calculations, allowed for the study of their individual properties,[155-157] unraveling their promise for application such as the development of new photodynamic therapeutics.[158] NCP-3H exhibited a higher degree of aromaticity and was thus considered to be more stable. Nevertheless, transition-metal complexes with both tautomers have been synthesized[159-162] and they are often interconvertible via redox reaction. The possibility of forming neutral molecules when combined with M^{II} and M^{IV} (with axial ligands) metal ions with decreased steric hindrance in its center, or of the derivatization of the outer N-H bond, however, confer additional interest to the NCP-2H form.

The complexes of such ligands have become a hot topic due to their prospective anti-cancer activity,[163] CO_2 fixation/derivatization capabilities[164-166] and ability to function as molecule (anion) sensors[167] or photosensitizers.[168] The properties of these compounds have been tentatively rationalized with analyses of the relative energy differences of their frontier orbitals (ΔHOMO and ΔLUMO)[169]

which are mainly located in the porphyrin ring and barely mixed with the metal *d* orbitals. They have been obtained, however, in the bare porphyrin forms, with axial ligands[170] and even as metal-metal bonded dimers[171] and there is no explanation for this preference or its consequences on the properties of these compounds. The repercussions of changing the metal center have also not been explored, especially with regards to spin state which is often not reported.

Here, we study a series of (theoretically) Cr(II), Cr(III), Mo(II), Mo(IV), Os(II), Os(IV), and Rh(III) complexes with the N-confused porphyrin isomer NCP-2H to understand the different forms in which they are obtained, their spin state and electronic structure.

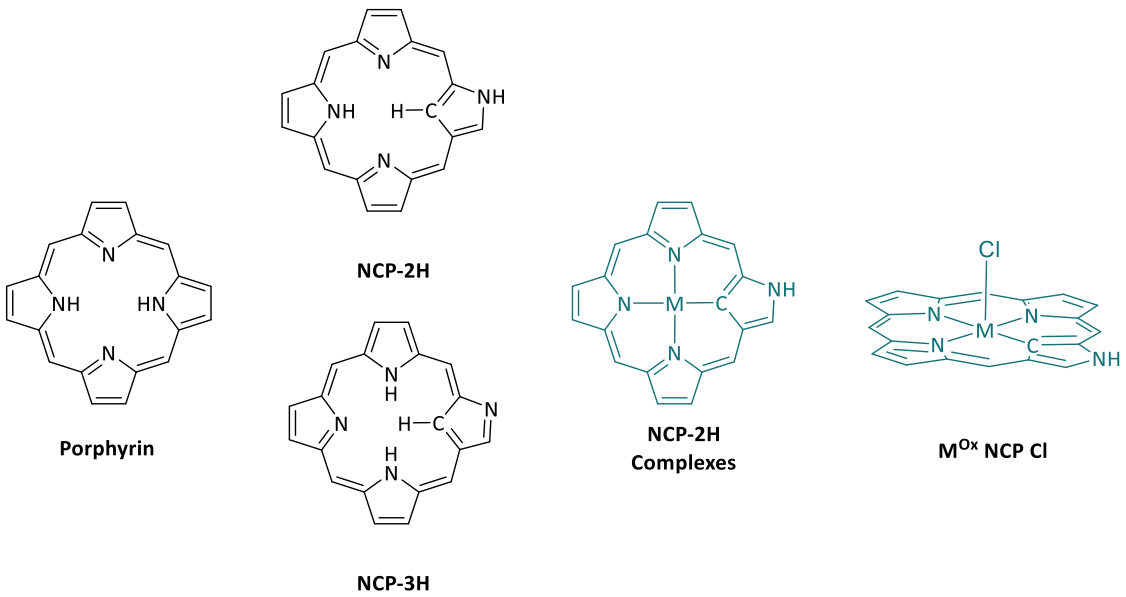

Scheme 5.1. Schematic structure of a porphyrin, its N-confused isomers including the one used as a ligand here, and corresponding transition-metal complexes. The latter two are analyzed in the present work: M = $Cr^{II/III}$, $Mo^{II/IV}$, $Os^{II/IV}$, Rh^{III}.

5.2. Computational method

DFT calculations were performed using the ADF/QUILD[130-132] program packages. Scalar relativistic corrections were employed using the Zeroth Order Regular Approximation[104] (ZORA). Solvent effects were included with the Conductor-like Screening Model (COSMO)[133] for dimethylformamide. Geometry optimizations, frequency, TDDFT and single-point calculations were done with the S12g[83] functional and a triple-ζ basis set with double polarization functions[134] (S12g/TZ2P). Vibrational modes below 100 cm^{-1} were raised to this value when calculating Gibbs energies, to compensate for the breakdown of the harmonic oscillator model.[106]

5.3. Results & Discussion

To the best of our knowledge, no X-ray structures are available in the CCDC database for N-confused porphyrins. Luckily, previous results had indicated that the methodology developed in-house for determining bond-orders[172] based on the S12g functional[83] was successful in the description of the properties of porphyrin transition metal complexes. However, because of the diversity of coordination environments of the metal in (confused) porphyrins with different axial ligands, we started by testing our computational method against experimental data available in the literature for porphyrin-chloride systems.

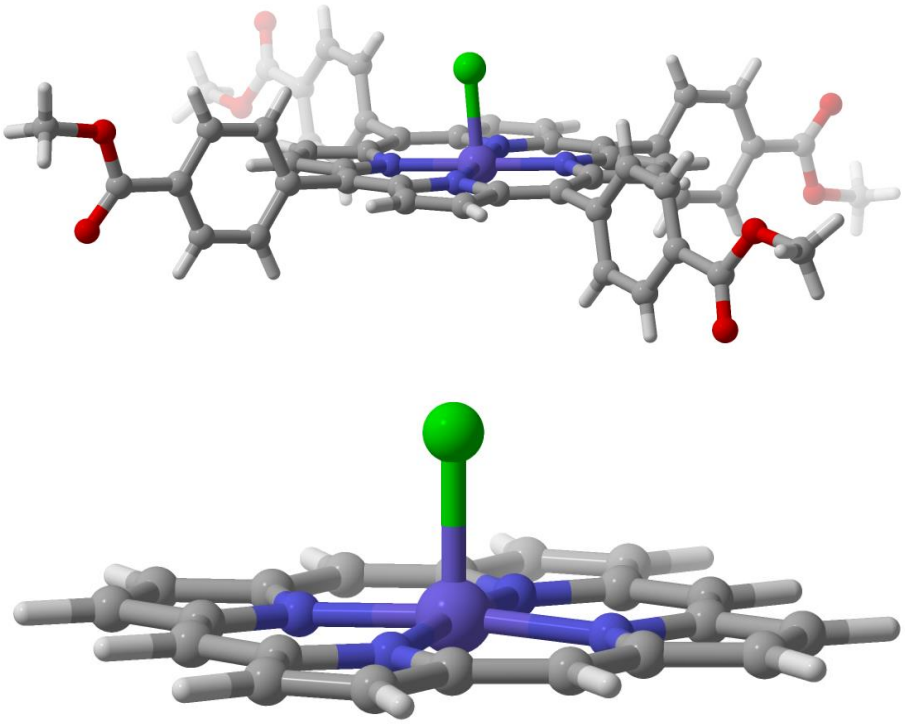

Figure 5.1. Example of the X-ray crystal structure of the Rh(Por)Cl complex reported in the literature (top, CCDC code JETBUI[173]), and our computational model (bottom).

Metal-Cl porphyrin structures were retrieved from the Cambridge Crystallographic Data Center database with Cr, Rh and Os, reorganized and simplified to a model which was devoid of substituents on the porphyrin ring (Figure 5.1). The models were then optimized with S12g/TZ2P (including solvent and relativistic effects, see Computational details) in all the relevant spin states and their energy minima were analyzed. Comparison of these results to those available in the original literature reports can be found in Table 5.1.

Table 5.1. Comparison between M-Cl distance and ground spin state of the complexes reported in the literature and our computational models.

	M-Cl (Å)		Ground state (S)		CCDC	ref
	Exp.	DFT	Exp.	DFT		
$Cr^{III}(Cl)(H_2O)$	2.321	2.296	3/2	3/2	ROTKES	[174]
$Os^{IV}(Cl)_2$	2.293	2.324	1[a)]	1	ZAVLIR	[175]
$Rh^{III}Cl$	2.204	2.261	0	0	JETBUI	[173]

a) Actual magnetic moment measured was slightly lower than expected for S=1.

The coordination environment in our computational models is the same as that found in the crystal structure: a Cl axial ligand was added in the case of Rh, two in the case of Os and one Cl and one water molecule in the case of Cr. Indeed, our models proved to be good representations of the full complexes that had been synthesized, thus showing the minor effect of the porphyrin substituents on the structural and electronic properties of the metal center. The correct ground (spin) state was predicted for all three complexes using the chosen method, S12g/TZ2P. The largest M-Cl bond distance differences between theory and experiment were obtained for the Os^{IV} complex (0.031 Å, 1.4%) and the Rh^{III} (0.057 Å, 2.6%) meaning that the DFT geometries are also in good agreement with the single crystal X-ray results.

We have confirmed the reliability of the S12g functional for the systems at hand and are now able to delve deeper into the electronic properties of these N-confused metalloporphyrins. A correct spin ground state is crucial for the shape and electronic transitions of these molecules; hence it must be analyzed first. This was performed not only for the bare metallo-N-confused porphyrin, but also for the analogues with a negatively charged axial ligand from each end of the spectrochemical series (Cl^- and CN^-). We chose monoanions to keep the total charge of the final complexes at the bare minimum. The results are

presented consecutively, with increasing number of *d* electrons, from d^2 in the Mo(IV) NCPs to d^6 in the case of those bearing Os(II) or Rh(III) metal ions.

The two cations with the lowest *d*-electron count are $Mo^{IV}(4d^2)$ and $Cr^{III}(3d^3)$. Energies of the possible spin states, relative to the lowest lying state, for their NCP complexes are represented in Scheme 5.2.

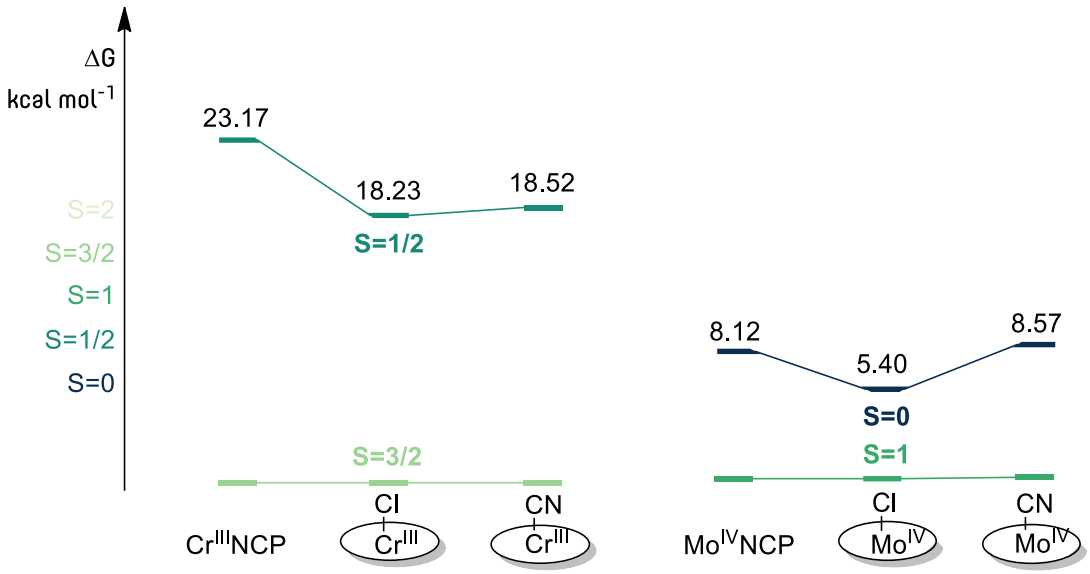

Scheme 5.2. Spin state relative energies for Cr^{III} and Mo^{IV} N-confused porphyrins and their pentacoordinate analogues.

In both cases, a high-spin (S=3/2 and S=1, for chromium and molybdenum, respectively) electronic distribution is shown to be more stable for the bare N-confused porphyrins. The same effect is observed upon addition of the axial ligands for the d^2 and d^3 populations: the low-spin state is slightly stabilized by the low-field inducing chloride anion, but this stabilization is counteracted by the high-field axial ligand cyanide. Nevertheless, no spin state change is to be expected when moving from the square planar to square pyramidal coordination sphere.

Three metal ions studied here have a d^4 population: Cr^{II} ($3d^4$), Mo^{II} ($4d^4$) and Ov^{IV} ($5d^4$). This series provides insight into the effect of core potential as each metal belongs to a different period of the periodic table. Results are in Scheme 5.3.

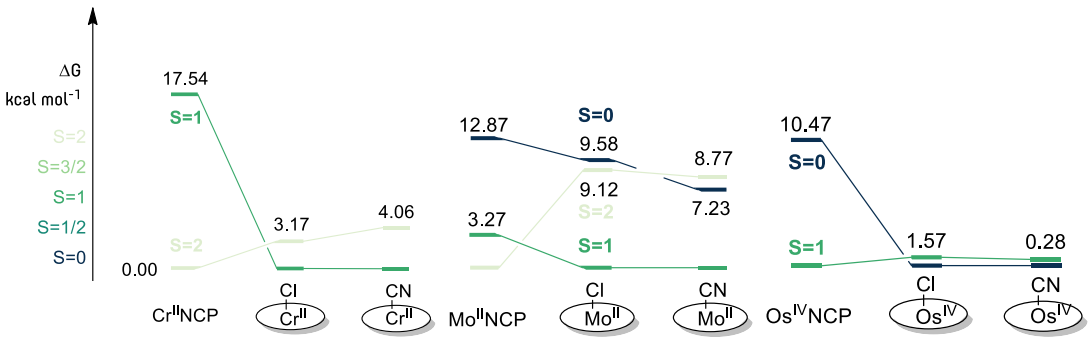

Scheme 5.3. Spin state relative energies for Md⁴ N-confused porphyrins and their pentacoordinate analogues.

The core potential is not affecting the spin state, as similar energy profiles were obtained for the three metal centers. A high-spin state is the most favorable for the bare metal NCPs (S=2 for Cr^{II} and Mo^{II}, S=1 for Os^{IV}), but the coordination of an axial ligand, even with a low field strength, stabilizes a lower spin configuration to such extent that a spin change is to be expected. In the case of osmium, energy differences close to the chemical accuracy limit (1.57 kcal mol^{-1} and 0.28 kcal mol^{-1}) are obtained, so it is possible that a mixed spin distribution is measured experimentally, depending on the temperature. However, the increase in Δ_{SP} to a point that it matches or is greater than the spin pairing energy and the qualitative similarity to the other two energy profiles are clear.

The metal ions with the highest *d* electron population are $Rh^{III}(4d^6)$ and $Os^{II}(5d^6)$. The results obtained for those metalloporphyrin complexes are in Scheme 5.4. Energies above 33 kcal mol^{-1} are not represented to scale.

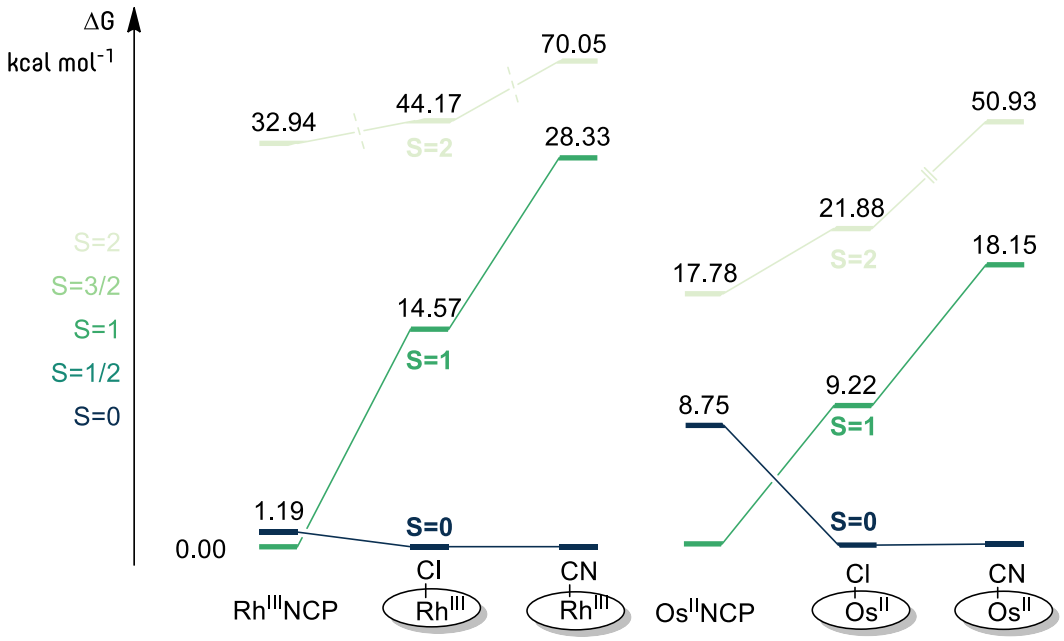

Scheme 5.4. Spin state relative energies for Md^6 N-confused porphyrins and their pentacoordinate analogues.

We have again obtained comparable energy profiles for the two metals. The S=2 high-spin configuration is too high in energy for the bare NCP complexes and those with an axial ligand, regardless of the metal center. The intermediate spin state is the most stable for the square planar complexes, but the low-spin (S=0) configuration is clearly the most stable for the complexes with axial ligands.

A summary of the results presented above can be found in Table 5.2.

Table 5.2. Summary of the results presented above on the spin state of the complexes.

	Ground state (S)			
	d^2	d^3	d^4	d^6
M(NCP)	1	$^3/_2$	2 / 1	1
M(NCP)Cl	1	$^3/_2$	1 / 0	0
M(NCP)CN	1	$^3/_2$	1 / 0	0

The same spin states and energy profiles were obtained for the complexes with equal *d* electron count; they seem to depend only on the number of *d* electrons and not on the charge of the metal or even the total charge of the complexes. The exception to this rule was Os^{IV} which, despite having a similar energy profile to the remaining d^4 complexes, can stabilize lower spin states even further. The coordination to an additional axial ligand can either have no effect on the spin state, for smaller *d* orbital populations, or allow for the stabilization of a lower spin configuration via increase of the energy difference between the stabilized and the destabilized *d* orbitals. This, however, is occurring simply due to the destabilization of the d_{z2} orbital upon axial ligand coordination: the strong field ligand cyanide would generally only extend the effect of the low field chloride, further destabilizing already higher energy electronic configurations.

As shown before, the present computational method proved to be accurate in assigning the spin state of metallo porphyrinate complexes. Porphyrin derivatives, however, are known non-innocent ligands[176] so a careful look into the electronic structure of these complexes must be carried out to understand if all of the spin density in these complexes is located in the metal centers or if the NCP ring is the entity that will participate in redox processes involving

these complexes. This may occur even if the aromatic system is disrupted by the N-confusion. The combination of a population analysis of molecular orbitals with great *d*-character with the mapping of the Mulliken spin densities should provide this information.

For both d^6 metallo-N-confused porphyrins, a S=1 ground spin state was obtained. This would correspond to a low-spin state in the square-planar ligand field, with two filled *d*-based molecular orbitals (4 electrons) and two SOMOs. A Sit analysis[177] of the *d*-orbital occupations reveals a total of four electrons. This means that instead of the expected Rh(III) and Os(II) cations, we formally observe the coupling of Rh(IV) and Os(IV) with ligand radicals, $Rh^{IV}NCP^{\bullet}$ and $Os^{IV}NCP^{\bullet\bullet}$. From a ligand-field point of view, this can be rationalized as the low-lying *d*-orbitals will all be partially occupied, thus increasing the stability of the complexes. The spin-density, however, is in different parts of the NCP ring (Scheme 5.5). In the case of the Rh NCP, there is one highly localized unpaired electron on the confused carbon atom and the remaining electron is delocalized over the four N-confused porphyrin C_β. In the case of the Os NCP, the two electrons are completely delocalized over the outer ring of the ligand.

The Os(IV) NCP complex is correctly described as bearing formal Os(IV). This agrees with the above observation: Osmium will always prefer to have four unpaired *d* electrons and redox processes are expected to occur on the ligand. A similar observation is made for the molybdenum metal ions: the Mo(II) complex is best described as formal Mo(IV) coupled with a Mo(II) diradical as similar spin densities are obtained for the metal center and only two SOMOs were obtained. Finally, the same was observed for the theoretical Cr(II) NCP,

which instead is better described as $Cr^{III}NCP^{\bullet}$ indicating that reduction of the Cr(III) compound would reduce the ligand and not the metal.

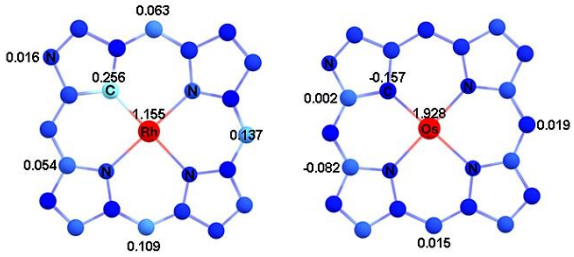

Scheme 5.5. Mulliken spin density atom coloring from dark blue (~0.0) to red (> 1.0) for the lowest spin states of Rh(NCP) and OsII(NCP) – the latter is representative of the remaining M(NCP) complexes. Numbers represent the Multipole Derived Charge Analysis (q) spin densities for relevant atoms.

These preliminary results have directed us to properly investigate the electronic structure of all these compounds. We have done so via a combined oxidation state and spin density analysis (see Table 5.3 and Table 5.4).

Table 5.3. Number of unpaired electrons (Tot.), spin density of the metal (M), sum of the ligands spin density (P) and respective percentages.

	MP					**MPCl**					**MPCN**				
	Tot.	M	P	%M	%P	Tot.	M	P	%M	%P	Tot.	M	P	%M	%P
Cr^{II}	4	3.28	0.72	0.82	0.18	2	2.47	-0.47	1.24	-0.24	2	2.54	-0.54	1.27	-0.27
Cr^{III}	3	3.72	-0.72	1.24	-0.24	3	2.45	0.55	0.82	0.18	3	2.74	0.26	0.91	0.09
Mo^{II}	4	4.35	-0.35	1.09	-0.09	2	1.32	0.68	0.66	0.34	2	1.44	0.56	0.72	0.28
Mo^{IV}	2	2.13	-0.13	1.07	-0.07	2	1.36	0.64	0.68	0.32	2	1.49	0.51	0.75	0.25
Os^{II}	2	1.93	0.07	0.96	0.04	0	0.00	0.00	0.00	0.00	0	0.00	0.00	0.00	0.00
Os^{IV}	2	2.43	-0.43	1.21	-0.21	0	0.00	0.00	0.00	0.00	0	0.00	0.00	0.00	0.00
Rh^{III}	2	1.15	0.85	0.58	0.42	0	0.00	0.00	0.00	0.00	0	0.00	0.00	0.00	0.00

Table 5.4. Oxidation states of the metalloporphyrin as accessed by the QTAIM localization/delocalization indexes of the electrons.

		MP		MPCl		MPCN	
	Core Nuc	Loc Index	**Ox state**	Loc Index	**Ox state**	Loc Index	**Ox state**
Cr^{II}	14	11.0969	**2.9031**	10.5894	**3.4106**	10.4641	**3.5359**
Cr^{III}	14	10.9122	**3.0878**	10.5903	**3.4097**	10.5097	**3.4903**
Mo^{II}	14	10.5763	**3.4237**	9.8332	**4.1668**	9.8173	**4.1827**
Mo^{IV}	14	10.0188	**3.9812**	9.7394	**4.2606**	9.7678	**4.2322**
Os^{II}	30	26.4564	**3.5436**	25.7065	**4.2935**	25.7281	**4.2719**
Os^{IV}	30	26.1388	**3.8612**	25.6267	**4.3733**	25.6567	**4.3433**
Rh^{III}	17	13.9677	**3.0323**	13.5227	**3.4773**	13.4587	**3.5413**

Both approaches are based on defining how many electrons are localized, in this case, at the metal and how many electrons are delocalized over the whole structure. The oxidation states can be calculated directly[178, 179] from the localization and delocalization indexes as obtained from a QTAIM topology analysis.[180] As for the spin densities, these are relatively pitted against each other (metal vs porphyrin atoms) for complexes with unpaired electrons. The example for Mo^{II} complexes can be found in Scheme 5.6.

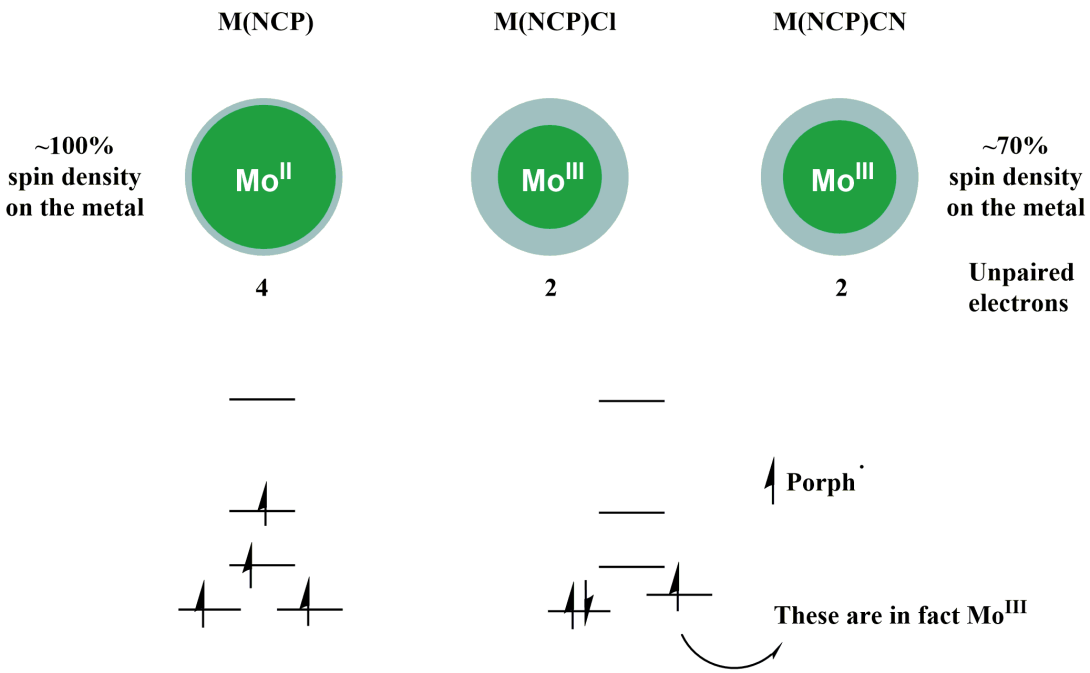

Scheme 5.6. Example for the theoretical Mo^{II} complexes of how the spin density localization can provide information on the electronic structure of the complexes.

A summary of the results can be found in Table 5.5. They show that only a limited number of oxidation states is available for most metals (Cr^{III}, Mo^{IV}, Os^{IV}) as the NCP ligand is very likely to be reduced, except for the case of rhodium in which two oxidation states can arise, $Rh^{III/IV}$.

Table 5.5. Electronic configuration of the metalloporphyrins.

	Formal electronic configuration (FEC)		
	M(NCP)	M(NCP)Cl	M(NCP)CN
Cr^{III}	$[Cr^{III}NCP]^{+}$	$[Cr^{III}(NCP)Cl]$	$[Cr^{III}(NCP)CN]$
Mo^{IV}	$[Mo^{IV}NCP]^{2+}$	$[Mo^{IV}(NCP)Cl]^{+}$	$[Mo^{IV}(NCP)CN]^{+}$
Cr^{II}	$[Cr^{III}(NCP^{\bullet})]$	$[Cr^{III}(NCP^{\bullet})Cl]^{-}$	$[Cr^{III}(NCP^{\bullet})CN]^{-}$
Mo^{II}	$[Mo^{IV}(NCP^{\bullet\bullet})]$	$[Mo^{IV}(NCP^{\bullet\bullet})Cl]^{-}$	$[Mo^{IV}(NCP^{\bullet\bullet})CN]^{-}$
Os^{IV}	$[Os^{IV}(NCP)]^{2+}$	$[Os^{IV}(NCP)Cl]^{+}$	$[Os^{IV}(NCP)CN]^{+}$
Os^{II}	$[Os^{IV}(NCP^{\bullet\bullet})]$	$[Os^{IV}(NCP^{\bullet\bullet})Cl]^{-}$	$[Os^{IV}(NCP^{\bullet\bullet})CN]^{-}$
Rh^{III}	$[Rh^{IV}(NCP^{\bullet})]^{+}$	$[Rh^{III}(NCP)Cl]$	$[Rh^{III}(NCP)CN]$

This assignation is not clear for the Rh(NCP). Therefore, we used energy decomposition analysis (EDA)[181] to further investigate the correct electronic structure in Rh(NCP) as it is not entirely clear from the spin density and localization indexes. The orbital interactions are in Table 5.6.

Table 5.6. Orbital interaction energy as calculated per EDA.

	Orbital interaction stabilization (kcal mol^{-1})
$[Cr^{III}(NCP^{\bullet})]$	-813.83
$[Cr^{II}(NCP)]$	-432.73
$[Rh^{IV}(NCP)^{\bullet}]^{+}$	-1488.07
$[Rh^{III}(NCP)]^{+}$	-935.67

EDA provided the expected result for chromium in which it shows that the $Cr^{III}(NCP^{\bullet})$ is the species with the greatest orbital stabilization. The same was observed for the Rh^{IV} species bound to a NCP radical instead of Rh^{III} analogue, confirming the assignation in Table 3.

We also attempted to study any correlation of these findings with the geometry of the NCP rings and their delocalized π system. The shape of porphyrins has been recently reviewed by Kingsbury and Senge.[182] Although they derive some intricate geometrical parameters, we have preferred to perform a continuous shape measurement (CShM) with SHAPE.[183, 184] This measurement quantifies the difference between a selected geometry, in our case the metalloNCPs, and the geometries of ideal transition-metal complexes. We compared the bare NCP complexes to the four vertices[185] polyhedral model and the axial substituted NCPs to the five vertices[186] polyhedral. Greater distortions are expected for the latter, as axial coordination on one end only seems to be capable of pulling the metal out of plane. The results can be found in Table 5.7.

Table 5.7. CShM[183] for the porphyrins when compared to the ideal geometries with code as presented in the table.

	CShM Model			
	SP-4	**SPY-5 (Cl)**	**SPY-5 (CN)**	**FEC**
Cr^{III}	0.041	0.223	0.729	**Cr^{III}**
Mo^{IV}	3.338	0.833	0.889	**Mo^{IV}**
Cr^{II}	0.017	0.244	0.797	**Cr^{III}**NCP$^{\bullet}$
Mo^{II}	0.245	0.200	0.506	**Mo^{IV}**NCP$^{\bullet\bullet}$
Os^{IV}	1.067	1.677	1.704	**Os^{IV}**
Os^{II}	0.028	0.545	1.396	**Os^{IV}**NCP$^{\bullet\bullet}$
Rh^{III}	0.058	0.701	1.732	**Rh^{III}**

The greatest distortions can be found for the square planar Mo^{IV} and Os^{IV}, as well as for square pyramidal Os^{IV}, Os^{IV}NCP$^{\bullet\bullet}$ and Rh^{III}. Indeed, axial coordination is shown to increase the CShM in general, as this effect is larger with the cyanide ligand, but nothing else was obtained from that analysis. We also compared relevant BODSEP bond orders (bond orders normalized in such a way that their sum corresponds to the total number of bonds) to those reported in previous work by some of us.[172] These results can be found in Table 5.8.

Table 5.8. Comparison between relevant BODSEP bond orders of the porphyrin (Por) dianion, the corresponding 2H-N-confused porphyrin dianion, and their metal complexes.

	G-J BODSEP bond orders				
	M-C	**M-N**	**N-C_α**	**M-N_c**	**M-X****
*Por^{2-}	-	-	1.329	-	-
NCP-2H^{2-}	-	-	1.419	-	-
*M(Por) *Avg*	-	0.408	1.330	-	-
M(NCP) *Avg*	0.960	0.542	1.255	0.322	-
M(NCP)Cl *Avg*	0.900	0.556	1.241	0.332	0.777
M(NCP)CN *Avg*	0.890	0.540	1.249	0.297	0.915

NCP-2H is said to be less aromatic than porphyrin. When one compares their dianion analogues, one can note that there is an increase in N-C_α bond order. If one assumes that the ideal aromatic value for these mixtures of single and double bonds is 1.5,[172] the anion of the NCP would seem to be more aromatic than that of porphyrin, which is contradictory. While metal coordination was shown to, on average, not influence this bond order, the same is not true in the case of NCP, as there is a slight decrease in the BODSEP of the N-C_α bond. The lateral M-N bond orders are comparable between the NCP complexes and those with porphyrin, but the M-C bond is exceptionally strong, thus weakening the opposite M-N bond, as can be noted by average bond order values close to 0.300. Unsurprisingly, the bond between the metal and the high-field ligand is stronger than that of the metal-chloride.

The porphyrin absorption spectrum shows a triade of smaller intensity bands at higher wavelengths, the Q bands, and an absorption maximum at a higher energy wavelength, so called Soret band (B band). This spectrum has been

tentatively interpreted with a four-orbital model originally proposed by Gouterman,[187] which states that these bands arise from π–π* transitions between the HOMO/HOMO-1 and the LUMO/LUMO+1 pairs, with varying degrees of bonding and antibonding character depending on substituents, and the effect of such ring substituents and metal coordination has been revisited by other computational chemists (Scheme 5.7, left).[188, 189]

We will thus be performing a similar analysis for the N-confused isomer and respective metalloNCPs. The comparison between the Soret band region of normal porphyrin, the NCP-2H isomer and the corresponding dianion, NCP-2H^{2-}, is in Figure 5.2. All the spectra presented in this section were calculated in DMF, as it is the solvent in which the confused porphyrin isomer was isolated.

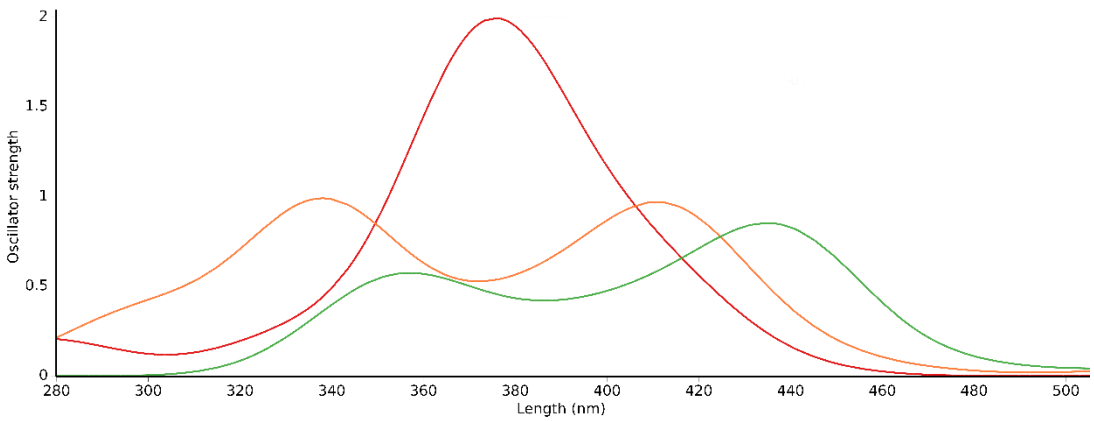

Figure 5.2. Absorption spectra (dimethylformamide) calculated in the Soret band region of porphyrin (red) NCP-2H (orange) and its dianionic form (green). Band width = 40 nm, Gaussian height broadening.

The single band that was obtained for porphyrin around ca. 375 nm is in good agreement with the literature. This band appears to split into two bands with

lower absorption values, in both NCP-2H and its dianionic form. However, if the average between the two absorption peaks is taken, porphyrin and its N-confused isomer have similar energies (porph ~375 nm, NCP-2H ~375 nm) and a small bathochromic shift is expected for the free base (free base ~400 nm). Scheme 5.7 provides a more in-depth investigation of the origin of these bands.

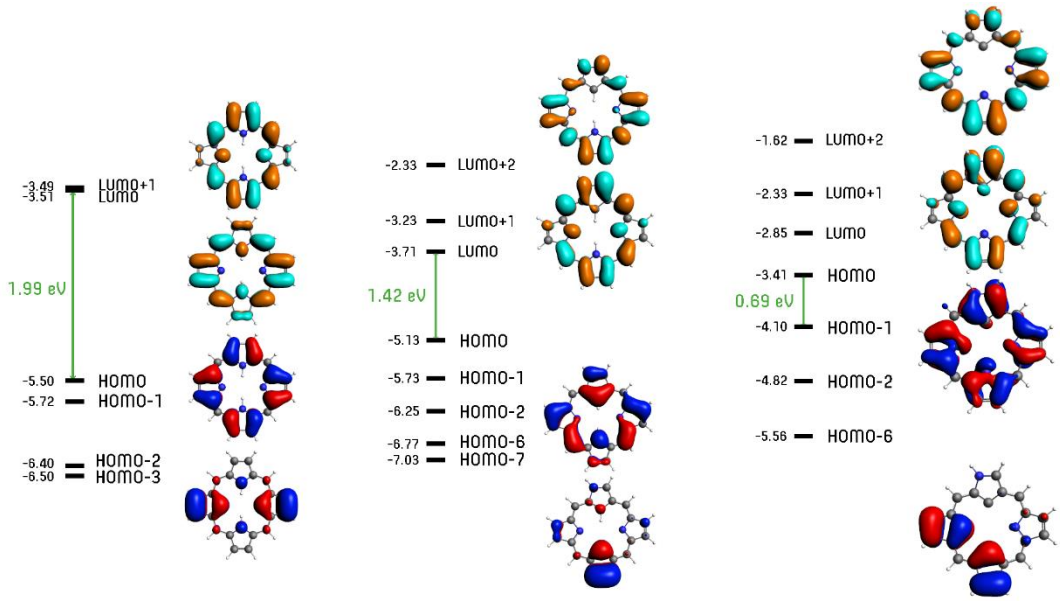

Scheme 5.7. Frontier orbital diagram for porphyrin (left), NCP-2H (center) and NCP-2H^{2-} (right). The orbitals involved in the Soret-band associated electronic transitions are depicted next to the corresponding diagram.

Despite the decrease in the HOMO-LUMO gap that is clearly noticeable from left to right in Scheme 5.7, what seems to contribute most to the differences in the calculated UV-Vis spectra is the decrease in the symmetry level of the N-confused monomer when compared to normal porphyrin. The orbitals involved in the electronic transitions of porphyrin are highly symmetric, cover most of the ring and agree with the four orbital model that states the orbitals involved

in the transitions should be in the frontier region (HOMO-3, HOMO-2). The same is not true, however, for the N-confused isomer. The decrease in ΔHOMO-LUMO explains the lowest energy band observed at ca. 410nm, but electron transitions accounting for a higher energy band (ca. 340 nm) are also noted. These electrons stem from orbitals that are much lower in energy (HOMO-7), in contradiction with the four-orbital model. A similar phenomenon is observed for the dianion.

No significant changes are observed between the UV-Vis spectrum of the dianion NCP-2H^{2-} and most of the transition metal complexes, except for the Rh complexes. These are shown in Figure 5.3.

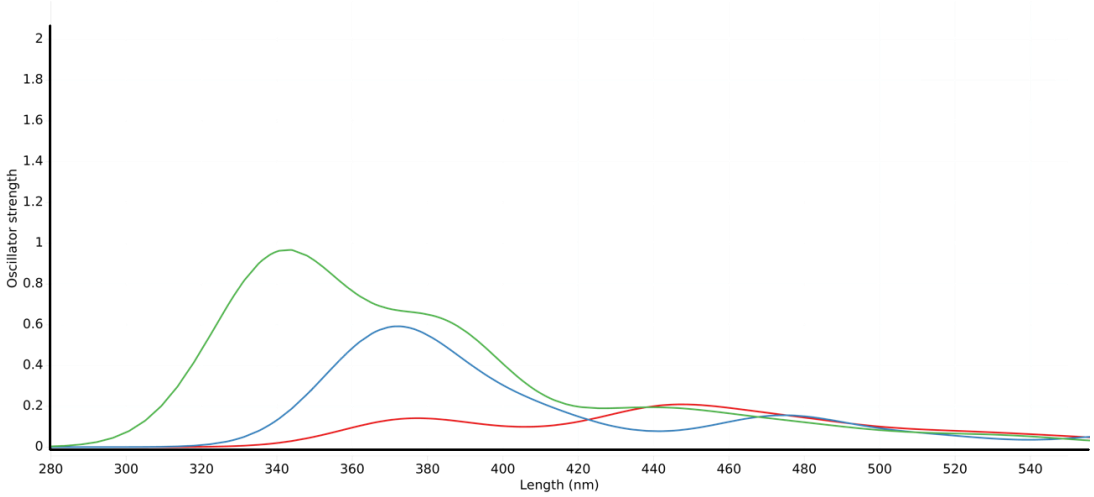

Figure 5.3. UV-Vis spectra calculated in the Soret band region of (NCP)M (red), (NCP)M-Cl (blue) and (NCP)M-CN (green) for the Rh metal complexes. Band width = 40 nm, Gaussian height broadening.

The spectra in Figure 5.3 show a large ligand to metal charge transfer band that occur from π orbitals in the NCP ring to the d_{z2} metal orbital. The introduction

of an axial ligand in the Rh(III) NCP not only increases the intensity of the band, but also its energy. This increase seems to be correlated with the strength of the field induced by the axial ligand which suggest it may be tuned.

Figure 5.4 contains the ΔHOMO-LUMO for the bare and substituted metalloNCPs.

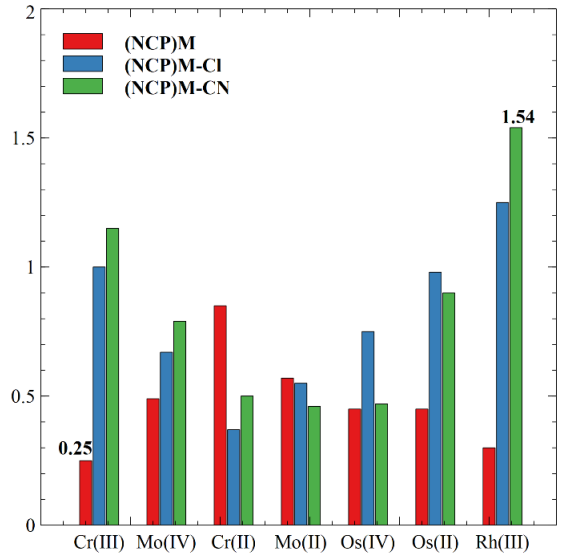

Figure 5.4. HOMO-LUMO gaps for all the complexes in this work (energies in eV).

The HOMO-LUMO gap for NCP-2H is 1.42 eV as per Scheme 5.7. Analogous Zn and Mg complexes were reported to have HL gaps of (2.25 was obtained for the isomer NCP-2H) 2.21 eV and 2.14 eV.[190] The same result was obtained here, coordination to the transition-metal decreases this gap in all cases (Figure 5.4). However, as NCP-2H and its metal complexes do not exhibit the same Gouterman-type frontier orbitals, this parameter alone is not sufficient to

explain their spectra. Most of the metal complexes have frontier orbitals that also have mostly a NCP ring character and π–π* transitions occur, but that is not true for Os(II) or Rh(III), where both HOMO and LUMO are mostly located around the metal. In such cases the ligand π* orbitals are in turn LUMO+2.

The two cases in which there is a massive increase in the gap from the normal to the Cl are Cr(III) and Rh(III). In both cases there is a massive destabilization of the LUMO orbital with respect to the HOMO (225% and 351% respectively) upon Cl coordination and this phenomenon is exacerbated further with the higher field ligand. The gap only decreases in Cr(II) and Mo(II). In both cases, the HOMO and LUMO orbitals for normal and the axial ligand analogues are very similar. They also have the same spin ground states for the bare NCP and Cl-coordinated (S=2 and S=1). Mo(II) has a smaller difference in H-L gap due to the largest destabilization of the LUMO orbital in regards to the HOMO in the Cl complex (143% vs 109%).

We also decided to study the redox chemistry of the Rh(NCP) radical. The $[Rh^{III}(NCP)]^+$ complex is best described as $[Rh^{IV}(NCP^{\bullet})]^+$ and it has been established that for Cr, Mo and Os a single oxidation state is accessible as the remaining redox chemistry occurs in the NCP ring. It is thus interesting to see what happens upon reduction and oxidation of the rhodium N-confused porphyrin as two oxidation states ($Rh^{III/IV}$) seem to be accessible. The reduction of $[Rh^{IV}NCP^{\bullet}]^+$ yields the neutral $[Rh^{II}NCP]$ doublet which is more stable than the quartet by ca. 27 kcal mol^{-1}. The oxidation of $[Rh^{IV}NCP^{\bullet}]^+$ yields a mixed configuration of quartet (more stable by ca. 0.04 kcal mol^{-1}) and doublet. The

quartet corresponds to the oxidation of the metal to a FEC of $[Rh^{V}NCP^{\bullet}]^{2+}$ while the doublet is an oxidation of the NCP ligand, yielding the $[Rh^{IV}NCP]^{2+}$ species.

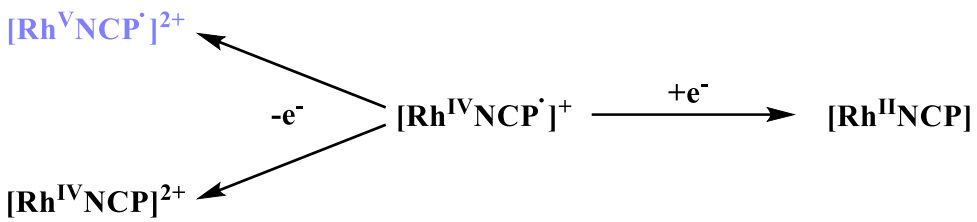

Scheme 5.8. Redox chemistry of the bare Rh N-confused porphyrin complex.

We can now say that the electronic distribution and optical properties of the N-confused NCP-2H isomer and their transition metal complexes were analyzed. Our computational method proved to be successful in the description of both the geometries and spin states of known similar porphyrins. The spin state of the putative N-confused metalloporphyrins was shown to depend mostly on the total number of unpaired electrons and the same spin state was obtained for NCPs with seemingly equal number of *d* electrons, even with metals from different rows of the periodic table. An analysis of the electronic distribution in the bare metalloNCPs unveiled the redox character of the N-confused porphyrin. The introduction of an axial ligand was shown to affect the spin state of d^4 and d^6 complexes, as expected, but the effect is independent of the strength of the axial ligand field. Although in the porphyrin the electronic transitions associated to the B band region arise from frontier orbital excitations, the same is not true for NCP-2H or its metal complexes. This is problematic as the simple $\Delta_{HOMO-LUMO}$ gap analysis that is usually performed for the comparison of porphyrin derivatives is no longer possible for the N-confused analogues, the actual orbitals involved in the transitions must be

studied as well. Here, the relative energy between the metal and ligand orbitals seems to be the determining factor: d^2, d^3, d^4 and Os(II) complexes showed a UV-Vis spectrum very similar to that of the dianion NCP-2H$^-$, while the d^6 Rh complexes showed a large LMCT band that is deeply affected by the axial destabilization of the metal *d* orbitals.

Chapter 6

Ni-halide C-H activation

6. Ni-halide C-H activation

This work has been developed in collaboration with the group of Prof. Aidan McDonald, from Trinity College Dublin (TCD).

6.1. State of the art

The activation of C-H bonds with high bond dissociation energies (BDEs) is of the utmost importance for the chemical industry due to the chemical space exploration that it allows and one of the most efficient methods to perform it is resorting to transition metal complexes.[191] While some of the most iconic C-H activation reactions are performed with noble metal catalysts,[192] their high cost and environmental footprint led to the development of more sustainable catalysts, a field which is dominated by bio-inspired iron-oxo complexes.[193]

More recently, however, McDonald and coworkers reported another sustainable catalyst candidate, a high-valent Ni^{III}-Chloride complex which is capable of activating both C-H and O-H bonds through an apparent hydrogen atom transfer (HAT) mechanism.[194] The bonds activated had BDEs up to ca. 85 kcal mol^{-1} and exhibited varying reaction rates, depending on the BDE. They postulated that tuning the halogen ligand in the catalytic species could lead to better performing catalysts.

In this work, we use DFT with a functional that excels in spin-state description[83] to characterize the reactivity of the Ni complex reported by McDonald and

coworkers and dive further into the chemical space to probe for more efficient derivatives (Scheme 6.1).

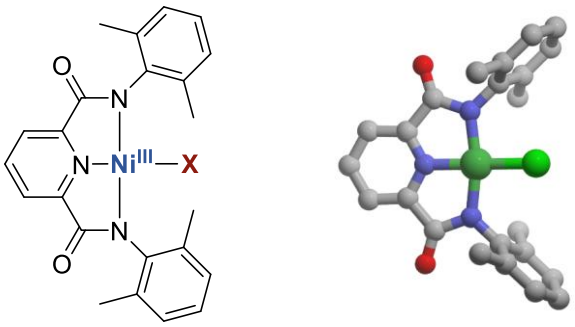

Scheme 6.1. General scheme for these complexes where X=Cl and F (left) and ground state (DFT, S=0) structure for the Ni-Cl, H atoms omitted for the sake of clarity.

6.2. Computational method

DFT calculations were performed using the ADF/QUILD[130-132] program packages. Scalar relativistic corrections were employed using the Zeroth Order Regular Approximation[104] (ZORA). Solvent effects were included with the Conductor-like Screening Model[133] (COSMO) for acetone. Geometry optimizations, frequency and single-point calculations were done with the S12g[83] functional and a triple-ζ basis set with double polarization functions[134] (S12g/TZ2P). Vibrational modes below 100 cm^{-1} were raised to this value when calculating Gibbs energies, to compensate for the breakdown of the harmonic oscillator model.[106]

6.3. Results & discussion

Our first concern was identifying the ground spin state of the Ni-Cl complex. It turned out to be the low-spin state and a significant structural rearrangement of the complex would be required for the transition to occur (Figure 6.1).

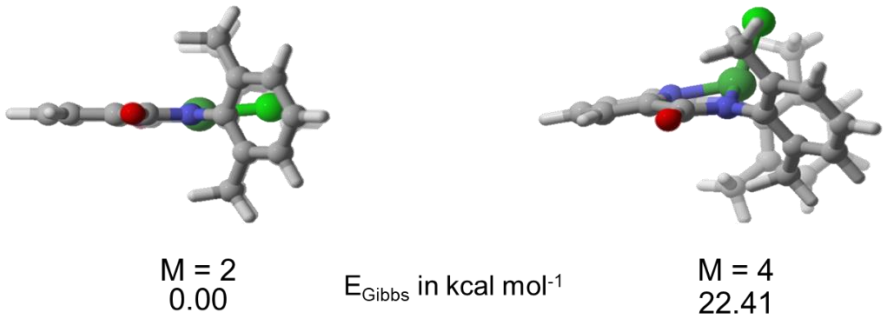

Figure 6.1. Relative energies for S=½ and S=3/2 of the Ni-Cl complex.

This spin transition involves a decrease in the N-Ni-Halogen angle from 175° to ca. 120° and an elongation of 7% of the Ni-N bonds (ca. 0.130 Å). The same was true for the fluoride analogue. A difference of 26.61 kcal mol^{-1} favored the low-spin S=½ state. A comparison of the structural parameters for this complex can be found in Table 6.1.

Table 6.1. Structural data for the Ni-F complex. Bond lengths in angström, angles in degrees.

Bond	Crystal	DFT (S = ½)	DFT (S = 3/2)
Ni-N_1	1.819	1.821	2.009
Ni-$N_{2,3}$	1.919	1.862	2.043
Ni-F	1.808	1.814	1.853
N-Ni-F	179.33	179.53	178.17

There is a clear agreement between the low-spin DFT optimized structure and that obtained via single crystal X-ray crystallography. The largest bond difference between the LS structure and that obtained experimentally was found to be 0.057 Å and the N-Ni-F angle is approximately the same, while for the HS structure 0.045 Å is in fact the smallest bond length difference (Ni-F) and disparities up to 0.190 Å are observed (Ni-N_1). As we had identified the low-spin state to be the ground-state for both complexes, since both the energies and structures were comparable to those reported, we sought the mechanism for the hydrogen abstraction. The most obvious proposal, based on the experimental finding that hydrochloric acid was released upon hydrogen abstraction, can be found in Scheme 6.2.

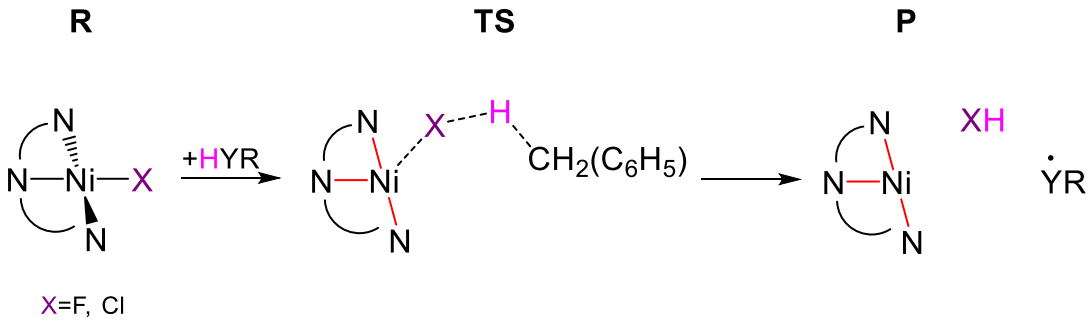

Scheme 6.2. Mechanistic proposal for the abstraction of a hydrogen from a C-H bond with the high-valent nickel complex.

We expected a single transition state (TS) with simultaneous elongation of the Ni-X and C-H bonds and indeed this is what we found. The product that is obtained is already considering the release of XH, which is clearly reported in the experiments. Additionally, a spin-state change between the reactants (R) and the TS could take place. The BDE for the Ni-Cl bond was estimated to be between 25 and 30 kcal mol^{-1} via calculation of the potential energy surface of the lengthening of this bond and as such a barrier over this value would have no chemical relevance. We calculated the thermodynamics of the reactions in the two spin surfaces for the complex with both halogens (Cl and F) and the C-H activation of 1,4-cyclohexadiene (1,4-CHD). These can be found in Table 6.2. It is important to remember that the reactions were reported to occur at -40 °C and as such reasonably low barriers should be obtained.

Table 6.2. Reaction barriers and Gibbs energies for HAT of 1,4-cyclohexadiene with the Ni^{III}-X complexes. Values in parenthesis account for the spin transition.

Multiplicity	X	$\Delta G^{\ddagger}$ / kcal mol^{-1}	ΔG / kcal mol^{-1}
2	Cl	Not found	
	F	18.53	7.16
4	Cl	10.14 (32.55)	9.97 (32.38)
	F	7.16 (33.77)	-0.04 (26.57)

The fact that the reactions are endergonic up to this point is not surprising, as they are not complete – a second hydrogen abstraction or radical rebound step is required for the reaction to follow its course. In fact, we have calculated this to be exergonic by ca. 12 kcal mol^{-1}. However, to compare the reactivity of the

Ni-Cl with the Ni-F, the analysis should be focused on the reaction barrier of the first transition-state as that is, in principle, the determining TS responsible for the hydrogen abstraction. Immediately, one can see that we were not able to find a maximum in the M=2 surface of the chloride complex. This is problematic as, if it does not exist, that suggests that the reaction involves a spin transition, which has an additional energy barrier that should be considered. The hydrogen abstraction by the fluoride doublet has a barrier of ca. 19 kcal mol^{-1} which seems reasonable for a putative reaction below room temperature. We were, however, able to identify the two PES maxima in the M=4 surface. The notable result is that the fluoride complex has a smaller activation barrier (by ca. 3 kcal mol^{-1}) and would thus exhibit a greater reaction rate if the reactions proceeded via this spin surface. It is, however, not the case, as it increases from 7.16 to 33.77 kcal mol^{-1} upon addition of the spin gap energy.

Considering that we were only able to find a TS for the quartet surface of the Ni-Cl compound and the objective of this work was to compare both catalysts, we calculated all the reaction barriers in this spin state, for both the C-H and O-H activations (Table 6.3), in the hopes that the results are analogous in the doublet surface.

Table 6.3. Reaction barriers for the complexes (S=3/2). BDE increasing downwards. DTBP = di-tert-butylphenol.

Bond	Substrate	$\Delta G^{‡}$ (Cl) / kcal mol^{-1}	$\Delta G^{‡}$ (F) / kcal mol^{-1}
C-H	1,4-CHD	10.14	7.16
	Xanthene	10.64	10.45
O-H	*p*-Me-2,6-DTBP	17.02	4.04
	p-H-2,6-DTBP	20.04	7.11
	p-Br-2,6-DTBP	18.34	6.03

Two C-H and three O-H activations were analyzed and the substrates are organized in the table in such a way that the BDE is increasing from top to bottom. We obtained qualitative agreement between BDE and activation barriers. Also, we noted that not only for CHD, but also for all the other substrates, the barrier calculated for the Ni-F complex was lower than its chloride analogue, providing further proof that it should be a better candidate to perform this non-catalytic reaction.

The failure in finding a suitable TS for the Ni-Cl doublet led us to explore an alternative mechanism for this reaction (Scheme 6.3). It involved the abstraction of the hydrogen by the ketone of the ligand arm followed by several proton migrations. Nonetheless, a barrier of ca. 57 kcal mol^{-1} was obtained for the proton migration from the oxygen in the ligand ketone to the nickel-bound nitrogen and it was thus ruled out.

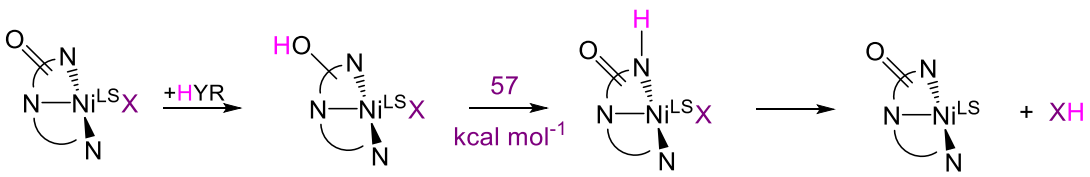

Scheme 6.3. Alternative mechanism for C-H activation.

Two other strategies were attempted: the coordination of an explicit solvent molecule to the metal on the opposite side of the interaction with the substrate and a rotation of the ligand arm in such a way that it would be ketone and not amine coordinated. The former resulted in no change in the reaction profile

calculated and the newly found intermediate was found to be ca. 16 kcal mol^{-1} higher in energy than the amine coordinated arm and hence was ignored.

Ultimately, we were not able to properly model the reactivity of the Ni-Cl complex. The choice of method could be a source of error, as hybrid functionals were also employed and failed to even find a local maximum on the potential energy surface, given the structure of the GGA-optimized TS for the Ni-F compound. Later, our experimental colleagues synthesized and characterized the reactivity of the fluoride complex and indeed it proved to have higher reaction rates than the Ni-chloride.[195] Furthermore, Sun, Nam and coworkers published a very recent study[196] (UB3LYP/B2) precisely on the mechanism of operation of these two molecules for HAT of 1,4-CHD. They obtained much smaller spin gaps for the Cl and F metal complexes (11.7 kcal mol^{-1} for both) and TSs with a large disparity in Ni-X-H angle (114.9° for Ni-Cl as opposed to 177.5° for Ni-F), but confirmed our findings that the proposed mechanism (Scheme 6.2) was indeed correct. It is interesting to note that despite obtaining the TS at the correct spin surface for the Ni-Cl complex, its structure is much closer to the one that we have obtained for the quartet. The reaction barriers were 15.6 for F and 20.4 for Cl. They concluded it was a HAT and not cPCET as no π-interaction between the metal-halide and the substrate was found along the reaction coordinate.

Chapter 7

High-valent Iron species characterization

7. High-valent Iron species characterization

This work has been developed in collaboration with the group of Prof. Christine McKenzie, from the University of Southern Denmark (SDU) and coworkers.

7.1. State of the art

High-valent biomimetic iron complexes present themselves as green alternatives for the catalysis of strong C-H bonds due to the availability and accessibility of the metal. When performed in the gas phase, such reactions are easier to study and control as there are no intermolecular interactions that may affect the reactivity in a positive or detrimental fashion. This has been successfully shown for two systems:[197, 198] an iron(V) nitrido complex that was capable of removing two hydrogen atoms from cyclohexadienes and transferring the nitrogen of the nitride ligand to olefins and the iron(IV) oxo complex $[Fe^{IV}O(bpg)]^+$ (bpg = *N,N′*-bis(2-pyridylmethyl)-3-aminoacetate), that was shown to react selectively with C-H bonds in volatile alcohols. The latter finding was of particular interest due to this selectivity that excluded O-H bonds. Laser ablation-generated iron oxide ions had shown much greater reactivity towards alcohol O-H bonds[199] (not C-H) but they have the additional disadvantage of not being a suitable reference for comparison to condensed phase chemistry. The differences in selectivity and potency of these molecules can only be attributed to the effect of the bpg ligand, both the electronic effects derived from the ligand field and the structural support. It would thus be of great interest to synthesize other Fe^{IV}=O complexes with ligands capable of

providing equal structural support, but with different electronic properties, to study how this affects the reactivity of the metal-oxo moiety towards organic substrates in the gas phase.

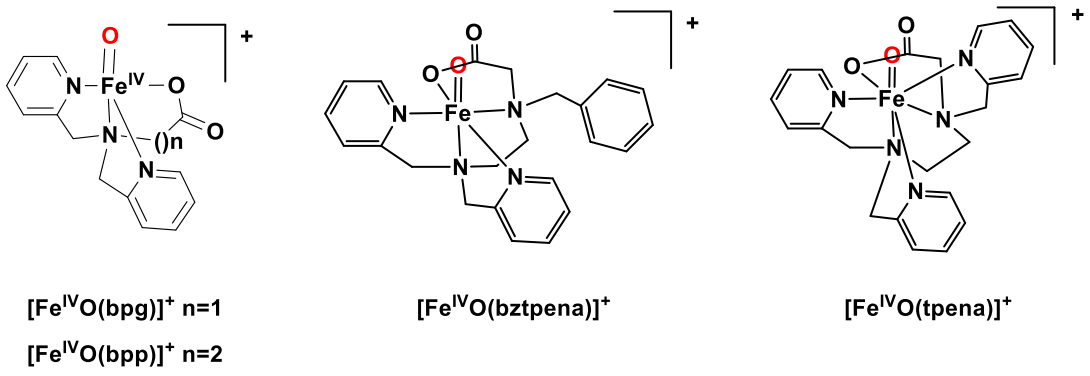

Scheme 7.1. Fe-oxo monomers that we hoped to obtain as products of gas-phase disproportionation.

McKenzie and coworkers investigated the UV photodissociation action spectra and gas phase reactivity of putative analogues of biomimetic iron complexes with varying ligand ring sizes and structures (Scheme 7.1) generated via gas disproportionation of precursor oxo-bridged dimers. However, the characterization of the complexes obtained was exceedingly difficult as the spectroscopic techniques available in the gas phase are extremely limited.

7.2.Computational method

DFT calculations were performed in the gas phase using the ADF/QUILD[130-132] program packages. Scalar relativistic corrections were employed using the Zeroth Order Regular Approximation[104] (ZORA). Geometry optimizations, frequency, single-point and TD-DFT calculations were done with the S12g[83]

functional and a triple-ζ basis set with double polarization functions[134] (S12g/TZ2P). Vibrational modes below 100 cm^{-1} were raised to this value when calculating Gibbs energies, to compensate for the breakdown of the harmonic oscillator model.[106]

7.3. Results & discussion

The first part of this work consisted of the characterization of the precursor dimers. The gas phase electronic structure for the series of $[Fe_2(\mu\text{-}O)(N_xO)_2]^{2+}$ complexes was probed using gas phase Ultra-violet Photodissociation (UVPD) action spectroscopy in the 220-520 nm range. The absorption results are plotted as a function of wavelength in Figure 7.1, left. In two sets, distinctly different λ_{max} were observed for $[Fe_2(\mu\text{-}O)(bpg)_2]^{2+}$, $[Fe_2(\mu\text{-}O)(bzpbena)_2]^{2+}$ and $[Fe_2(\mu\text{-}O)(tpena)_2]^{2+}$ ($[Fe_2(\mu\text{-}O)(N_xO)_2]^{2+}$ X = 3, 4 and 5 respectively). One set of these appear at 349 nm ($Fe_2(\mu\text{-}O)(tpena)_2]^{2+}$) and two at 364 nm for $[Fe_2(\mu\text{-}O)(bpg)_2]^{2+}$ and $[Fe_2(\mu\text{-}O)(bzpbena)_2]^{2+}$. Two bands in the UV region appear repeat the pattern of absorptions for $[Fe_2(\mu\text{-}O)(N_xO)_2]^{2+}$ X = 3, 4 appearing at the same position (ca. 250 nm and 230 nm). Again bands in this region for $[Fe_2(\mu\text{-}O)(tpena)_2]^{2+}$ are distinctly different at 260 nm and possibly at 220 nm or below.

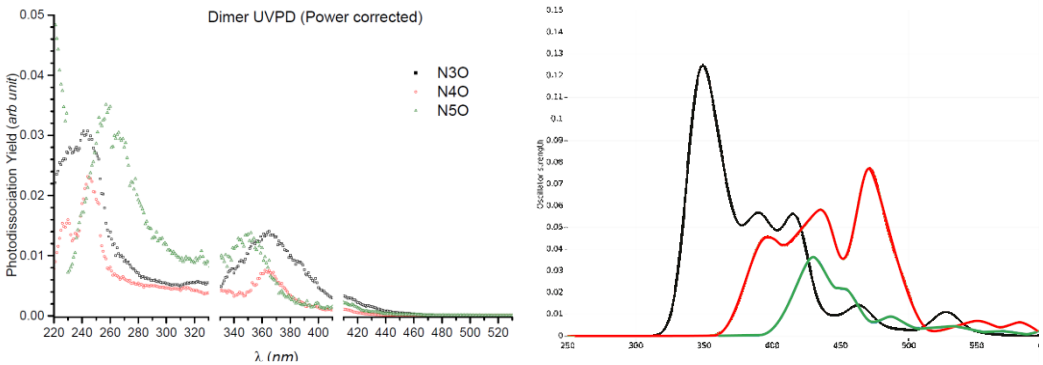

Figure 7.1. UV-vis spectra obtained experimentally (left) and computationally (right) for the oxo-bridged dimers with bpg (black), bztpena (red) and tpena (green) ligands.

The UV-vis spectra of the three dinuclear compounds in their singlet state was also calculated with DFT (S12g/TZ2P, Figure 7.1, right). All three complexes exhibit a band at ca. 750 nm which is usually associated with Fe(IV)=O complexes (not shown here). This band can be observed at 750, 782 and 781 nm for the bpg, bztpena and tpena complexes, respectively. In the case of bpg and tpena, they represent a ligand to metal charge transfer from the HOMO, located mainly on the carboxylate arm of one of the ligands, to a metal/oxo d_{z^2}-π combination (Figure 7.2). With the bpp ligand, however, the same orbital is instead the HOMO-1, and the transition occurs to a metal/oxo $d_x/d_y/d_z$-π combination. The band which is observed at ca. 350 nm in the UVPD results, corresponds to the band with the highest oscillator strength in the DFT results. It is found at 346, 432 and 468 nm for bpg, bztpena and tpena respectively. While for bpg and bztpena it concerns again a ligand to metal charge transfer phenomenon, now from a pyridine ring π-system to a metal/oxo $d_x/d_y/d_z$-π combination (Figure 7.2), in the case of tpena the electron is excited from the

combination of the σ orbital of the oxygen in the Fe-O-Fe bridge and the π of the carboxylate oxygens. While the bpg and bpp peaks are in fact in close proximity, in agreement with experiment, the peak obtained for tpena appears at a higher wavelength than those formerly mentioned.

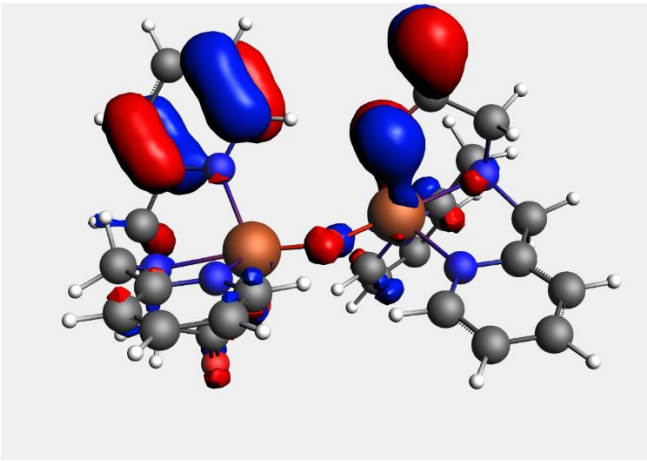

Figure 7.2. Highest-occupied molecular orbital of the dimeric complexes with bpg and tpena. It corresponds to HOMO-1 in the case of the analogous complex with the bztpena ligand.

Collision-induced dissociation spectra for the bpp, bztpena and tpena supported systems were recorded and that of the bpg-supported system had been reported in their initial study.[198] Under identical conditions, it was noted that the dimer assembled with the bpg ligand would fragment to a greater extent than the others, as its relative abundance was higher than the remaining ions (dissociation products). This suggests that $Fe_2O(bpp)_2]^{2+}$ has a relatively higher Fe-O-Fe bond strength in the gas phase compared to, for instance, $[Fe_2O(bpg)_2]^{2+}$. The product iron(IV)oxo complexes $[Fe^{IV}O(bpg)]^{+}$ (m/z

328.3081) and the tentatively assigned $[Fe^{IV}O(bpp)]^+$ (m/z 342.0534) were also obtained, confirming the disproportionation. Gopinathan-Jug bond order analysis[200] was performed for three dinuclear complexes to verify the relative stability of the Fe-O bonds. The results obtained can be found in the table below (Table 7.1).

Table 7.1. Gopinathan-Jug Fe-O bond orders for three of the dinuclear μ-oxo bridged compounds.

Ligand	G-J Bond Order	Fe-O distance / Å
Bpg	0.513	1.784
Bpp	0.533	1.794
Tpena	0.837	1.817

Indeed, bpp has a higher Fe-O bond strength than that found in the bpg complexes. The difference observed for the bond orders obtained is similar to that found for the bond distances, hence the mass spectrometry results are in full agreement with the computational results for the structure and the nature of the iron-oxo bonds.

As the electronic and structural characterization of the dimers was finished, we then turned to the electronic characterization of the iron (IV) product monomers. The experimental UVPD spectrum was recorded (Figure 7.3).

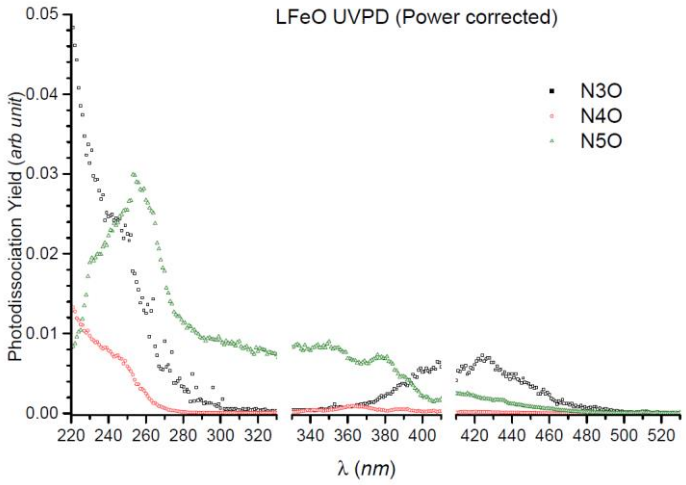

Figure 7.3. UVPD for the bpg (black), bpp (red) and tpena (green) monomeric complexes.

A similar band around 250 nm is observed for the monomeric iron-oxo complexes with the bpg and bpp ligands, however, the bpg complex showed an additional wide band centered at ca. 420 nm. The spectrum recorded for the compound with the tpena ligand was significantly different, as its absorption maximum was slightly red shifted to ca. 260 nm, exhibiting a shoulder around 240 and thus a completely different shape.

To confirm the assignment of the UVPD spectrum to the appropriate structures, the excitations were calculated for the Fe(IV)=O quintets (Figure 7.4). The four complexes exhibit a band at ca. 750 nm typical for Fe(IV)=O complexes. It appears at 718, 714, 755 and 822 nm for bpg, bpp, bztpena and tpena respectively. In all four cases it corresponds to a ligand to metal charge transfer from the carboxylate/oxo π-orbitals to a combination of the d_{z^2}/oxo-σ orbitals. The bpg and bpp complexes both exhibit a band at 377 and 386 nm

respectively which corresponds to charge transfer from the carboxylate oxygen π-orbitals to the pyridine rings. The strongest excitation on the bpg complex is observed at 326 nm, a LMCT phenomenon from the carboxylate oxygen π-orbitals to a combination of metal-oxo $d_x/d_y/d_z$ - π orbitals. The peak observed at 338 nm in the bpp spectrum also shows LMCT but it is from the pyridine rings π-system to a metal-centered $d_x/d_y/d_z$ orbital instead. In the case of tpena, two relevant LMCT bands are observed at 398 and 431 nm. The latter is similar to the bpg excitation from the pyridine rings π-system to a metal-centered orbital. The former corresponds to the excitation of electrons from carboxylate oxygen and pyridine rings π-orbitals to a combination of metal-oxo $d_x/d_y/d_z$ - π orbitals.

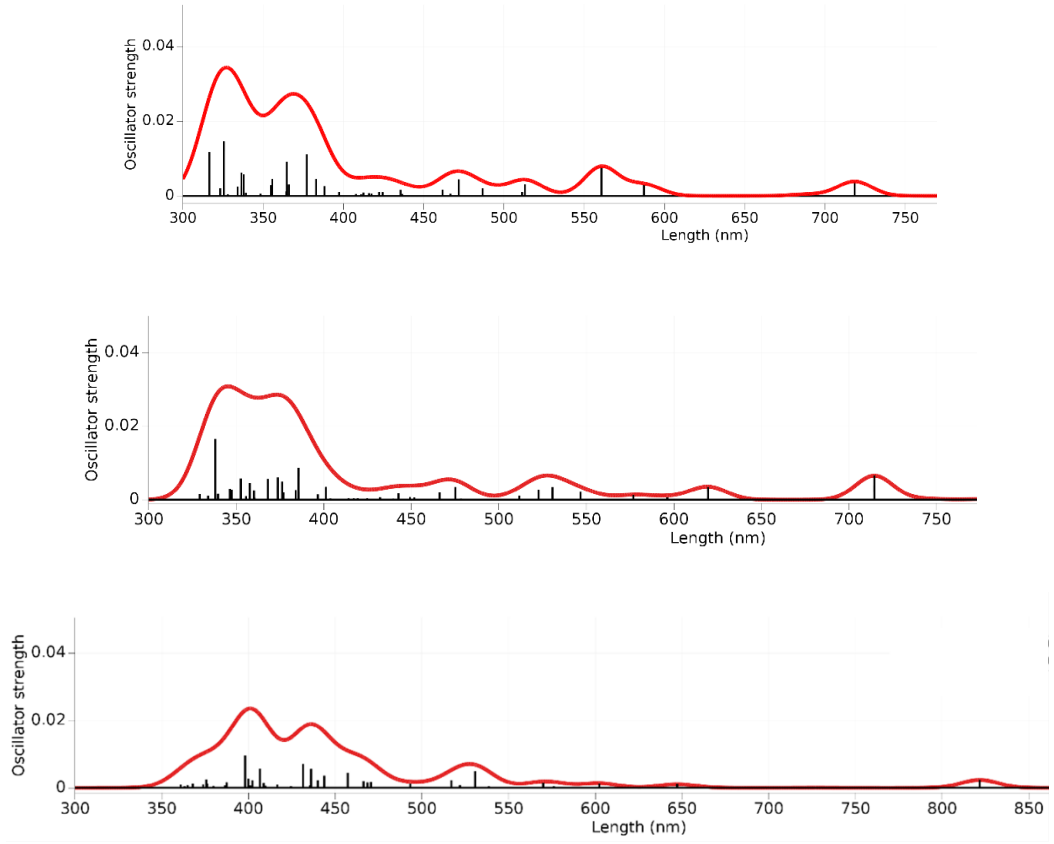

Figure 7.4. Quintet state excitation spectra for bpg (top), bpp (middle) and tpena (bottom) monomeric products.

In spite of being ca. 100 nm red shifted, this is in qualitative agreement with the experimental data: the shapes and absorption peaks of the bpg and bpp complexes are very similar and the tpena complex again has its main absorptions at higher wavelengths.

The spectra were calculated for the triplet state as well. The results can be found below (Figure 7.5). In the case of the triplets, a strong band is observed at ca. 500 nm which is not observed experimentally. The strong band at ca. 325 nm is

shifted to higher wavelengths in the cases of bpg and bpp. The tpena spectra for the two spin states show completely different profiles. We thus hypothesize that a correct assessment of the spin-state was done for the monomeric complexes.

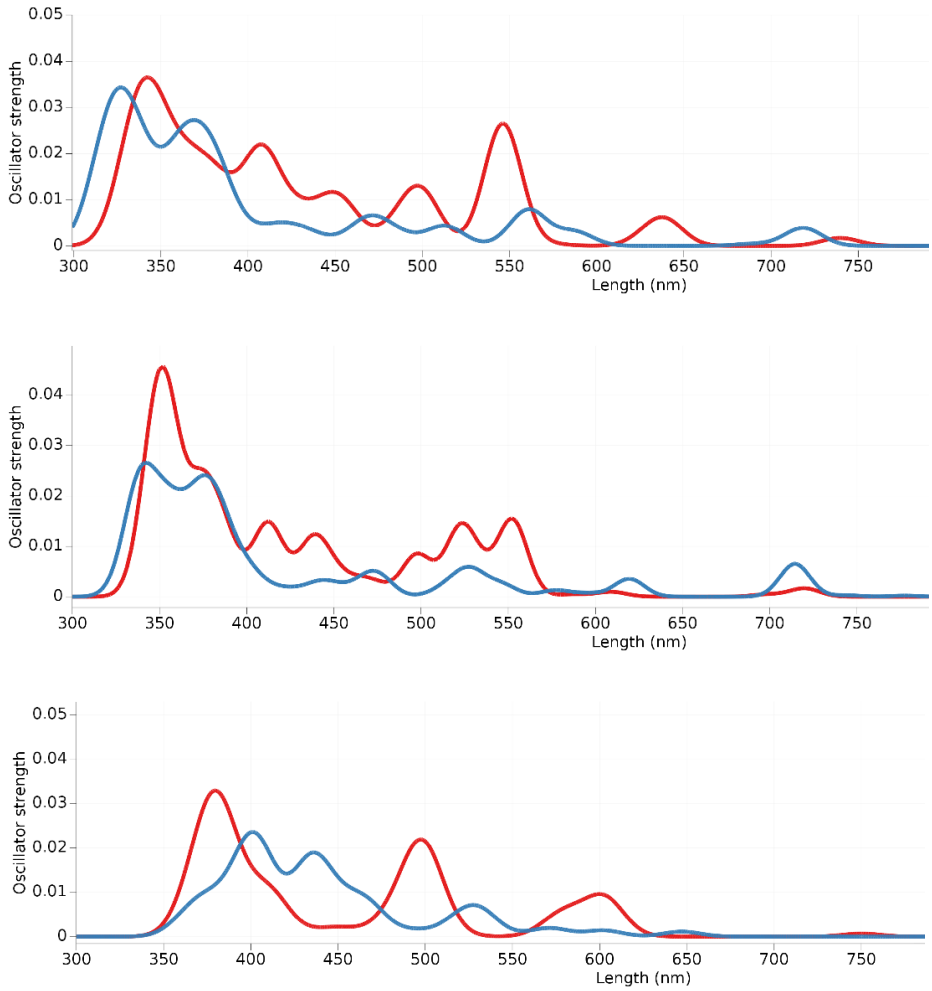

Figure 7.5. Comparison between the quintets (blue) and triplet (red) states of bpg (top), bpp (middle) and tpena (bottom) monomeric products.

In this work we were able to aid in the characterization of both μ-oxo-bridged iron dimers and their dissociation product iron-oxo monomers. The spin-state of the complexes was confirmed with DFT calculations as well as the structural assignments suggested by the mass spectrometry results. Even though there was not a quantitative match between calculated and experimental UV-vis spectra, we were able to qualitatively match the spectra to the correct complex and spin-state and to identify the excitations involved in the peaks and bands that had been recorded.

Chapter 8

Cooperative effects between transition metals and Lewis acids for the activation of dinitrogen

8. Cooperative effects between transition metals and Lewis acids for the activation of dinitrogen

This work has been developed within the scope of an HPC-Europa3 fellowship that involved a 4-month research stay at the group of Prof. Vera Krewald, at the Technische Universität Darmstadt (TUD), Germany.

8.1. State of the art

As stated in the introduction, the reduction of atmospheric dinitrogen to ammonia is extremely important for human life, but this chemical transformation is performed with great (fossil) energy expenditure nowadays. Single transition-metal complexes have struggled to conduct this reaction in ambient conditions and, alas, cooperativity-based strategies have arisen.[201-207] Cooperativity can be achieved in bimetallic complexes with two asymmetric metal coordination spheres,[208, 209] with the idea that the resulting orbital interactions and electronic structure will allow for new modes of activation. A few heterobimetallic complexes (metal oxides), with the heavy metal combinations Re/Ti[210] or Re/Mo[211, 212] have been reported to weaken the N_2 bond. However, to the best of our knowledge, the only heterobimetallic complexes with an N_2 bridge and first-row transition metal complex that have been synthesized are the much more recent chromium and iron Re-N_2-metalloporphyrins reported by Zhang and coworkers.[213]

A different strategy exploiting cooperativity relies on Lewis Acids (LAs). A Lewis acid is defined by IUPAC[214] as an electron-pair acceptor, and this ability can in principle contribute to the weakening of adjacent chemical bonds. In fact, Lewis acids have been reported to have a "pulling" capability,[215-219] making them viable candidates for building blocks in cooperative molecular entities: a transition metal complex is used as an electron donor and a Lewis acid as an electron acceptor.[220-222] This so-called "Push/Pull" strategy has proven quite successful in the weakening of the N_2 bond, in particular with borane Lewis acids,[223, 224] as the sp^2 orbital of boron is vacant and thus may take electron density from the dinitrogen bridge while the filled π orbital is implicated in π-backdonation.[225] This mechanism had originally been proposed for nitrogenase,[59] where the positive charge in sulfur-bound hydrogen species enhanced the pushing of electrons by the cofactor into the nitrogen molecule.

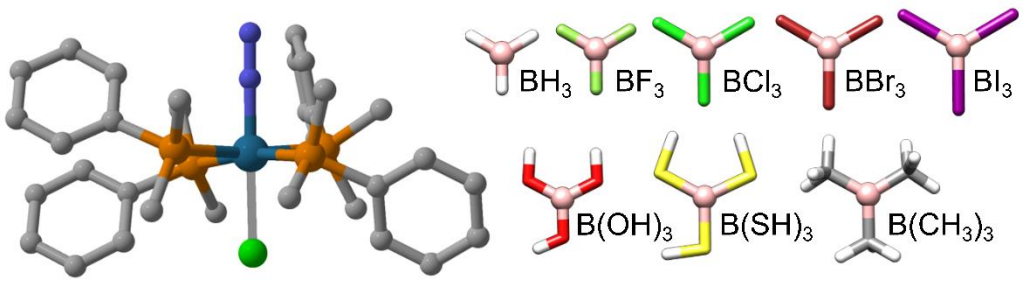

Figure 8.1. Molecular structures of the parent complex, trans-[Re^{I}Cl(N_2)(PMe_2Ph)$_4$], (left) and some of the Lewis acids tested in this work (right). The color code of the elements is rhenium, teal; nitrogen, blue; phosphorus, orange; carbon, grey; chloride, green; fluoride, light green; bromide, dark red; iodide, purple; oxygen, red; sulfur, yellow; hydrogen, white; carbon-bound hydrogen atoms are omitted for clarity.

In this work, we revisit the Re(I) complex synthesized by Chatt (Figure 8.1).[226, 227] It can form dinuclear, N_2-bridged complexes; adducts were obtained with group 4, 5 and 6 halides[210, 228, 229] and metalloporphyrins.[213] Herein, we set out to rationalize how the addition of a second molecular entity to the distal end of the N_2 molecule affects the dinitrogen bond strength. More specifically, the viability of less expensive, but ideally equally effective, borane Lewis acids is evaluated. Since Mo(0) and W(0) complexes with phosphine equatorial ligands have been shown to spontaneously bind two dinitrogen units and work as templates for further functionalization,[230, 231] or direct conversion of dinitrogen into ammonia,[232] we furthermore study the isoelectronic molybdenum and tungsten analogues of the Chatt complex.

8.2. Computational method

Density Functional Theory[79] calculations were performed with the ORCA 5[233-235] suite of programs. Geometry optimizations and numerical frequency calculations were performed with the functional combining the exchange energy approximation by Becke[236] and correlation by Perdew[237] (BP86) in combination with the balanced polarized triple-ζ basis set from the Ahlrichs family[238] (def2-TZVP) for all atoms. The resolution of the identity integral method,[239] with the appropriate auxiliary basis (def2/J), was used in order to optimize computational cost. Grimme's DFT-D4[240] was included to account for dispersion interactions. Solvent effects were considered using the conductor-like polarizable continuum model (CPCM)[241] for dichloromethane. Explicit solvent molecules are not expected to have a significant influence on the

covalent binding reported here and are therefore not included. Equally, counterions and other species commonly found in solution are not explicitly included.

A pincer ligand system by Schneider and coworkers has proven successful in dinitrogen activation using multiple strategies with different transition metal ions.[242-246] Redox potentials were calculated using the method described by Schneider and coworkers.[245] The potential is obtained from the difference between the oxidized and reduced forms Gibbs energies and the Nernst equation. It is anchored to the experimental value measured for the first (reversible) wave of *mer*-[ReCl(N_2)(PPhCPh=CPh)(PMe_2Ph)$_3$] (0.19 V vs SCE).[247] All the computational data have been uploaded (DOI: 10.19061/iochem-bd-4-56, link: https://doi.org/10.19061/iochem-bd-4-56) onto the ioChem-BD[248] platform (www.iochem-bd.org) to facilitate data exchange and dissemination, according to the FAIR[249] principles of OpenData sharing.

8.3. Results and discussion

While the chemical concept of an "acceptor of electrons" is rather intuitive, the quantitative determination of Lewis acidity is not a trivial chemical problem[250, 251] even though it is in principle rooted in thermodynamics.[252] Experimental attempts to devise a Lewis acidity scale have relied on measuring the change of a physical property, such as luminescence, NMR shifts or IR bands, when binding the same molecular entity to different Lewis acids (LAs).[253-257] Computational efforts have followed a similar approach by calculating the relative thermodynamic stability of binding the same electron donor, usually

the fluoride or the hydride anion, to a range of LAs. These are known as the fluoride ion affinity (FIA)[258, 259] and the hydride ion affinity (HIA)[260] and the accuracy of these calculations has improved over the years.[258, 261, 262] The fluoride ion is a good proxy of a nonpolarizable base and the hydride of a polarizable base, such as a transition metal complex.[263] However, the literature on the latter is limited with a focus on hydrocarbon-based LAs.[264-267]

One of the latest contributions to this field were FIA calculations by Greb and coworkers[268] who applied coupled cluster and its domain-based local pair natural orbital variant[269-271] to a series of LAs containing halide, carbon and oxygen-based groups with group 13-15 central atoms. Although the accuracy of such a high-level method is remarkable, we have used it here to benchmark a computationally less demanding Density Functional Theory (DFT) approach to predict the FIA for several boranes, see Figure 8.2. As expected, DFT with a generalized gradient functional does not achieve coupled cluster accuracy, but it is suitable to obtain an equally sensible Lewis acidity scale. We note that a higher accuracy of the electronic energies may be achieved with a hybrid functional, but since vibrational frequencies will be employed for further analyses, the choice fell on BP86 as the density functional.

We find a generally good qualitative agreement between the FIAs calculated with a simple BP86/def2-TZVP approach and those reported by Greb and coworkers, see Figure 8.2. There is a shift in the absolute FIA values predicted at the DFT level with respect to the DLPNO coupled cluster calculations, so that relative values should be analyzed instead. Two outliers are BH_3 and $B(N(C_6F_5)_2)_3$, which have maximum errors of 59 and -87 kJ mol^{-1}, respectively, corresponding to relative errors of less than 12%. Overall, we find the

correlation of sufficient quality to evaluate the influence of LAs in potential push-pull systems for dinitrogen activation. Since the Lewis acidity depends on the Lewis base used as a reference,[250, 251, 272, 273] we report calculated hydride ion affinities (HIA) for the same set of LAs.[265] As shown in Figure 8.2 (bottom), the results are qualitatively the same.

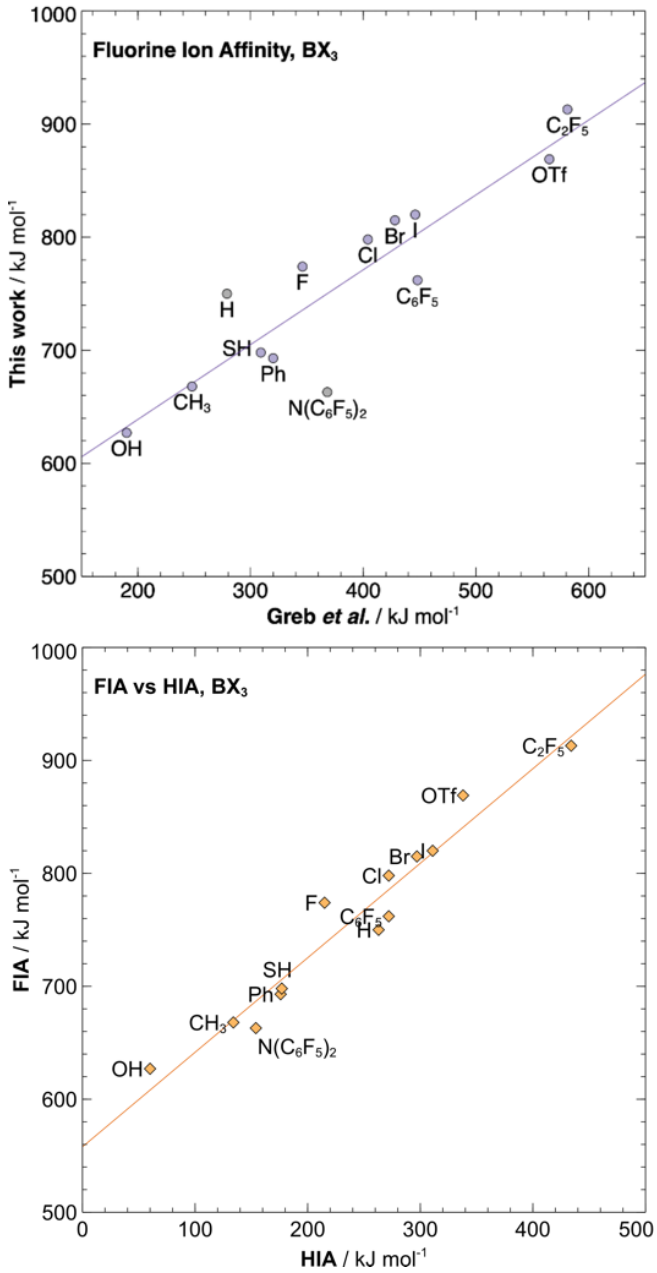

Figure 8.2. Top: Fluorine ion affinity calculation of BX_3 boranes, X=data label, using DFT (BP86/def2-TZVP) vs. the data from Greb and coworkers; linear fit parameters: y = 0.6621x + 506.47, R^2 = 0.8029 (blue line), excluding the outliers BH_3 and $B(N(C_6F_5)_2)_3$ results in linear fit with y = 0.6934x + 496.77, R^2 = 0.9234. Bottom: calculated FIAs vs. calculated HIAs at the same level of theory; linear fit parameters: y = 0.8368x + 557.9, R^2 = 0.9436 (orange line).

To understand how the LA affects the molecular orbitals (MOs) involving the dinitrogen unit, we analyzed the MO diagram for the bare Re-N_2 complex. The energy of the δ orbital, a relatively pure atomic orbital with rhenium $d_{x^2-y^2}$ character, is used as a reference point for frontier orbitals with significant rhenium or dinitrogen character.

Previously reported metal-dinitrogen MO diagrams for linear M–N-N–M and M–N-N complexes showed considerable splitting between σ-bonding and σ*-antibonding interactions while the remaining π interactions were found closer to the frontier orbital region.[57, 61, 243, 244, 274-279] In the present case, the σ-type orbitals[280] are HOMO-15 and LUMO+16. The δ reference orbital of the bare complex is found in the HOMO-2 position. The frontier occupied orbitals, HOMO and HOMO-1, have π-antibonding character for the N-N bond due to π-backbonding, which suggests that oxidation should increase the strength of this bond. Reduction of the complex would likely not weaken the N-N bond since the LUMO is found to comprise the aromatic π-systems of the phenyl rings in the phosphine ligands. The π*-π* orbitals are rather destabilized (3.62 eV above the HOMO).

To study the effect of LA binding towards a strategic influence of the molecular orbitals and thereby the degree of dinitrogen activation, the thermodynamic stability of Lewis Acid adducts of the rhenium complex and the analogous tungsten and molybdenum complexes with the same *d* configuration is evaluated. The formation of the LA adducts is generally thermodynamically favorable with stabilization energies between -15 and -241 kJ mol^{-1}. Exceptions to this are $B(OH)_3$ (ca +32 kJ mol^{-1}) and $B(N(C_6F_5)_2)_3$ (ca +220 kJ mol^{-1}) for all

three metal centers, and for Re^{I} additionally $B(CH_3)_3$ and $B(SH)_3$. We hypothesize that $B(OH)_3$ is not a strong enough electron acceptor to establish a proper bond with end-on-bound dinitrogen. For $B(N(C_6F_5)_2)_3$, the electrostatic repulsion between the bulky LA and the metal complexes may surpass any stabilization resulting from bonding, rendering the putative N-B bond unstable. The cases of $B(CH_3)_3$ and $B(SH)_3$ do not have a simple explanation, but we note that they are also at the lower end of the FIA scale.

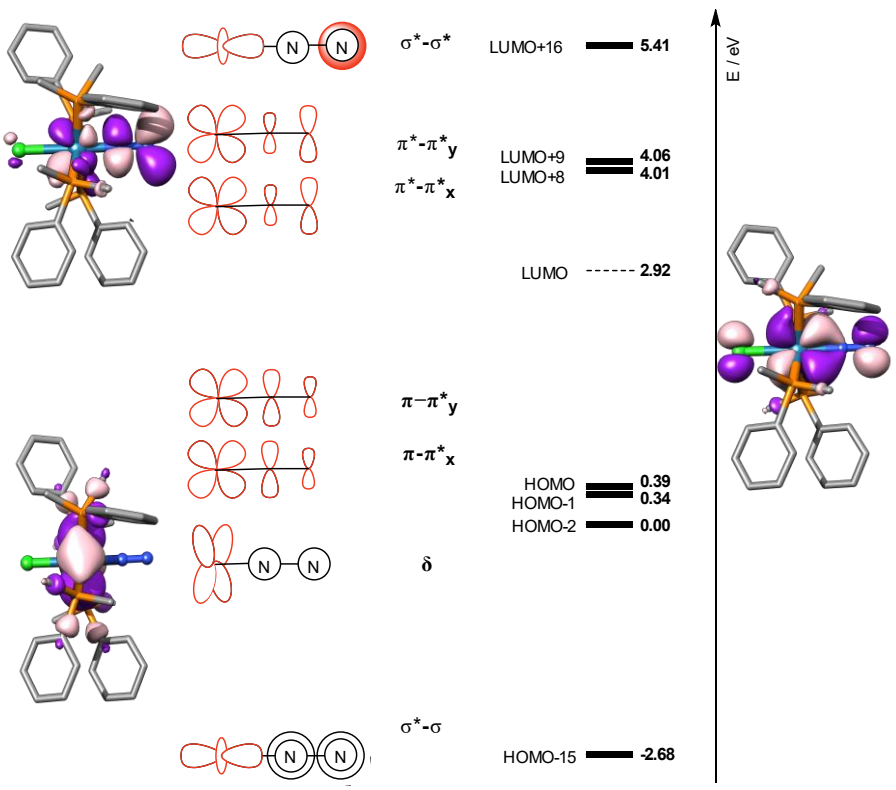

Figure 8.3. The MO diagram of the parent Re^{I} complex focusing on the orbitals with dominant metal and nitrogen character. Note that the orbital energies shown here are energies in eV relative to the δ reference orbital, HOMO-2.

The Lewis acids bind the end-on nitrogen ligand via the boron atom, forming a non-linear Re-N-N-LA subunit with N-N•••B angle varying from 132° (BF_3) to 172° ($B(CH_3)_3$). This geometrical arrangement is reminiscent of a dinuclear bent bridging motif[281-283] and may allow for an electrophilic attack of a substrate on the nascent lone-pair at the boron-bound nitrogen atom. The N-N bond distance in the bare Re-N-N complex is 1.154 Å, and it ranges from 1.158 Å [$B(CH_3)_3$] to 1.208 Å [$B(OTf)_3$] in the Re-N_2-LA adducts, suggesting some degree of bond weakening for all adducts. While the strength of a bond is often assessed by the bond length, it can be evaluated more quantitatively with other parameters such as bond orders or N-N stretching frequencies.[284] To compare the validity of these measures, N-N Mayer bond orders and $\upsilon_{N\text{-}N(stretch)}$ frequencies are plotted against the calculated FIA in Figure 8.4.

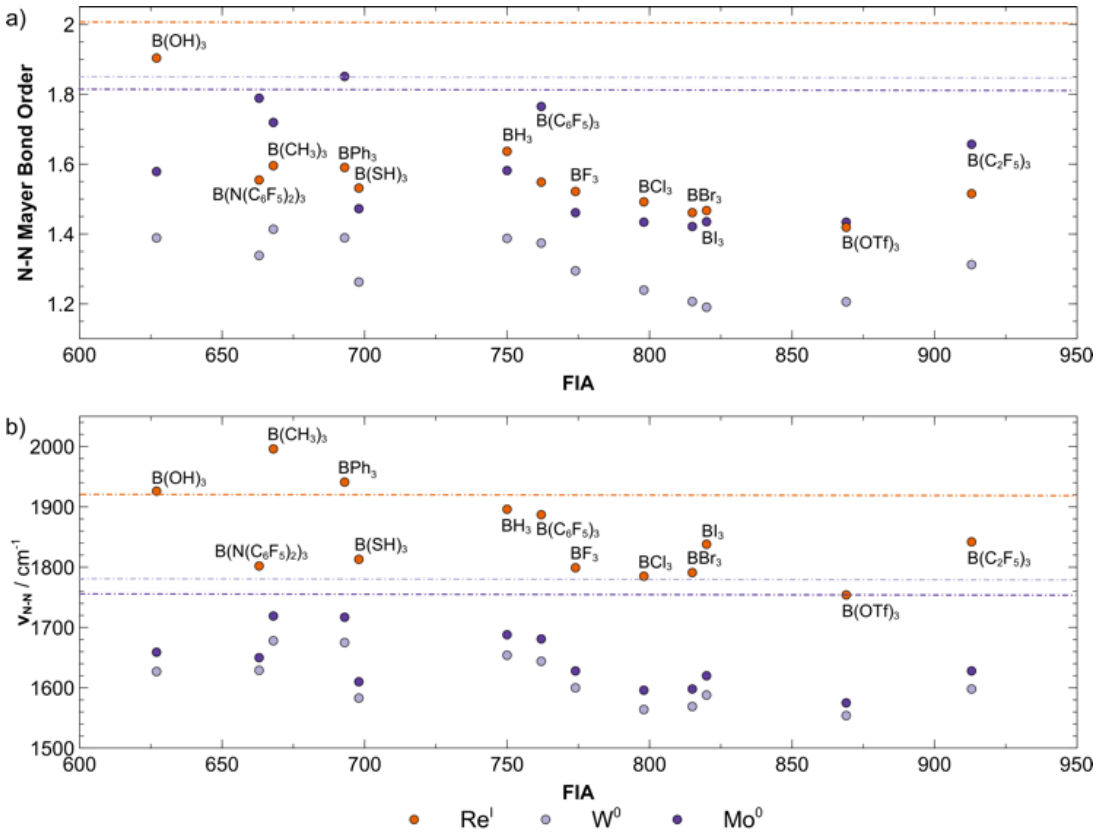

Figure 8.4. Computed a) N-N Mayer bond orders and b) N-N vibrational frequency vs. calculated FIA. The data points represent different metal ion-LA adducts: Re^{I} (orange), W^{0} (purple) and Mo^{0} (light purple). Dashed lines represent the values of the bare complexes.

Figure 8.4a shows that the N-N bond orders of the metal complex-LA adducts (dots) are lower than in the bare complexes (dashed line), indicative of a higher degree of N_2 activation. However, the values are rather scattered across the FIA scale and do not show a clear trend for the three metal elements studied so that Mayer bond orders should be interpreted with some caution. In contrast, the N_2 stretching frequencies shown in Figure 8.4b show a general decrease of $\upsilon_{N\text{-}N}$ with increasing FIA, albeit not perfectly linear, and a clear trend for the three

types of central metal. Deviations from linearity along the FIA scale may be due to steric effects: the relationships between $\upsilon_{N\text{-}N}$ and FIA for LAs with comparable steric hindrance, such as the $B(OH)_3/B(SH)_3$ and $BPh_3/B(C_6F_5)_3$ pairs, appear to be reasonable. The case of $B(C_2F_5)_3$, however, does not follow this trend. Its structure is very similar to that of the $B(OTf)_3$ adduct, so considering that a higher FIA was obtained in both our computational model and that of Greb and coworkers, a decrease in $\upsilon_{N\text{-}N}$ is expected. We will return to this result further below as this may be related to the molecular orbital diagram resulting from adduct formation (Figure 8.5).

We note that the decrease in $\upsilon_{N\text{-}N(stretch)}$ with increasing FIA is independent of the metal ion – the "pushing" of electrons into the N_2 bridge is consistent for all adducts and depends only on the acidity of the metal. This is an important finding as orthogonal effects can be independently tuned and exploited for the rational design of new molecules. Binding to the electron withdrawing Lewis acids can weaken the N-N bond from an obvious triple bond[284] in the bare Re^{I} complex with a N-N stretching mode at 1919 cm^{-1}, to 1754 cm^{-1} in the Re^{I}–$B(OTf)_3$ adduct or even to values as low as 1575 cm^{-1} for the analogous Mo^{0}-$B(OTf)_3$ complex. These stretching frequencies are consistent with the N-N double bond range (ca. 1300-1800 cm^{-1}), and are much lower than those reported, for instance, for the Re^{I}-N_2-metalloporphyrin complexes of iron and chromium (1803 and 1887 cm^{-1}, respectively).[213] We note that the predicted modes are expected to differ from experimental values due to the harmonic approximation and intrinsic DFT errors. The qualitative trend and the degree of activation, however, is expected to translate to experimental observations. Our findings are in general agreement with those of Szymczak and coworkers for an Fe^{0}

model of the nitrogenase enzyme,[222] although for a smaller range of Lewis acids. This result strongly supports the usefulness of LAs for electronic structure modulations and implies that a more detailed electronic structure analysis can shed light onto the activation mechanism in M-N_2-LA adducts.

Having shown that the formation of M-N_2-LA adducts affects the N-N bond strength, the findings will now be interpreted within an MO framework for the series of Re-N_2-LA adducts. $B(OH)_3$ is excluded from this analysis because no stable structure with a B-N bond was found.

In their nitrogenase model study, Szymczak and coworkers[222] rationalized the decrease in $\upsilon_{N\text{-}N}$ by comparing the admixture of $d_{xy}/d_{xz}/d_{yz}$-type atomic orbitals of the transition metal with π-MOs of the N_2-LA adduct and discussed the stabilization of the resulting MOs with respect to the MOs of the separate fragments. We did not find a significant variation of the rhenium atomic orbital coefficient in the π-frontier MOs (values ranging from 2.7% to 5.2%). We also found no meaningful correlation between the degree of admixture and the calculated FIAs or $\upsilon_{N\text{-}N}$ for the complexes studied here.

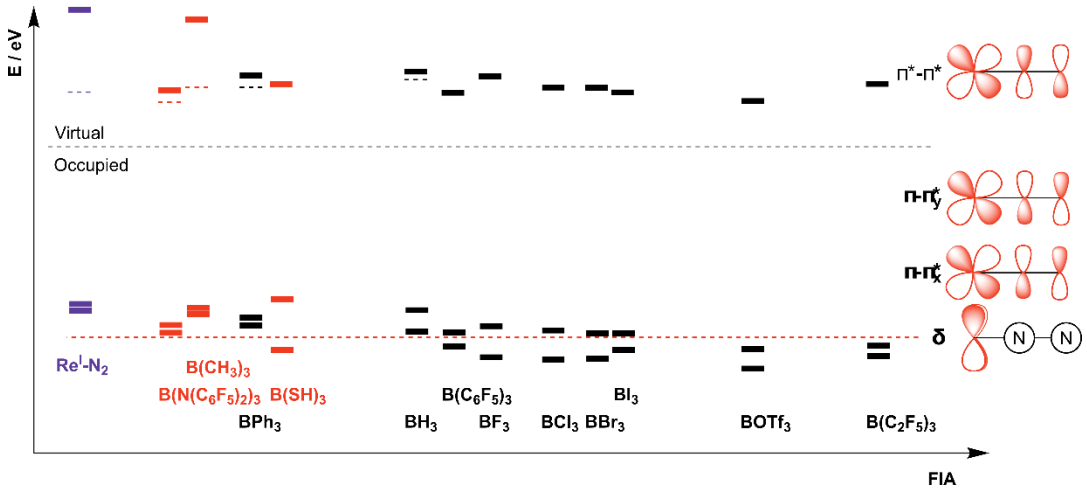

Figure 8.5. Molecular orbital energies of the occupied π-π and virtual π*-π* orbitals relative to the respective d orbital energies (orange dashed line) for all LA-N_2-rhenium(I) adducts. The bare complex is represented in purple and the Lewis acids with thermodynamically unfavorable binding in orange, except $B(OH)_3$ as no stable structure with a B-N bond was obtained. Orbitals that do not have considerable N character are not represented unless they correspond to the LUMO (dashed lines).*

We therefore devised an alternative approach for rationalizing the LA effect in an MO framework. As a suitable reference point for comparing orbital energies across all M-N_2-LA adducts, we chose the Re $d_{x^2-y^2}$ orbital (δ-MO) of all the adducts, since it can be readily identified, corresponds to an essentially pure Re atomic orbital and should thus not change its energy when adduct formation occurs. This approach is advantageous as it only requires a description of the full adduct and not of the separate fragments.

Figure 8.5 shows how the electron withdrawing capabilities of the LAs affect the frontier orbital energies in the adducts relative to the δ-MO. The relative energies of the π-π* orbitals generally decrease with increasing FIA, in a very similar trend to that observed in Figure 8.4 for the N-N stretching frequencies. Correlating the energy of the more stable π- π* orbital against $\upsilon_{N\text{-}N}$ shows a

linear relationship with a coefficient of determination R^2 close to 0.80. The mean absolute error is quite small, -0.09 eV. The elimination of the obvious outlier with the largest relative error of ca. 10%, the bulky $B(N(C_6F_5)_2)_3$, leads to an improvement in coefficient of determination to 0.96 and a much better correlation ($E_{\pi\text{-}\pi^*} = 0.0027\upsilon_{N\text{-}N} - 5.0436$ eV). A very similar trend is observed if instead of the energy of the lower π-π*, the center of gravity of the two π-π* orbitals is considered (albeit with a smaller R^2 value of 0.80).

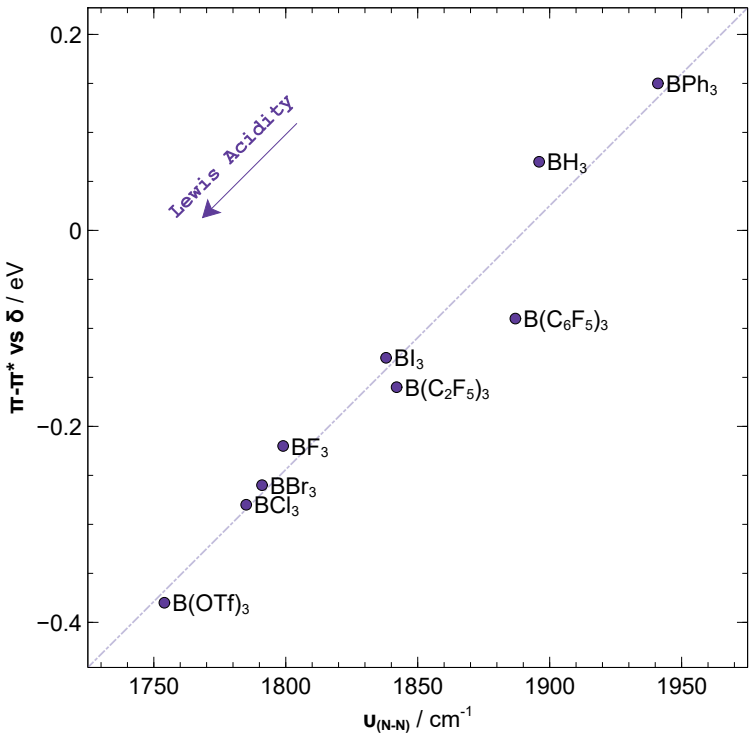

Figure 8.6. Relative energy of the lower π-π orbital with respect to the metal δ orbital, for each Re^{I}-N_2-LA adduct, plotted against the respective N-N stretching frequency. Linear fit parameters: y = 0.0027x - 5.0912, R^2 = 0.9491.*

These results show that the weakening of the N-N bond by a LA, usually referred to as a "pulling" effect, can be interpreted within the MO scheme as a stabilization of the π-π* orbitals upon formation of the adduct. In contrast, the π*-π* orbitals are essentially unaffected by LA binding.

It is also noteworthy that, in contrast to what had been observed upon plotting $\upsilon_{N\text{-}N}$ vs FIA (Figure 8.4), the expected relative positions of $B(OTf)_3$ and $B(C_2F_5)_3$ are obtained in Figure 8.5 and Figure 8.6. This may be interpreted as a more favorable overlap between the π orbitals of dinitrogen with those of $B(OTf)_3$ compared to those of $B(C_2F_5)_3$ that outweighs the apparently weaker electron withdrawing capability of $B(OTf)_3$.

Although the π*-π* orbital energy is essentially the same in all adducts, see Figure 8.5, an important observation is that the stronger Lewis acids shift the π*-π* orbital into the LUMO position. This may allow its population via electrochemical reduction, which would decrease the strength of both the metal-nitrogen and the nitrogen-nitrogen π-bonds. Even though it was not rationalized within a molecular orbital framework, the facilitation of redox catalysis via binding to an electron acceptor has already been achieved in the context of dinitrogen binding and functionalization.[285] Such a dual effect could contribute to the desired result of forming bonds between nitrogen and a new organic unit or to releasing the product from the metal.

The nature and energy of the required electrochemical steps to further enhance N_2 activation was evaluated by calculating the redox potentials and anchoring them to an experimentally measured reversible redox peak in a Re^I analogue.[245] The processes studied here are shown in Scheme 8.1 with redox potentials *vs*.

SHE for the parent complex. A constant of 0.244 V was added to the potentials to move from the SCE (experimental result) to SHE scale.

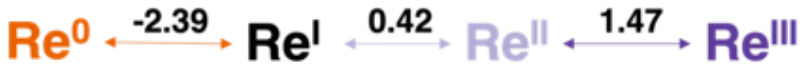

Scheme 8.1. Computed reduction potentials between the different rhenium species (bare complex) vs SHE (V).

The metal ion was confirmed to undergo the oxidation processes, as the appropriate spin density changes are solely accumulated on the rhenium atom. The reduction, however, is shared between the phosphine aromatic systems and the rhenium ion (weak LAs) or between the nitrogen bridge and the rhenium ion (strong LAs), as expected from the nature of the corresponding LUMOs.

While the expected spin states for the $Re^{0\text{-}II}$ species are clear, there are two plausible spin states for Re^{III}. Calculations show that the singlet state is energetically preferred over the triplet state for the bare complex (-10 kJ mol^{-1}) and LA adducts (BPh_3: -1 kJ mol^{-1}; $B(C_2F_5)_3$: -4 kJ mol^{-1}; others: -10 to -14 kJ mol^{-1}). Considering these small energy differences and expected spin-orbit coupling effects suggests that the redox potentials predicted here will likely differ from those that would be measured experimentally. However, even with this uncertainty in mind, the calculated redox potentials reported in Table 8.1 seem attainable and are in agreement with previous reports for similar Re-N_2 complexes.[245]

The results completely corroborate the expectations from the molecular orbital analysis shown in Figure 8.5. For the LA adducts with a π*-π* orbital as the LUMO, ($B(C_2F_5)_3$, BCl_3 and $B(OTf)_3$), reduction to Re^0 decreases the N-N stretching frequency by ca. 300 cm^{-1}. This is not observed for the bare complex or the ones forming adducts with BPh_3/BH_3, because the π*-π* orbitals are not in the frontier region (LUMO+8). The weakening of both the Re-N and N-N bonds upon reduction is also corroborated by the increased bond lengths of the reduced complexes relative to the neutral compounds. In the case of the $Re-N_2-B(OTf)_3$ adduct, the increase is similar for the Re-N (0.078 Å) and the N-N (0.050 Å) bonds.

Single and double oxidation events lead to an increase in υ_{N-N}, as the antibonding π-π* HOMO orbital is depopulated. Not only does the binding to LAs allow for a reduction process productive for nitrogen bond weakening, but it also shifts the redox level (ca. +0.8 V) towards better attainable potentials, making this reduction easier while maintaining the redox span. The latter shift had also been reported for the Fe^0 nitrogenase-like complex.[222]

Table 8.1. N-N stretching frequencies (cm^{-1}) and reduction potentials (V vs. SHE) for the different rhenium oxidation states and adducts. The data for Re^{III} species is based on singlet spin states.

	LA	Re^{0}	Re^{I}	Re^{II}	Re^{III}
$\upsilon_{(N-N)}$ / cm^{-1}	-	1897	1919	1993	2074
	BPh_3	1907	1941	1978	2038
	BH_3	1847	1896	2009	2112
	$B(C_2F_5)_3$	1514	1842	1911	1985
	BCl_3	1514	1785	1860	1975
	$B(OTf)_3$	1467	1753	1837	1884
Pot. vs SHE / V	-	-2.39		0.42	1.47
	BPh_3	-2.31		0.74	1.78
	BH_3	-2.32		0.72	1.64
	$B(C_2F_5)_3$	-1.97		1.14	2.24
	BCl_3	-1.94		1.20	2.07
	$B(OTf)_3$	-1.73		1.38	2.27

As a final tuning opportunity in the complex, the ligand in the *trans* position to the nitrogen bridge[286] was modified to study a putative enhancement of the "pushing" effect of the metal, possibly leading to cooperative pushing and pulling. The "push" had previously been rationalized as the donation from filled metal *d* orbitals to N_2 π^* orbitals upon formation of the M-N_2-LA adducts.[222] We thus tested the substitution of the chloride ligand in the initial rhenium complex with the other halogens.

An increasing halogen electronegativity decreases the N-N stretching frequency in the three test cases shown in Figure 8.7. This suggests that removing electron density from the metal ion improves N-N activation, contrary to what had previously been reported for complexes with *trans* boron-metal bonds and is expected for a "push"-like effect. The effect is small for Cl, Br and I (ca. 5-10 cm^{-1} per halide substitution step), but when chloride is substituted by fluoride, a decrease comparable to the pulling effect of the Lewis acids of up to 44 cm^{-1} is seen. We note that binding of a LA and substitution of a *trans*-ligand are two independent processes, as the same effect is observed for three LAs at different points of the FIA spectrum and can thus be exploited cooperatively.

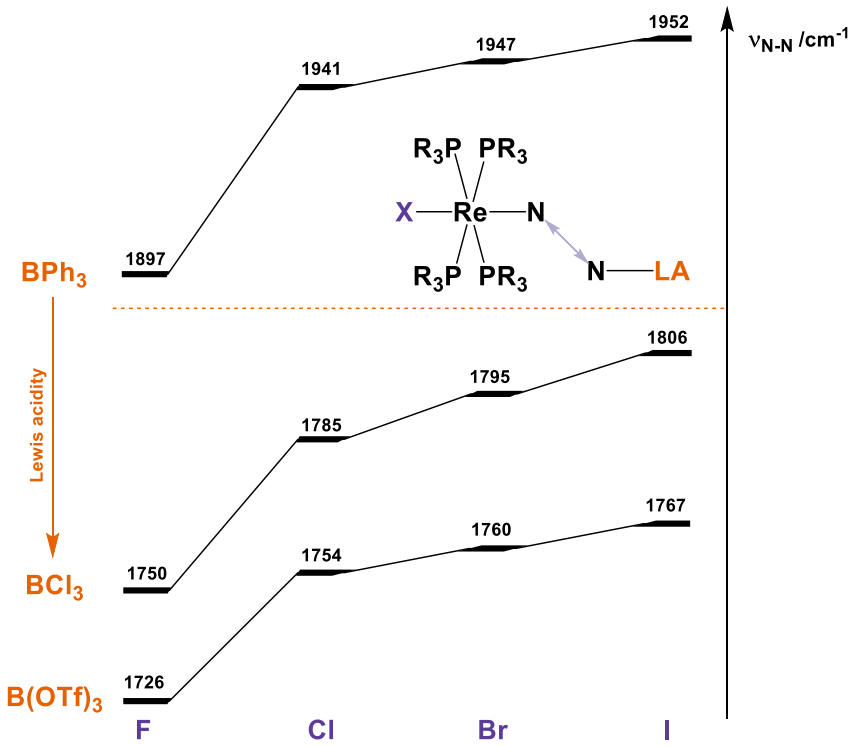

Figure 8.7. Effect of halogen substitution in the position trans to the dinitrogen bridge on different Lewis acid-bound Re^{I} complexes.

This finding was rationalized with a molecular orbital diagram in which metal and halogen atoms are varied, see Figure 8.8. Taking the chloride complexes as a starting point (purple lines), it is shown how the π and σ orbitals along the halogen-metal-nitrogen axis are affected (i) by adduct formation with the strongest LA $B(OTf)_3$ (black lines), and (ii) additional substitution of the chloride ligand for the more electronegative fluoride (orange lines). For all three metals, the same π-stabilization is observed upon LA binding: the black energy levels of the LA adduct are lower in energy than the purple lines of the parent complexes.

Comparing the metal series from the more acidic Re^{I} to the less acidic Mo^{0}, the relative energy of the π frontier orbitals generally decreases. This is expected as the latter should be able to push more electron density into the N_2 antibonding orbitals and is in perfect agreement with the $\upsilon_{N\text{-}N}$ relationships established in Figure 8.5. We note that for the tungsten and molybdenum complexes, the π*-π* stabilization observed upon LA binding is like that discussed above for the rhenium complex. The π*-π* levels lower from LUMO+9 to LUMO+8, but the effect is not strong enough to create LUMOs of predominant N π* character and thus allow for productive reduction processes.

Importantly, upon substitution of the *trans*-ligand in the adducts, the π frontier orbitals are destabilized. This is unexpected, as the F-M-N_2-LA adducts have a smaller $\upsilon_{N\text{-}N}$ and previous analyses of the π-system showed that a decrease in $\upsilon_{N\text{-}N}$ seems to be directly connected to a π-frontier orbital stabilization.[222] Inspection of the σ bonds along the X-M-N_2 axis reveals that there is a significant stabilization of this orbital in the *trans*-fluorine complex, implying a donation of electron density from dinitrogen to the metal along a σ-path enhanced by increasing electronegativity of the *trans*-halogen. The possibility of electron density donation via a σ-path had been discussed by Ruddy and coworkers in 2018:[223] however, to the best of our knowledge, this is the first time it is identified in a series of transition metal dinitrogen complexes.

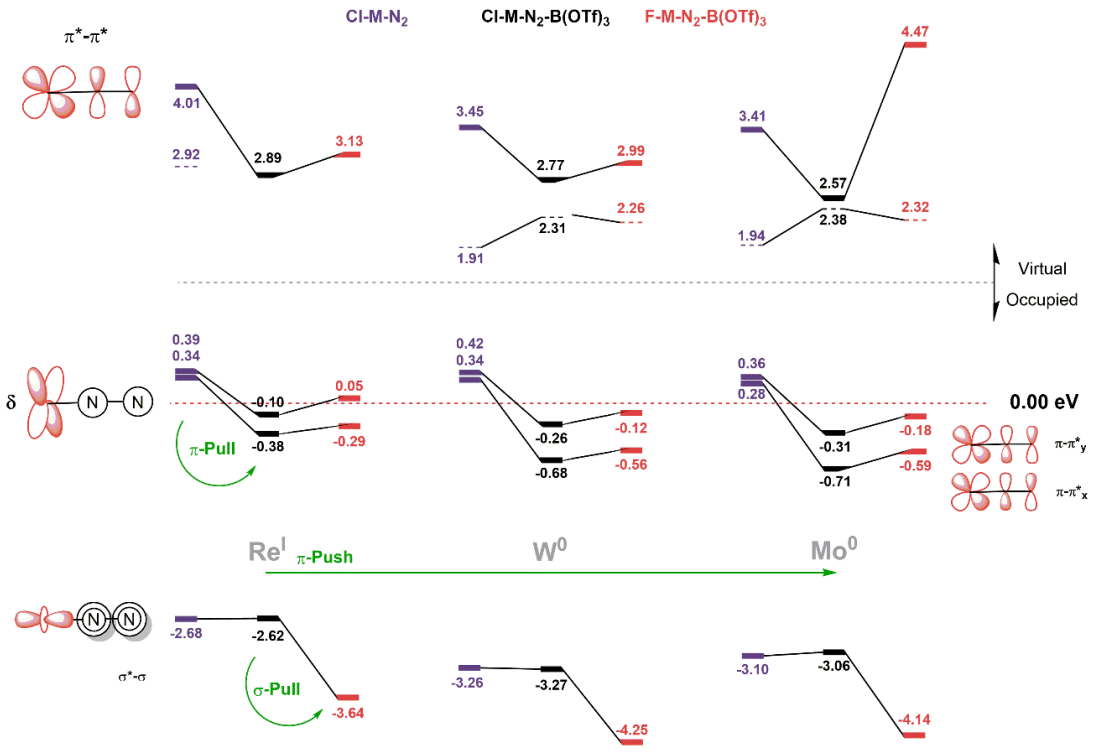

Figure 8.8. Frontier orbital diagram for the bare Re^{I}, Wo and Mo^{0} complexes (purple) and respective Push/Pull Lewis acid analogues with chloride (black) and fluoride (orange) ligands in the trans position relative to the nitrogen.

The σ-drain of the electron density over both the metal and the dinitrogen bridge is confirmed by a correlation between the decrease in σ orbital energy and the N-N stretching frequency shown in Figure 8.9. These two parameters correlate with a determination coefficient of ca. 0.99, which further supports that the weakening of the dinitrogen bond is indeed caused by a weakening of the σ interactions due to the electronegativity of the halogen. The σ effect is stronger than the influence of the metal and compensates for the diminished π-pushing of the metal *d* orbitals. However, the synthetic viability of a fluoride

substituent cannot be assessed here; other choices of ligand positioned *trans* to the dinitrogen unit and able to pull electron density via the σ-channel may have a smaller effect.

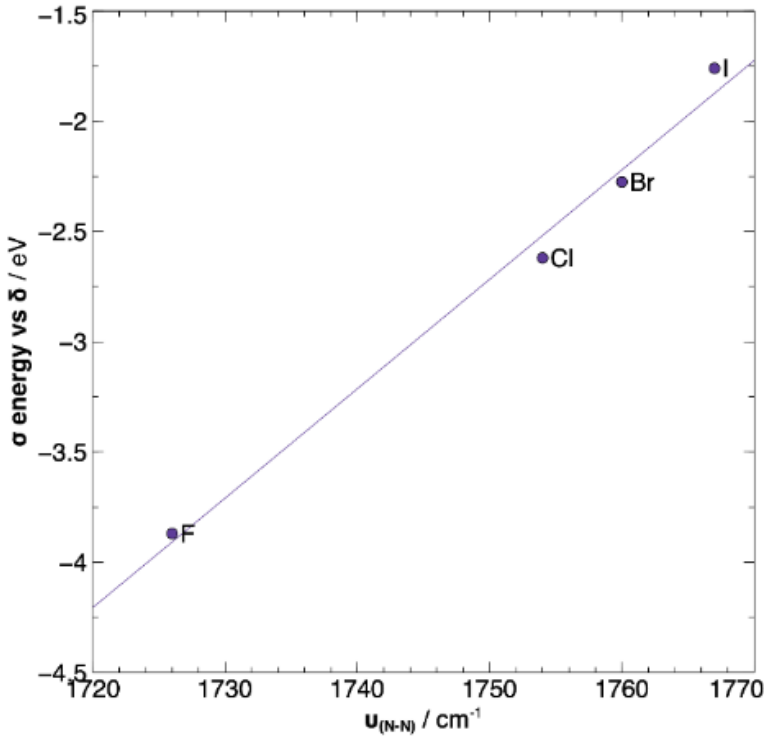

Figure 8.9. Relative energy of the halogen-metal-N2 σ orbital with respect to the metal δ orbital, for each X-Re^{I}-N$_2$-B(OTf)$_3$ adduct, plotted against the respective N-N stretching frequency. Linear fit parameters: y = 0.0496x - 89.573, R^2 = 0.9886.

Herein, we studied the cooperative "push-pull" effect of Lewis acid binding to dinitrogen bound in molybdenum, tungsten, and rhenium complexes with a d^6 configuration. Stronger Lewis acids weaken the dinitrogen bond more strongly as monitored by the N-N stretching frequencies, although steric hindrance and electronic effects cannot be fully disentangled. The "push-pull" effect was

rationalized with an electronic structure analysis: occupied molecular orbitals with π antibonding interactions between the two nitrogen atoms are more strongly stabilized for stronger Lewis acids. The choice of Lewis acid was furthermore found to determine the orbital ordering in the rhenium complexes. The π*-π* metal-N_2 orbital can be moved into the LUMO position, implying electrochemical bond activation in a single reduction event.

Chapter 9

Conclusions

9. CONCLUSIONS

Overall, we have shown how Density Functional Theory, born in the 1920s with a revival in the 1960s,[287] survived and thrived for decades, remaining of the utmost relevant for the description of ever more complicate chemical systems for decades. The work presented here is meant to highlight its capabilities in the study of transition-metal complexes, which are particularly tricky to analyze due to their open-shell electronic configurations. The Chemistry-related conclusions are presented divided by chapters, below:

Chapter 4 (Spectroscopy to structure in oxo bridged iron dinuclear compounds):

- We have shown how vibrational frequencies depend on geometrical constraints and the origin of such correlations;
- This knowledge allowed us to develop tools that predict structural and magnetic parameters with decent accuracy, from recorded vibrational spectra;

Chapter 5 (Electronic properties of N-confused Metalloporphyrins):

- DFT methods were proven capable of describing the electronic structure of extremely delocalized systems;
- N-confusion in the porphyrin ligand disrupts the symmetry of the molecular orbitals in the frontier region and, thus, alters the optical properties of these complexes, including the Soret band;
- The spin of metallo-N-confused-porphyrinates seems to depend on the total number of unpaired electrons, irrespectively of their location – only a few metal oxidation states are accessible;

Chapter 6 (Ni-halide C-H activation):

- Despite its many capabilities, DFT can not be considered a black-box method as the potential energy surface that one explores from a specific starting structure may not lead to useful conclusions and while there are ways of accessing other PES minima, there is always a degree of uncertainty as to whether the real one was found;

Chapter 7 (High-valent Iron species characterization):

- High-valent iron-oxo species can be identified via TD-DFT methodologies with relatively low computational cost;

Chapter 8 (Cooperative effects between transition metals and Lewis acids for the activation of dinitrogen):

- The "push-pull" cooperative effect of Lewis acids and transition-metals has been rationalized via a Molecular Orbital viewpoint;
- These strategies show great promise in the improvement of TMetCs reactivity towards though reactions.

While I believe this document properly exhibits the Physical Chemistry, Inorganic Chemistry and reading/writing qualifications I have honed during these four years, it lacks in showing many other skills. I should therefore mention that I was working in a healthy competitive environment that fostered good work ethic, cooperation among individuals and promoted pushing boundaries and growth. I also had the opportunity to join the Scientific Communication Committee of the institute, which gave me extensive managerial skills and helped me better communicate the science developed within the institute to the general public, including students.

REFERENCES

1. Gomollón-Bel, F., IUPAC Top Ten Emerging Technologies in Chemistry 2022. *Discover the innovations that will transform energy, health, and materials science, to tackle the most urgent societal challenges and catalyse sustainable development.* **2022,** *44* (4), 4-13.
2. Gomollón-Bel, F., IUPAC Top Ten Emerging Technologies in Chemistry 2021. *Breakthroughs for a circular, climate-neutral future* **2021,** *43* (4), 13-20.
3. Yang, B.; Ding, W.; Zhang, H.; Zhang, S., Recent progress in electrochemical synthesis of ammonia from nitrogen: strategies to improve the catalytic activity and selectivity. *Energy & Environmental Science* **2021,** *14* (2), 672-687.
4. Dalle, K. E.; Warnan, J.; Leung, J. J.; Reuillard, B.; Karmel, I. S.; Reisner, E., Electro- and Solar-Driven Fuel Synthesis with First Row Transition Metal Complexes. *Chemical Reviews* **2019,** *119* (4), 2752-2875.
5. Norvaiša, K.; Kielmann, M.; Senge, M. O., Porphyrins as Colorimetric and Photometric Biosensors in Modern Bioanalytical Systems. *ChemBioChem* **2020,** *21* (13), 1793-1807.
6. Safaei, M.; Foroughi, M. M.; Ebrahimpoor, N.; Jahani, S.; Omidi, A.; Khatami, M., A review on metal-organic frameworks: Synthesis and applications. *TrAC Trends in Analytical Chemistry* **2019,** *118*, 401-425.
7. Dodd, M. S.; Papineau, D.; Grenne, T.; Slack, J. F.; Rittner, M.; Pirajno, F.; O'Neil, J.; Little, C. T. S., Evidence for early life in Earth's oldest hydrothermal vent precipitates. *Nature* **2017,** *543* (7643), 60-64.
8. Groves, J. T., Using push to get pull. *Nature Chemistry* **2014,** *6* (2), 89-91.
9. Costas, M.; Harvey, J. N., Discussion of an open problem. *Nature Chemistry* **2013,** *5* (1), 7-9.
10. and, P. E. M. S.; Blomberg, M. R. A., DENSITY FUNCTIONAL THEORY OF BIOLOGICALLY RELEVANT METAL CENTERS. *Annual Review of Physical Chemistry* **1999,** *50* (1), 221-249.
11. Banerjee, R.; Jones, J. C.; Lipscomb, J. D., Soluble Methane Monooxygenase. *Annu Rev Biochem* **2019,** *88*, 409-431.
12. Ravi, M.; Ranocchiari, M.; van Bokhoven, J. A., The Direct Catalytic Oxidation of Methane to Methanol-A Critical Assessment. *Angewandte Chemie International Edition* **2017,** *56* (52), 16464-16483.
13. Jasniewski, A. J.; Que, L., Jr., Dioxygen Activation by Nonheme Diiron Enzymes: Diverse Dioxygen Adducts, High-Valent Intermediates, and Related Model Complexes. *Chem Rev* **2018,** *118* (5), 2554-2592.
14. Que, L., Jr.; Tolman, W. B., Bis(mu-oxo)dimetal "diamond" cores in copper and iron complexes relevant to biocatalysis. *Angewandte Chemie International Edition* **2002,** *41* (7), 1114-37.

15. Banerjee, S.; Draksharapu, A.; Crossland, P. M.; Fan, R.; Guo, Y.; Swart, M.; Que, L., Jr., Sc(3+)-Promoted O-O Bond Cleavage of a (mu-1,2-Peroxo)diiron(III) Species Formed from an Iron(II) Precursor and O2 to Generate a Complex with an Fe(IV)2(mu-O)2 Core. *J Am Chem Soc* **2020,** *142* (9), 4285-4297.
16. Lee, S. K.; Nesheim, J. C.; Lipscomb, J. D., Transient intermediates of the methane monooxygenase catalytic cycle. *Journal of Biological Chemistry* **1993,** *268* (29), 21569-21577.
17. Liu, K. E.; Valentine, A. M.; Wang, D.; Huynh, B. H.; Edmondson, D. E.; Salifoglou, A.; Lippard, S. J., Kinetic and spectroscopic characterization of intermediates and component interactions in reactions of methane monooxygenase from Methylococcus capsulatus (Bath). *Journal of the American Chemical Society* **1995,** *117* (41), 10174-10185.
18. Banerjee, R.; Proshlyakov, Y.; Lipscomb, J. D.; Proshlyakov, D. A., Structure of the key species in the enzymatic oxidation of methane to methanol. *Nature* **2015,** *518* (7539), 431-434.
19. Trehoux, A.; Mahy, J.-P.; Avenier, F., A growing family of O2 activating dinuclear iron enzymes with key catalytic diiron(III)-peroxo intermediates: Biological systems and chemical models. *Coordination Chemistry Reviews* **2016,** *322*, 142-158.
20. Tshuva, E. Y.; Lippard, S. J., Synthetic Models for Non-Heme Carboxylate-Bridged Diiron Metalloproteins: Strategies and Tactics. *Chemical Reviews* **2004,** *104* (2), 987-1012.
21. Dantignana, V.; Company, A.; Costas, M., Catalytic Oxidation of Primary C–H Bonds in Alkanes with Bioinspired Catalysts. *CHIMIA* **2020,** *74* (6), 470.
22. Castillo, C. E.; Gamba, I.; Vicens, L.; Clémancey, M.; Latour, J.-M.; Costas, M.; Basallote, M. G., Spin State Tunes Oxygen Atom Transfer towards FeIVO Formation in FeII Complexes. *Chemistry – A European Journal* **2021,** *27* (15), 4946-4954.
23. Dantignana, V.; Pérez-Segura, M. C.; Besalú-Sala, P.; Delgado-Pinar, E.; Martínez-Camarena, Á.; Serrano-Plana, J.; Álvarez-Núñez, A.; Castillo, C. E.; García-España, E.; Luis, J. M.; Basallote, M. G.; Costas, M.; Company, A., Characterization of a Ferryl Flip in Electronically Tuned Nonheme Complexes. Consequences in Hydrogen Atom Transfer Reactivity. *Angewandte Chemie International Edition* **2023,** *62* (2), e202211361.
24. Sánchez-Eguía, B. N.; Serrano-Plana, J.; Company, A.; Costas, M., Catalytic O2 activation with synthetic models of α-ketoglutarate dependent oxygenases. *Chemical Communications* **2020,** *56* (92), 14369-14372.
25. Kasper, J. B.; Saisaha, P.; de Roo, M.; Groen, M. J.; Vicens, L.; Borrell, M.; de Boer, J. W.; Hage, R.; Costas, M.; Browne, W. R., A Common Active Intermediate in the Oxidation of Alkenes, Alcohols and Alkanes with H2O2 and a Mn(II)/Pyridin-2-Carboxylato Catalyst. *ChemCatChem* **2023,** *15* (1), e202201072.

26. Besalú-Sala, P.; Magallón, C.; Costas, M.; Company, A.; Luis, J. M., Mechanistic Insights into the ortho-Defluorination-Hydroxylation of 2-Halophenolates Promoted by a Bis(μ-oxo)dicopper(III) Complex. *Inorganic Chemistry* **2020,** *59* (23), 17018-17027.
27. Chu, M.; Planas, O.; Company, A.; Ribas, X.; Hamilton, A.; Whiteoak, C. J., Unravelling the mechanism of cobalt-catalysed remote C–H nitration of 8-aminoquinolinamides and expansion of substrate scope towards 1-naphthylpicolinamide. *Chemical Science* **2020,** *11* (2), 534-542.
28. Orio, M.; Pantazis, D. A.; Neese, F., Density functional theory. *Photosynthesis Research* **2009,** *102* (2), 443-453.
29. Neese, F., Prediction of molecular properties and molecular spectroscopy with density functional theory: From fundamental theory to exchange-coupling. *Coordination Chemistry Reviews* **2009,** *253* (5), 526-563.
30. Murray, C. W.; Laming, G. J.; Handy, N. C.; Amos, R. D., Kohn—Sham bond lengths and frequencies calculated with accurate quadrature and large basis sets. *Chemical Physics Letters* **1992,** *199* (6), 551-556.
31. Han, W.-G.; Liu, T.; Lovell, T.; Noodleman, L., DFT calculations of 57Fe Mössbauer isomer shifts and quadrupole splittings for iron complexes in polar dielectric media: Applications to methane monooxygenase and ribonucleotide reductase. *Journal of Computational Chemistry* **2006,** *27* (12), 1292-1306.
32. Cramer, C. J.; Truhlar, D. G., Density functional theory for transition metals and transition metal chemistry. *Physical Chemistry Chemical Physics* **2009,** *11* (46), 10757-10816.
33. Kim, S.; Kim, J.; Zhong, H.; Panetti, G. B.; Chirik, P. J., Catalytic N–H Bond Formation Promoted by a Ruthenium Hydride Complex Bearing a Redox-Active Pyrimidine-Imine Ligand. *Journal of the American Chemical Society* **2022,** *144* (45), 20661-20671.
34. Carvalho, O. Q.; Marks, R.; Nguyen, H. K. K.; Vitale-Sullivan, M. E.; Martinez, S. C.; Árnadóttir, L.; Stoerzinger, K. A., Role of Electronic Structure on Nitrate Reduction to Ammonium: A Periodic Journey. *Journal of the American Chemical Society* **2022,** *144* (32), 14809-14818.
35. Merakeb, L.; Bennaamane, S.; De Freitas, J.; Clot, E.; Mézailles, N.; Robert, M., Molecular Electrochemical Reductive Splitting of Dinitrogen with a Molybdenum Complex**. *Angewandte Chemie International Edition* **2022,** *61* (40), e202209899.
36. Fritz, M.; Rupp, S.; Kiene, C. I.; Kisan, S.; Telser, J.; Würtele, C.; Krewald, V.; Schneider, S., Photoelectrochemical Conversion of Dinitrogen to Benzonitrile: Selectivity Control by Electrophile- versus Proton-Coupled Electron Transfer. *Angewandte Chemie International Edition* **2022,** *61* (35), e202205922.
37. Souilah, C.; Jannuzzi, S. A. V.; Demirbas, D.; Ivlev, S.; Swart, M.; DeBeer, S.; Casitas, A., Synthesis of FeIII and FeIV Cyanide Complexes Using Hypervalent Iodine Reagents as Cyano-Transfer One-Electron Oxidants. *Angewandte Chemie International Edition* **2022,** *61* (22), e202201699.

38. Kass, D.; Corona, T.; Warm, K.; Braun-Cula, B.; Kuhlmann, U.; Bill, E.; Mebs, S.; Swart, M.; Dau, H.; Haumann, M.; Hildebrandt, P.; Ray, K., Stoichiometric Formation of an Oxoiron(IV) Complex by a Soluble Methane Monooxygenase Type Activation of O2 at an Iron(II)-Cyclam Center. *Journal of the American Chemical Society* **2020,** *142* (13), 5924-5928.
39. Padamati, S. K.; Angelone, D.; Draksharapu, A.; Primi, G.; Martin, D. J.; Tromp, M.; Swart, M.; Browne, W. R., Transient Formation and Reactivity of a High-Valent Nickel(IV) Oxido Complex. *Journal of the American Chemical Society* **2017,** *139* (25), 8718-8724.
40. Brinkmeier, A.; Dalle, K. E.; D'Amore, L.; Schulz, R. A.; Dechert, S.; Demeshko, S.; Swart, M.; Meyer, F., Modulation of a μ-1,2-Peroxo Dicopper(II) Intermediate by Strong Interaction with Alkali Metal Ions. *Journal of the American Chemical Society* **2021,** *143* (42), 17751-17760.
41. Kozuch, S.; Shaik, S., How to Conceptualize Catalytic Cycles? The Energetic Span Model. *Accounts of Chemical Research* **2011,** *44* (2), 101-110.
42. Huynh, M. H. V.; Meyer, T. J., Proton-Coupled Electron Transfer. *Chem. Rev.* **2007,** *107* (11), 5004-5064.
43. Warren, J. J.; Tronic, T. A.; Mayer, J. M., Thermochemistry of Proton-Coupled Electron Transfer Reagents and its Implications. *Chemical Reviews* **2010,** *110* (12), 6961-7001.
44. Mayer, J. M., Understanding Hydrogen Atom Transfer: From Bond Strengths to Marcus Theory. *Accounts of Chemical Research* **2011,** *44* (1), 36-46.
45. Roth, J. P.; Yoder, J. C.; Won, T.-J.; Mayer, J. M., Application of the Marcus Cross Relation to Hydrogen Atom Transfer Reactions. *Science* **2001,** *294* (5551), 2524-2526.
46. D'Amore, L.; Belpassi, L.; Klein, J. E. M. N.; Swart, M., Spin-resolved charge displacement analysis as an intuitive tool for the evaluation of cPCET and HAT scenarios. *Chemical Communications* **2020,** *56* (81), 12146-12149.
47. Klein, J. E. M. N.; Knizia, G., cPCET versus HAT: A Direct Theoretical Method for Distinguishing X–H Bond-Activation Mechanisms. *Angewandte Chemie International Edition* **2018,** *57* (37), 11913-11917.
48. Price, J. C.; Barr, E. W.; Glass, T. E.; Krebs, C.; Bollinger, J. M., Evidence for Hydrogen Abstraction from C1 of Taurine by the High-Spin Fe(IV) Intermediate Detected during Oxygen Activation by Taurine:α-Ketoglutarate Dioxygenase (TauD). *Journal of the American Chemical Society* **2003,** *125* (43), 13008-13009.
49. Knapp, M. J.; Rickert, K.; Klinman, J. P., Temperature-Dependent Isotope Effects in Soybean Lipoxygenase-1: Correlating Hydrogen Tunneling with Protein Dynamics. *Journal of the American Chemical Society* **2002,** *124* (15), 3865-3874.
50. Goetz, M. K.; Anderson, J. S., Experimental Evidence for pKa-Driven Asynchronicity in C–H Activation by a Terminal Co(III)–Oxo Complex. *Journal of the American Chemical Society* **2019,** *141* (9), 4051-4062.

51. Amtawong, J.; Skjelstad, B. B.; Balcells, D.; Tilley, T. D., Concerted Proton–Electron Transfer Reactivity at a Multimetallic Co4O4 Cubane Cluster. *Inorganic Chemistry* **2020,** *59* (20), 15553-15560.
52. Mandal, M.; Elwell, C. E.; Bouchey, C. J.; Zerk, T. J.; Tolman, W. B.; Cramer, C. J., Mechanisms for Hydrogen-Atom Abstraction by Mononuclear Copper(III) Cores: Hydrogen-Atom Transfer or Concerted Proton-Coupled Electron Transfer? *Journal of the American Chemical Society* **2019,** *141* (43), 17236-17244.
53. Chatt, J.; Chatt, J.; Fogg, G. E., Recent developments in the chemistry of nitrogen fixation. *Proceedings of the Royal Society of London. Series B. Biological Sciences* **1969,** *172* (1029), 327-337.
54. Erisman, J. W.; Sutton, M. A.; Galloway, J.; Klimont, Z.; Winiwarter, W., How a century of ammonia synthesis changed the world. *Nature Geoscience* **2008,** *1* (10), 636-639.
55. Cherkasov, N.; Ibhadon, A. O.; Fitzpatrick, P., A review of the existing and alternative methods for greener nitrogen fixation. *Chemical Engineering and Processing: Process Intensification* **2015,** *90*, 24-33.
56. Wendeborn, S., The Chemistry, Biology, and Modulation of Ammonium Nitrification in Soil. *Angewandte Chemie International Edition* **2020,** *59* (6), 2182-2202.
57. Forrest, S. J. K.; Schluschaß, B.; Yuzik-Klimova, E. Y.; Schneider, S., Nitrogen Fixation via Splitting into Nitrido Complexes. *Chemical Reviews* **2021,** *121* (11), 6522-6587.
58. Krewald, V., Dinitrogen photoactivation: status quo and future perspectives. *Dalton Transactions* **2018,** *47* (31), 10320-10329.
59. Hoffman, B. M.; Lukoyanov, D.; Yang, Z.-Y.; Dean, D. R.; Seefeldt, L. C., Mechanism of Nitrogen Fixation by Nitrogenase: The Next Stage. *Chemical Reviews* **2014,** *114* (8), 4041-4062.
60. Ohki, Y.; Munakata, K.; Matsuoka, Y.; Hara, R.; Kachi, M.; Uchida, K.; Tada, M.; Cramer, R. E.; Sameera, W. M. C.; Takayama, T.; Sakai, Y.; Kuriyama, S.; Nishibayashi, Y.; Tanifuji, K., Nitrogen reduction by the Fe sites of synthetic [Mo3S4Fe] cubes. *Nature* **2022,** *607* (7917), 86-90.
61. Fritz, M.; Rupp, S.; Kiene, C. I.; Kisan, S.; Telser, J.; Würtele, C.; Krewald, V.; Schneider, S., Photoelectrochemical Conversion of Dinitrogen to Benzonitrile: Selectivity Control by Electrophile- versus Proton-Coupled Electron Transfer. *Angewandte Chemie International Edition 61* (35).
62. Speelman, A. L.; Čorić, I.; Van Stappen, C.; DeBeer, S.; Mercado, B. Q.; Holland, P. L., Nitrogenase-Relevant Reactivity of a Synthetic Iron–Sulfur–Carbon Site. *Journal of the American Chemical Society* **2019,** *141* (33), 13148-13157.
63. Singh, D.; Buratto, W. R.; Torres, J. F.; Murray, L. J., Activation of Dinitrogen by Polynuclear Metal Complexes. *Chemical Reviews* **2020,** *120* (12), 5517-5581.
64. Roux, Y.; Duboc, C.; Gennari, M., Molecular Catalysts for N2 Reduction: State of the Art, Mechanism, and Challenges. *ChemPhysChem* **2017,** *18* (19), 2606-2617.

65. Mayer, S. M.; Lawson, D. M.; Gormal, C. A.; Roe, S. M.; Smith, B. E., New insights into structure-function relationships in nitrogenase: a 1.6 Å resolution X-ray crystallographic study of Klebsiella pneumoniae MoFe-protein11Edited by D. C. Rees. *Journal of Molecular Biology* **1999,** *292* (4), 871-891.
66. Katayama, A.; Ohta, T.; Wasada-Tsutsui, Y.; Inomata, T.; Ozawa, T.; Ogura, T.; Masuda, H., Dinitrogen-Molybdenum Complex Induces Dinitrogen Cleavage by One-Electron Oxidation. *Angewandte Chemie International Edition* **2019,** *58* (33), 11279-11284.
67. Yandulov, D. V.; Schrock, R. R.; Rheingold, A. L.; Ceccarelli, C.; Davis, W. M., Synthesis and Reactions of Molybdenum Triamidoamine Complexes Containing Hexaisopropylterphenyl Substituents. *Inorganic Chemistry* **2003,** *42* (3), 796-813.
68. Arashiba, K.; Miyake, Y.; Nishibayashi, Y., A molybdenum complex bearing PNP-type pincer ligands leads to the catalytic reduction of dinitrogen into ammonia. *Nature Chemistry* **2011,** *3* (2), 120-125.
69. Anderson, J. S.; Rittle, J.; Peters, J. C., Catalytic conversion of nitrogen to ammonia by an iron model complex. *Nature* **2013,** *501* (7465), 84-87.
70. Ye, S.; Bill, E.; Neese, F., Electronic Structures of the [Fe(N2)(SiPiPr3)]+1/0/–1 Electron Transfer Series: A Counterintuitive Correlation between Isomer Shifts and Oxidation States. *Inorganic Chemistry* **2016,** *55* (7), 3468-3474.
71. Lee, Y.; Mankad, N. P.; Peters, J. C., Triggering N2 uptake via redox-induced expulsion of coordinated NH3 and N2 silylation at trigonal bipyramidal iron. *Nature Chemistry* **2010,** *2* (7), 558-565.
72. Vyas, N.; Sen, A.; Kumar, A.; Grover, A., Computational study of ammonia generation by iron(III) and iron(IV) complexes supported by trigonal bipyramidal iron. *International Journal of Quantum Chemistry* **2021,** *121* (21), e26775.
73. Vyas, N.; Pandey, B.; Ojha, A.; Grover, A., Revisiting mechanistic studies on dinitrogen reduction to ammonia by an iron dinitrogen complex as nitrogenase mimic. *International Journal of Quantum Chemistry* **2019,** *119* (24), e26025.
74. Simons, J., Why Is Quantum Chemistry So Complicated? *Journal of the American Chemical Society* **2023,** *145* (8), 4343-4354.
75. Kruse, H.; Goerigk, L.; Grimme, S., Why the Standard B3LYP/6-31G* Model Chemistry Should Not Be Used in DFT Calculations of Molecular Thermochemistry: Understanding and Correcting the Problem. *The Journal of Organic Chemistry* **2012,** *77* (23), 10824-10834.
76. Bartlett, R. J.; Musiał, M., Coupled-cluster theory in quantum chemistry. *Reviews of Modern Physics* **2007,** *79* (1), 291-352.
77. Riplinger, C.; Pinski, P.; Becker, U.; Valeev, E. F.; Neese, F., Sparse maps—A systematic infrastructure for reduced-scaling electronic structure methods. II. Linear scaling domain based pair natural orbital coupled cluster theory. *The Journal of Chemical Physics* **2016,** *144* (2), 024109.

78. Perdew, J. P.; Schmidt, K., Jacob's ladder of density functional approximations for the exchange-correlation energy. *AIP Conference Proceedings* **2001,** *577* (1), 1-20.
79. Parr, R. G. In *Density Functional Theory of Atoms and Molecules*, Horizons of Quantum Chemistry, Dordrecht, 1980//; Fukui, K.; Pullman, B., Eds. Springer Netherlands: Dordrecht, 1980; pp 5-15.
80. Bursch, M.; Mewes, J.-M.; Hansen, A.; Grimme, S., Best-Practice DFT Protocols for Basic Molecular Computational Chemistry**. *Angewandte Chemie International Edition* **2022,** *61* (42), e202205735.
81. Morgante, P.; Peverati, R., The devil in the details: A tutorial review on some undervalued aspects of density functional theory calculations. *International Journal of Quantum Chemistry* **2020,** *120* (18), e26332.
82. Goerigk, L.; Mehta, N., A Trip to the Density Functional Theory Zoo: Warnings and Recommendations for the User. *Australian Journal of Chemistry* **2019,** *72* (8), 563-573.
83. Swart, M., A new family of hybrid density functionals. *Chemical Physics Letters* **2013,** *580*, 166-171.
84. Perdew, J. P.; Burke, K.; Wang, Y., Generalized gradient approximation for the exchange-correlation hole of a many-electron system. *Physical Review B* **1996,** *54* (23), 16533-16539.
85. Perdew, J. P.; Burke, K.; Ernzerhof, M., Generalized Gradient Approximation Made Simple. *Physical Review Letters* **1996,** *77* (18), 3865-3868.
86. Handy, N. C.; Cohen, A. J., Left-right correlation energy. *Molecular Physics* **2001,** *99* (5), 403-412.
87. Swart, M.; Ehlers, A. W.; Lammertsma *, K., Performance of the OPBE exchange-correlation functional. *Molecular Physics* **2004,** *102* (23-24), 2467-2474.
88. Grimme, S., Density functional theory with London dispersion corrections. *WIREs Computational Molecular Science* **2011,** *1* (2), 211-228.
89. Radoń, M., Benchmarking quantum chemistry methods for spin-state energetics of iron complexes against quantitative experimental data. *Physical Chemistry Chemical Physics* **2019,** *21* (9), 4854-4870.
90. Vlahovic, F.; Gruden, M.; Stepanovic, S.; Swart, M., Density functional approximations for consistent spin and oxidation states of oxoiron complexes. *International Journal of Quantum Chemistry* **2020,** *120* (5), e26121.
91. Boys, S. F.; Egerton, A. C., Electronic wave functions - I. A general method of calculation for the stationary states of any molecular system. *Proceedings of the Royal Society of London. Series A. Mathematical and Physical Sciences* **1950,** *200* (1063), 542-554.
92. Bao, J. L.; Gagliardi, L.; Truhlar, D. G., Self-Interaction Error in Density Functional Theory: An Appraisal. *The Journal of Physical Chemistry Letters* **2018,** *9* (9), 2353-2358.

93. Johansson, A. J.; Blomberg, M. R. A.; Siegbahn, P. E. M., Quantifying the effects of the self-interaction error in density functional theory: When do the delocalized states appear? II. Iron-oxo complexes and closed-shell substrate molecules. *The Journal of Chemical Physics* **2008,** *129* (15).
94. Grimme, S., Accurate description of van der Waals complexes by density functional theory including empirical corrections. *Journal of Computational Chemistry* **2004,** *25* (12), 1463-1473.
95. Grimme, S.; Huenerbein, R.; Ehrlich, S., On the Importance of the Dispersion Energy for the Thermodynamic Stability of Molecules. *ChemPhysChem* **2011,** *12* (7), 1258-1261.
96. Caldeweyher, E.; Ehlert, S.; Hansen, A.; Neugebauer, H.; Spicher, S.; Bannwarth, C.; Grimme, S., A generally applicable atomic-charge dependent London dispersion correction. *The Journal of Chemical Physics* **2019,** *150* (15), 154122.
97. Tomasi, J.; Mennucci, B.; Cammi, R., Quantum Mechanical Continuum Solvation Models. *Chemical Reviews* **2005,** *105* (8), 2999-3094.
98. Chung, L. W.; Sameera, W. M. C.; Ramozzi, R.; Page, A. J.; Hatanaka, M.; Petrova, G. P.; Harris, T. V.; Li, X.; Ke, Z.; Liu, F.; Li, H.-B.; Ding, L.; Morokuma, K., The ONIOM Method and Its Applications. *Chemical Reviews* **2015,** *115* (12), 5678-5796.
99. Wagen, C. C. *presto*, 2021.
100. Miertuš, S.; Scrocco, E.; Tomasi, J., Electrostatic interaction of a solute with a continuum. A direct utilizaion of AB initio molecular potentials for the prevision of solvent effects. *Chemical Physics* **1981,** *55* (1), 117-129.
101. Klamt, A.; Schüürmann, G., COSMO: a new approach to dielectric screening in solvents with explicit expressions for the screening energy and its gradient. *Journal of the Chemical Society, Perkin Transactions 2* **1993,** (5), 799-805.
102. Engel, E., Chapter 10 - Relativistic Density Functional Theory: Foundations and Basic Formalism. In *Theoretical and Computational Chemistry*, Schwerdtfeger, P., Ed. Elsevier: 2002; Vol. 11, pp 523-621.
103. Pyykko, P., Relativistic effects in structural chemistry. *Chemical Reviews* **1988,** *88* (3), 563-594.
104. Lenthe, E. v.; Baerends, E. J.; Snijders, J. G., Relativistic regular two-component Hamiltonians. *The Journal of Chemical Physics* **1993,** *99* (6), 4597-4610.
105. Dolg, M., Chapter 14 - Relativistic Effective Core Potentials. In *Theoretical and Computational Chemistry*, Schwerdtfeger, P., Ed. Elsevier: 2002; Vol. 11, pp 793-862.
106. Ribeiro, R. F.; Marenich, A. V.; Cramer, C. J.; Truhlar, D. G., Use of Solution-Phase Vibrational Frequencies in Continuum Models for the Free Energy of Solvation. *The Journal of Physical Chemistry B* **2011,** *115* (49), 14556-14562.
107. Runge, E.; Gross, E. K. U., Density-Functional Theory for Time-Dependent Systems. *Physical Review Letters* **1984,** *52* (12), 997-1000.
108. Rosa, A.; Ricciardi, G.; Gritsenko, O.; Baerends, E. J., Excitation Energies of Metal Complexes with Time-dependent Density Functional Theory. In *Principles and*

Applications of Density Functional Theory in Inorganic Chemistry I, Springer Berlin Heidelberg: Berlin, Heidelberg, 2004; pp 49-116.
109. Torrents, E., Ribonucleotide reductases: essential enzymes for bacterial life. *Front Cell Infect Microbiol* **2014,** *4*, 52.
110. Stenkamp, R. E., Hemerythrin. In *Encyclopedia of Inorganic and Bioinorganic Chemistry*, R.A. Scott ed.; 2011.
111. Ravi, M.; Ranocchiari, M.; van Bokhoven, J. A., The Direct Catalytic Oxidation of Methane to Methanol-A Critical Assessment. *Angew Chem Int Ed Engl* **2017,** *56* (52), 16464-16483.
112. Schlachta, T. P.; Anneser, M. R.; Schlagintweit, J. F.; Jakob, C. H. G.; Hintermeier, C.; Böth, A. D.; Haslinger, S.; Reich, R. M.; Kühn, F. E., Mimicking reactive high-valent diiron-μ2-oxo intermediates of nonheme enzymes by an iron tetracarbene complex. *Chemical Communications* **2021,** *57* (54), 6644-6647.
113. Wilkinson, E. C.; Dong, Y.; Zang, Y.; Fujii, H.; Fraczkiewicz, R.; Fraczkiewicz, G.; Czernuszewicz, R. S.; Que, L., Raman Signature of the Fe2O2 "Diamond" Core. *Journal of the American Chemical Society* **1998,** *120* (5), 955-962.
114. Zang, Y.; Dong, Y.; Que, L.; Kauffmann, K.; Muenck, E., The First Bis(.mu.-oxo)diiron(III) Complex. Structure and Magnetic Properties of [Fe2(.mu.-O)2(6TLA)2](ClO4)2. *Journal of the American Chemical Society* **1995,** *117* (3), 1169-1170.
115. Xue, G.; Wang, D.; De Hont, R.; Fiedler, A. T.; Shan, X.; Münck, E.; Que, L., A synthetic precedent for the [FeIV2(μ-O)2] diamond core proposed for methane monooxygenase intermediate Q. *Proceedings of the National Academy of Sciences* **2007,** *104* (52), 20713.
116. Skulan, A. J.; Hanson, M. A.; Hsu, H.-f.; Que, L.; Solomon, E. I., Spectroscopic Study of [Fe2O2(5-Et3-TPA)2]3+: Nature of the Fe2O2 Diamond Core and Its Possible Relevance to High-Valent Binuclear Non-Heme Enzyme Intermediates. *Journal of the American Chemical Society* **2003,** *125* (24), 7344-7356.
117. Hsu, H.-F.; Dong, Y.; Shu, L.; Young, V. G.; Que, L., Crystal Structure of a Synthetic High-Valent Complex with an Fe2(μ-O)2 Diamond Core. Implications for the Core Structures of Methane Monooxygenase Intermediate Q and Ribonucleotide Reductase Intermediate X. *Journal of the American Chemical Society* **1999,** *121* (22), 5230-5237.
118. Zheng, H.; Zang, Y.; Dong, Y.; Young, V. G.; Que, L., Complexes with FeIII2(μ-O)(μ-OH), FeIII2(μ-O)2, and [FeIII3(μ2-O)3] Cores: Structures, Spectroscopy, and Core Interconversions. *Journal of the American Chemical Society* **1999,** *121* (10), 2226-2235.
119. Zhang, X.; Furutachi, H.; Fujinami, S.; Nagatomo, S.; Maeda, Y.; Watanabe, Y.; Kitagawa, T.; Suzuki, M., Structural and Spectroscopic Characterization of (μ-Hydroxo or μ-Oxo)(μ-peroxo)diiron(III) Complexes: Models for Peroxo Intermediates of Non-Heme Diiron Proteins. *Journal of the American Chemical Society* **2005,** *127* (3), 826-827.

120. Dong, Y.; Zang, Y.; Shu, L.; Wilkinson, E. C.; Que, L.; Kauffmann, K.; Münck, E., Models for Nonheme Diiron Enzymes. Assembly of a High-Valent Fe2(μ-O)2 Diamond Core from Its Peroxo Precursor. *Journal of the American Chemical Society* **1997,** *119* (51), 12683-12684.
121. Fiedler, A. T.; Shan, X.; Mehn, M. P.; Kaizer, J.; Torelli, S.; Frisch, J. R.; Kodera, M.; Que, J. L., Spectroscopic and Computational Studies of (μ-Oxo)(μ-1,2-peroxo)diiron(III) Complexes of Relevance to Nonheme Diiron Oxygenase Intermediates. *The Journal of Physical Chemistry A* **2008,** *112* (50), 13037-13044.
122. Cranswick, M. A.; Meier, K. K.; Shan, X.; Stubna, A.; Kaizer, J.; Mehn, M. P.; Münck, E.; Que, L., Protonation of a Peroxodiiron(III) Complex and Conversion to a Diiron(III/IV) Intermediate: Implications for Proton-Assisted O–O Bond Cleavage in Nonheme Diiron Enzymes. *Inorganic Chemistry* **2012,** *51* (19), 10417-10426.
123. Kryatov, S. V.; Taktak, S.; Korendovych, I. V.; Rybak-Akimova, E. V.; Kaizer, J.; Torelli, S.; Shan, X.; Mandal, S.; MacMurdo, V. L.; Mairata i Payeras, A.; Que, L., Dioxygen Binding to Complexes with FeII2(μ-OH)2 Cores: Steric Control of Activation Barriers and O2-Adduct Formation. *Inorganic Chemistry* **2005,** *44* (1), 85-99.
124. Draksharapu, A.; Xu, S.; Que Jr, L., CeIV- and HClO4-Promoted Assembly of an Fe2IV(μ-O)2 Diamond Core from its Monomeric FeIV=O Precursor at Room Temperature. *Angewandte Chemie International Edition* **2020,** *59* (50), 22484-22488.
125. Abelson, C. S.; Aboelenen, A. M.; Rasheed, W.; Que, L., 8.17 - Synthetic Nonheme High-Valent Iron-Oxo Complexes Structures and Oxidative Function. In *Comprehensive Coordination Chemistry III*, Constable, E. C.; Parkin, G.; Que Jr, L., Eds. Elsevier: Oxford, 2021; pp 412-454.
126. Sanders-Loehr, J.; Wheeler, W. D.; Shiemke, A. K.; Averill, B. A.; Loehr, T. M., Electronic and Raman spectroscopic properties of oxo-bridged dinuclear iron centers in proteins and model compounds. *Journal of the American Chemical Society* **1989,** *111* (21), 8084-8093.
127. Norman, R. E.; Holz, R. C.; Menage, S.; Que, L.; Zhang, J. H.; O'Connor, C. J., Structures and properties of dibridged (.mu.-oxo)diiron(III) complexes. Effects of the Fe-O-Fe angle. *Inorganic Chemistry* **1990,** *29* (23), 4629-4637.
128. Zimmermann, T. P.; Limpke, T.; Stammler, A.; Bögge, H.; Walleck, S.; Glaser, T., Variation of the Molecular and Electronic Structures of μ-Oxo Diferric Complexes with the Bridging Motive. *Zeitschrift für anorganische und allgemeine Chemie* **2018,** *644* (14), 683-691.
129. Chen, J.; Stepanovic, S.; Draksharapu, A.; Gruden, M.; Browne, W. R., A Non-Heme Iron Photocatalyst for Light-Driven Aerobic Oxidation of Methanol. *Angew Chem Int Ed Engl* **2018,** *57* (12), 3207-3211.
130. Swart, M.; Bickelhaupt, F. M., QUILD: QUantum-regions interconnected by local descriptions. *J Comput Chem* **2008,** *29* (5), 724-34.
131. *ADF 2019.3*, 2019.3; SCM, Theoretical Chemistry, Vrije Universiteit, Amsterdam, The Netherlands.

132. te Velde, G.; Bickelhaupt, F. M.; Baerends, E. J.; Fonseca Guerra, C.; van Gisbergen, S. J. A.; Snijders, J. G.; Ziegler, T., Chemistry with ADF. *Journal of Computational Chemistry* **2001,** *22* (9), 931-967.
133. Pye, C. C.; Ziegler, T., An implementation of the conductor-like screening model of solvation within the Amsterdam density functional package. *Theoretical Chemistry Accounts* **1999,** *101* (6), 396-408.
134. Van Lenthe, E.; Baerends, E. J., Optimized Slater-type basis sets for the elements 1–118. *Journal of Computational Chemistry* **2003,** *24* (9), 1142-1156.
135. Do, L. H.; Xue, G.; Que, L.; Lippard, S. J., Evaluating the Identity and Diiron Core Transformations of a (μ-Oxo)diiron(III) Complex Supported by Electron-Rich Tris(pyridyl-2-methyl)amine Ligands. *Inorg. Chem.* **2012,** *51* (4), 2393-2402.
136. Spool, A.; Williams, I. D.; Lippard, S. J., Electronic and vibrational spectroscopic analysis of the (.mu.-oxo)bis(.mu.-carboxylato)diiron(III) core: a study of [Fe2O(O2CCH3)2(TACN)2]2+. *Inorg. Chem.* **1985,** *24* (14), 2156-2162.
137. Li, Z.-X.; Yu, M.-M.; Zhang, Y.-N.; Wei, L.-H., Tris(1,10-phenanthroline-[kappa]2N,N')iron(II) [mu]-oxido-bis[trichloridoferrate(III)] ethanol hemisolvate. *Acta Crystallographica Section E* **2008,** *64* (12), m1514.
138. Farmer, C. S.; Kurtz, D. M., Jr.; Liu, Z. J.; Wang, B. C.; Rose, J.; Ai, J.; Sanders-Loehr, J., The crystal structures of Phascolopsis gouldii wild type and L98Y methemerythrins: structural and functional alterations of the O2 binding pocket. *J Biol Inorg Chem* **2001,** *6* (4), 418-29.
139. Scarrow, R. C.; Maroney, M. J.; Palmer, S. M.; Que, L.; Roe, A. L.; Salowe, S. P.; Stubbe, J., EXAFS studies of binuclear iron proteins: hemerythrin and ribonucleotide reductase. *Journal of the American Chemical Society* **1987,** *109* (25), 7857-7864.
140. Younker, J. M.; Krest, C. M.; Jiang, W.; Krebs, C.; Bollinger, J. M.; Green, M. T., Structural Analysis of the Mn(IV)/Fe(III) Cofactor of Chlamydia trachomatis Ribonucleotide Reductase by Extended X-ray Absorption Fine Structure Spectroscopy and Density Functional Theory Calculations. *Journal of the American Chemical Society* **2008,** *130* (45), 15022-15027.
141. Martinie, R. J.; Blaesi, E. J.; Krebs, C.; Bollinger, J. M.; Silakov, A.; Pollock, C. J., Evidence for a Di-μ-oxo Diamond Core in the Mn(IV)/Fe(IV) Activation Intermediate of Ribonucleotide Reductase from Chlamydia trachomatis. *Journal of the American Chemical Society* **2017,** *139* (5), 1950-1957.
142. Dong, Y.; Fujii, H.; Hendrich, M. P.; Leising, R. A.; Pan, G.; Randall, C. R.; Wilkinson, E. C.; Zang, Y.; Que, L., A High-Valent Nonheme Iron Intermediate. Structure and Properties of [Fe2(.mu.-O)2(5-Me-TPA)2](ClO4)3. *Journal of the American Chemical Society* **1995,** *117* (10), 2778-2792.
143. Strautmann, J. B. H.; Dammers, S.; Limpke, T.; Parthier, J.; Zimmermann, T. P.; Walleck, S.; Heinze-Brückner, G.; Stammler, A.; Bögge, H.; Glaser, T., Design and synthesis of a dinucleating ligand system with varying terminal donor functions that

provides no bridging donor and its application to the synthesis of a series of FeIII–μ-O–FeIII complexes. *Dalton Transactions* **2016,** *45* (8), 3340-3361.
144. Unjaroen, D.; Swart, M.; Browne, W. R., Electrochemical Polymerization of Iron(III) Polypyridyl Complexes through C–C Coupling of Redox Non-innocent Phenolato Ligands. *Inorg. Chem.* **2017,** *56* (1), 470-479.
145. Martins, F. F. *GirSS - Girona's Spectrum to Structure Calculator*, 1.0.0; 2021.
146. Ligtenbarg, A. G. J.; Oosting, P.; Roelfes, G.; Crois, R. M. L.; Lutz, M.; Spek, A. L.; Hage, R.; Feringa, B. L., Efficient catalytic oxidation of primary and secondary alcohols using a non-heme dinuclear iron complex. *Chem. Commun.* **2001,** (4), 385-386.
147. Bowman, S. E. J.; Bren, K. L., The chemistry and biochemistry of hemec: functional bases for covalent attachment. *Natural Product Reports* **2008,** *25* (6), 1118-1130.
148. Bonnett, R., The Chemistry of the Vitamin B12 Group. *Chemical Reviews* **1963,** *63* (6), 573-605.
149. Pareek, S.; Sagar, N. A.; Sharma, S.; Kumar, V.; Agarwal, T.; González-Aguilar, G. A.; Yahia, E. M., Chlorophylls: Chemistry and biological functions. *Fruit and Vegetable Phytochemicals* **2017,** *29*, 269.
150. Drain, C. M.; Varotto, A.; Radivojevic, I., Self-Organized Porphyrinic Materials. *Chemical Reviews* **2009,** *109* (5), 1630-1658.
151. Pushpanandan, P.; Ravikanth, M., Neo-Porphyrinoids: New Members of the Porphyrinoid Family. *Topics in Current Chemistry* **2021,** *379* (4), 26.
152. Chmielewski, P. J.; Latos-Grażyński, L.; Rachlewicz, K.; Glowiak, T., Tetra-p-tolylporphyrin with an Inverted Pyrrole Ring: A Novel Isomer of Porphyrin. *Angewandte Chemie International Edition* **1994,** *33* (7), 779-781.
153. Furuta, H.; Asano, T.; Ogawa, T., "N-Confused Porphyrin": A New Isomer of Tetraphenylporphyrin. *Journal of the American Chemical Society* **1994,** *116* (2), 767-768.
154. Furuta, H.; Ishizuka, T.; Osuka, A.; Dejima, H.; Nakagawa, H.; Ishikawa, Y., NH Tautomerism of N-Confused Porphyrin. *Journal of the American Chemical Society* **2001,** *123* (25), 6207-6208.
155. Marchand, G.; Roy, H.; Mendive-Tapia, D.; Jacquemin, D., N-confused porphyrin tautomers: lessons from density functional theory. *Physical Chemistry Chemical Physics* **2015,** *17* (7), 5290-5297.
156. Tuersun, M.; Kerim, A., A study on the aromaticity and magnetic properties of N-confused porphyrins. *Royal Society Open Science 7* (7), 200069.
157. Furuta, H.; Maeda, H.; Osuka, A., Theoretical Study of Stability, Structures, and Aromaticity of Multiply N-Confused Porphyrins. *The Journal of Organic Chemistry* **2001,** *66* (25), 8563-8572.
158. Babu, B.; Mack, J.; Nyokong, T., A heavy-atom-free π-extended N-confused porphyrin as a photosensitizer for photodynamic therapy. *New Journal of Chemistry* **2021,** *45* (12), 5654-5658.

159. Wang, L.-L.; Peng, S.-H.; Wang, H.; Ji, L.-N.; Liu, H.-Y., Photophysical properties of free-base and manganese(iii) N-confused porphyrins. *Physical Chemistry Chemical Physics* **2018,** *20* (30), 20141-20148.
160. Khodov, I. A.; Maltceva, O. V.; Klochkov, V. V.; Koifman, O. I.; Mamardashvili, N. Z., N-Confused porphyrins: complexation and 1H NMR studies. *New Journal of Chemistry* **2017,** *41* (16), 7932-7937.
161. Fukuda, M.; Mori, S.; Furuta, H.; Shimizu, S., N-Confused Porphyrin-aza-Dipyrrin Chimera: A Versatile Metal Coordination Ligand Using its Unique NH Tautomerism. *Chemistry – An Asian Journal* **2019,** *14* (10), 1697-1702.
162. Miyazaki, T.; Fukuyama, K.; Mashita, S.; Deguchi, Y.; Yamamoto, T.; Ishida, M.; Mori, S.; Furuta, H., Ruthenium N-Confused Porphyrins: Selective Reactivity for Ambident 2-Heteroatom-Substituted Pyridines Serving as Axial Ligands. *ChemPlusChem* **2019,** *84* (6), 603-607.
163. Halder, N.; Dzhemileva, L. U.; Ramazanov, I. R.; D'Yakonov, V. A.; Dzhemilev, U. M.; Rath, H., Comparative in vitro Studies of the Topoisomerase I Inhibition and Anticancer Activities of Metallated N-Confused Porphyrins and Metallated Porphyrins. *ChemMedChem* **2020,** *15* (7), 632-642.
164. dela Cruz, J.-a. B.; Hung, C.-H., Ni and Zn N-confused porphyrin complexes as recyclable catalysts for high efficiency solvent-free CO2 fixation into cyclic carbonates. *Catalysis Science & Technology* **2021,** *11* (6), 2144-2154.
165. Ge, Y.; Cheng, G.; Xu, N.; Wang, W.; Ke, H., Zinc 2-N-methyl N-confused porphyrin: an efficient catalyst for the conversion of CO2 into cyclic carbonates. *Catalysis Science & Technology* **2019,** *9* (16), 4255-4261.
166. dela Cruz, J.-a. B.; Ruamps, M.; Arco, S.; Hung, C.-H., Ni and Pd N-confused porphyrin complexes as catalysts for the synthesis of cyclic carbonates from epoxides and CO2. *Dalton Transactions* **2019,** *48* (22), 7527-7531.
167. Grover, N.; Sankar, M., N-Confused Porphyrin – A Unique "Turn-On" Chemosensor for CN– and F– ions and "Turn-Off" Sensor for ClO4– ions. *Chemistry – An Asian Journal* **2020,** *15* (14), 2192-2197.
168. Babu, B.; Mack, J.; Nyokong, T., Sn(iv) N-confused porphyrins as photosensitizer dyes for photodynamic therapy in the near IR region. *Dalton Transactions* **2020,** *49* (43), 15180-15183.
169. Sripothongnak, S.; Ziegler, C. J.; Dahlby, M. R.; Nemykin, V. N., Controllable and Reversible Inversion of the Electronic Structure in Nickel N-Confused Porphyrin: A Case When MCD Matters. *Inorganic Chemistry* **2011,** *50* (15), 6902-6909.
170. Miyazaki, T.; Yamamoto, T.; Mashita, S.; Deguchi, Y.; Fukuyama, K.; Ishida, M.; Mori, S.; Furuta, H., N-Confused Porphyrin Metal Complexes with an Axial Pyridine Directly Tethered from an Inner Carbon: A Bioinspired Ligand as a Versatile Platform for Catalysis. *European Journal of Inorganic Chemistry* **2018,** *2018* (2), 203-207.
171. Yang, C.-H.; Dzugan, S. J.; Goedken, V. L., Synthesis and structural characterization of the metalloporphyrin dimer, [Mo(TPP)]2, the first product from

the reaction of Mo(CO)6 with H2TPP (tetraphenylporphyrin). *Journal of the Chemical Society, Chemical Communications* **1986,** (17), 1313-1315.
172. Swart, M., Bond orders in metalloporphyrins. *Theoretical Chemistry Accounts* **2020,** *139* (10), 160.
173. Liu, J.; Fan, Y.-Z.; Li, X.; Wei, Z.; Xu, Y.-W.; Zhang, L.; Su, C.-Y., A porous rhodium(III)-porphyrin metal-organic framework as an efficient and selective photocatalyst for CO2 reduction. *Applied Catalysis B: Environmental* **2018,** *231*, 173-181.
174. Huang, T.; Wu, X.; Weare, W. W.; Sommer, R. D., Mono-Oxido-Bridged Heterobimetallic and Heterotrimetallic Compounds Containing Titanium(IV) and Chromium(III). *European Journal of Inorganic Chemistry* **2014,** *2014* (33), 5662-5674.
175. Smieja, J. A.; Omberg, K. M.; Busuego, L. N.; Breneman, G. L., Synthesis and characterization of dichloro[5,10,15,20-tetrakis(p-tolyl)porphyrinato]osmium(IV), a potential precursor to organometallic porphyrinato complexes of osmium. *Polyhedron* **1994,** *13* (3), 339-343.
176. Blusch, L. K.; Craigo, K. E.; Martin-Diaconescu, V.; McQuarters, A. B.; Bill, E.; Dechert, S.; DeBeer, S.; Lehnert, N.; Meyer, F., Hidden Non-Innocence in an Expanded Porphyrin: Electronic Structure of the Siamese-Twin Porphyrin's Dicopper Complex in Different Oxidation States. *Journal of the American Chemical Society* **2013,** *135* (37), 13892-13899.
177. Sit, P. H. L.; Car, R.; Cohen, M. H.; Selloni, A., Simple, Unambiguous Theoretical Approach to Oxidation State Determination via First-Principles Calculations. *Inorganic Chemistry* **2011,** *50* (20), 10259-10267.
178. Mehara, J.; Koovakattil Surendran, A.; van Wieringen, T.; Setia, D.; Foroutan-Nejad, C.; Straka, M.; Rulíšek, L.; Roithová, J., Cationic Gold(II) Complexes: Experimental and Theoretical Study**. *Chemistry – A European Journal* **2022,** *28* (60), e202201794.
179. Day, C. S.; Do, C. D.; Odena, C.; Benet-Buchholz, J.; Xu, L.; Foroutan-Nejad, C.; Hopmann, K. H.; Martin, R., Room-Temperature-Stable Magnesium Electride via Ni(II) Reduction. *Journal of the American Chemical Society* **2022,** *144* (29), 13109-13117.
180. Rodríguez, J. I.; Ayers, P. W.; Götz, A. W.; Castillo-Alvarado, F. L., Virial theorem in the Kohn–Sham density-functional theory formalism: Accurate calculation of the atomic quantum theory of atoms in molecules energies. *The Journal of Chemical Physics* **2009,** *131* (2), 021101.
181. Kitaura, K.; Morokuma, K., A new energy decomposition scheme for molecular interactions within the Hartree-Fock approximation. *International Journal of Quantum Chemistry* **1976,** *10* (2), 325-340.
182. Kingsbury, C. J.; Senge, M. O., The shape of porphyrins. *Coordination Chemistry Reviews* **2021,** *431*, 213760.
183. Alvarez, S.; Alemany, P.; Casanova, D.; Cirera, J.; Llunell, M.; Avnir, D., Shape maps and polyhedral interconversion paths in transition metal chemistry. *Coordination Chemistry Reviews* **2005,** *249* (17), 1693-1708.

184. Casanova, D.; Cirera, J.; Llunell, M.; Alemany, P.; Avnir, D.; Alvarez, S., Minimal Distortion Pathways in Polyhedral Rearrangements. *Journal of the American Chemical Society* **2004,** *126* (6), 1755-1763.
185. Cirera, J.; Ruiz, E.; Alvarez, S., Shape and Spin State in Four-Coordinate Transition-Metal Complexes: The Case of the d6 Configuration. *Chemistry – A European Journal* **2006,** *12* (11), 3162-3167.
186. Alvarez, S.; Llunell, M., Continuous symmetry measures of penta-coordinate molecules: Berry and non-Berry distortions of the trigonal bipyramid. *Journal of the Chemical Society, Dalton Transactions* **2000,** (19), 3288-3303.
187. Gouterman, M., Spectra of porphyrins. *Journal of Molecular Spectroscopy* **1961,** *6*, 138-163.
188. Baerends, E. J.; Ricciardi, G.; Rosa, A.; van Gisbergen, S. J. A., A DFT/TDDFT interpretation of the ground and excited states of porphyrin and porphyrazine complexes. *Coordination Chemistry Reviews* **2002,** *230* (1), 5-27.
189. Liao, M.-S.; Scheiner, S., Electronic structure and bonding in metal porphyrins, metal=Fe, Co, Ni, Cu, Zn. *The Journal of Chemical Physics* **2002,** *117* (1), 205-219.
190. Wang, Q.; Song, M.; Song, X.; Bu, Y., Unexpected diradical character and large magnetic spin coupling in modified porphyrins induced by inverting pyrrole rings. *Physical Chemistry Chemical Physics* **2019,** *21* (31), 17209-17220.
191. Arakawa, H.; Aresta, M.; Armor, J. N.; Barteau, M. A.; Beckman, E. J.; Bell, A. T.; Bercaw, J. E.; Creutz, C.; Dinjus, E.; Dixon, D. A.; Domen, K.; DuBois, D. L.; Eckert, J.; Fujita, E.; Gibson, D. H.; Goddard, W. A.; Goodman, D. W.; Keller, J.; Kubas, G. J.; Kung, H. H.; Lyons, J. E.; Manzer, L. E.; Marks, T. J.; Morokuma, K.; Nicholas, K. M.; Periana, R.; Que, L.; Rostrup-Nielson, J.; Sachtler, W. M. H.; Schmidt, L. D.; Sen, A.; Somorjai, G. A.; Stair, P. C.; Stults, B. R.; Tumas, W., Catalysis Research of Relevance to Carbon Management: Progress, Challenges, and Opportunities. *Chemical Reviews* **2001,** *101* (4), 953-996.
192. Ritleng, V.; Sirlin, C.; Pfeffer, M., Ru-, Rh-, and Pd-Catalyzed C–C Bond Formation Involving C–H Activation and Addition on Unsaturated Substrates: Reactions and Mechanistic Aspects. *Chemical Reviews* **2002,** *102* (5), 1731-1770.
193. Que, L.; Tolman, W. B., Biologically inspired oxidation catalysis. *Nature* **2008,** *455* (7211), 333-340.
194. Mondal, P.; Pirovano, P.; Das, A.; Farquhar, E. R.; McDonald, A. R., Hydrogen Atom Transfer by a High-Valent Nickel-Chloride Complex. *Journal of the American Chemical Society* **2018,** *140* (5), 1834-1841.
195. Mondal, P.; Lovisari, M.; Twamley, B.; McDonald, A. R., Fast Hydrocarbon Oxidation by a High-Valent Nickel–Fluoride Complex. *Angewandte Chemie International Edition* **2020,** *59* (31), 13044-13050.
196. Zhou, A.; Li, X.-X.; Sun, D.; Cao, X.; Wu, Z.; Chen, H.; Zhao, Y.; Nam, W.; Wang, Y., Theoretical investigation on the elusive structure–activity relationship of

bioinspired high-valence nickel–halogen complexes in oxidative fluorination reactions. *Dalton Transactions* **2023,** *52* (7), 1977-1988.
197. Schlangen, M.; Neugebauer, J.; Reiher, M.; Schröder, D.; López, J. P.; Haryono, M.; Heinemann, F. W.; Grohmann, A.; Schwarz, H., Gas-Phase C–H and N–H Bond Activation by a High Valent Nitrido-Iron Dication and 〈NH〉-Transfer to Activated Olefins. *Journal of the American Chemical Society* **2008,** *130* (13), 4285-4294.
198. Donald, W. A.; McKenzie, C. J.; O'Hair, R. A. J., C□H Bond Activation of Methanol and Ethanol by a High-Spin FeIVO Biomimetic Complex. *Angewandte Chemie International Edition* **2011,** *50* (36), 8379-8383.
199. Schröder, D.; Wesendrup, R.; Schalley, C. A.; Zummack, W.; Schwarz, H., Gas-Phase Reactions of Aliphatic Alcohols with 'Bare' FeO+. *Helvetica Chimica Acta* **1996,** *79* (1), 123-132.
200. Gopinathan, M. S.; Jug, K., Valency. I. A quantum chemical definition and properties. *Theoretica chimica acta* **1983,** *63* (6), 497-509.
201. Chatterjee, B.; Chang, W.-C.; Jena, S.; Werlé, C., Implementation of Cooperative Designs in Polarized Transition Metal Systems—Significance for Bond Activation and Catalysis. *ACS Catalysis* **2020,** *10* (23), 14024-14055.
202. Elvers, B. J.; Pätsch, S.; Bandaru, S. S. M.; Krewald, V.; Schulzke, C.; Fischer, C., Fine-Tuning Redox Properties of Heteroleptic Molybdenum Complexes through Ligand-Ligand-Cooperativity. *Angewandte Chemie International Edition n/a* (n/a), e202303151.
203. Schendzielorz, F.; Finger, M.; Abbenseth, J.; Würtele, C.; Krewald, V.; Schneider, S., Metal-Ligand Cooperative Synthesis of Benzonitrile by Electrochemical Reduction and Photolytic Splitting of Dinitrogen. *Angewandte Chemie International Edition* **2019,** *58* (3), 830-834.
204. Doyle, L. R.; Wooles, A. J.; Liddle, S. T., Bimetallic Cooperative Cleavage of Dinitrogen to Nitride and Tandem Frustrated Lewis Pair Hydrogenation to Ammonia. *Angewandte Chemie International Edition* **2019,** *58* (20), 6674-6677.
205. Askevold, B.; Nieto, J. T.; Tussupbayev, S.; Diefenbach, M.; Herdtweck, E.; Holthausen, M. C.; Schneider, S., Ammonia formation by metal–ligand cooperative hydrogenolysis of a nitrido ligand. *Nature Chemistry* **2011,** *3* (7), 532-537.
206. Gambarotta, S.; Scott, J., Multimetallic Cooperative Activation of N2. *Angewandte Chemie International Edition* **2004,** *43* (40), 5298-5308.
207. Kilgore, U. J.; Yang, X.; Tomaszewski, J.; Huffman, J. C.; Mindiola, D. J., Activation of Atmospheric Nitrogen and Azobenzene NN Bond Cleavage by a Transient Nb(III) Complex. *Inorganic Chemistry* **2006,** *45* (26), 10712-10721.
208. Bae, D. Y.; Lee, G.; Lee, E., Fixation of Dinitrogen at an Asymmetric Binuclear Titanium Complex. *Inorganic Chemistry* **2021,** *60* (17), 12813-12822.
209. Nishibayashi, Y.; Iwai, S.; Hidai, M., Bimetallic System for Nitrogen Fixation: Ruthenium-Assisted Protonation of Coordinated N_2 on Tungsten with H_2. *Science* **1998,** *279* (5350), 540-542.

210. Robson, R., Lewis base behavior of einitrogen and carbonyl complexes of rhenium toward titanium tetrachloride and related species. *Inorganic Chemistry* **1974,** *13* (2), 475-479.
211. Mercer, M.; Crabtree, R. H.; Richards, R. L., A μ-dinitrogen complex with a long N–N bond. X-Ray crystal structure of [(PMe2Ph)4ClReN2MoCl4(OMe)]. *Journal of the Chemical Society, Chemical Communications* **1973,** (21), 808-809.
212. Mercer, M., Crystal structure of a dinuclear dinitrogen complex: tetrachloro-{chlorotetrakis[dimethyl(phenyl)phosphine]rhenium(I)}-μ-dinitrogen-methoxymolybdenum(V)–methanol–hydrochloric acid. *Journal of the Chemical Society, Dalton Transactions* **1974,** (16), 1637-1640.
213. Zhang, Q.-F.; Chim, J. L. C.; Lai, W.; Wong, W.-T.; Leung, W.-H., Bridged Dinitrogen Complexes of Iron and Chromium Porphyrins. *Inorganic Chemistry* **2001,** *40* (11), 2470-2471.
214. Muller, P., Glossary of terms used in physical organic chemistry (IUPAC Recommendations 1994). *Pure and Applied Chemistry* **1994,** *66* (5), 1077-1184.
215. Shanahan, J. P.; Szymczak, N. K., Lewis Acid Effects on Calculated Ligand Electronic Parameters. *Organometallics* **2020,** *39* (23), 4297-4306.
216. Shi, L.; Li, Q.; Ling, C.; Zhang, Y.; Ouyang, Y.; Bai, X.; Wang, J., Metal-free electrocatalyst for reducing nitrogen to ammonia using a Lewis acid pair. *Journal of Materials Chemistry A* **2019,** *7* (9), 4865-4871.
217. Khan, S. N.; Kalemos, A.; Miliordos, E., Metal-Free Activation of N2 by Persistent Carbene Pairs: An Ab Initio Investigation. *The Journal of Physical Chemistry C* **2019,** *123* (35), 21548-21553.
218. Rouf, A. M.; Dai, C.; Dong, S.; Zhu, J., Screening Borane Species for Dinitrogen Activation. *Inorganic Chemistry* **2020,** *59* (16), 11770-11781.
219. Wech, F.; Gellrich, U., In Situ Formation of an Efficient Catalyst for the Semihydrogenation of Alkynes from Imidazolone and BH3. *ACS Catalysis* **2022**, 5388-5396.
220. Specklin, D.; Coffinet, A.; Vendier, L.; del Rosal, I.; Dinoi, C.; Simonneau, A., Synthesis, Characterization, and Comparative Theoretical Investigation of Dinitrogen-Bridged Group 6-Gold Heterobimetallic Complexes. *Inorganic Chemistry* **2021,** *60* (8), 5545-5562.
221. Coffinet, A. s.; Simonneau, A.; Specklin, D., Push–Pull Activation of N2: Coordination of Lewis Acids to Dinitrogen Complexes. In *Encyclopedia of Inorganic and Bioinorganic Chemistry*, Scott, R. A., Ed. John Wiley & Sons: Hoboken, 2020; pp 1-25.
222. Geri, J. B.; Shanahan, J. P.; Szymczak, N. K., Testing the Push–Pull Hypothesis: Lewis Acid Augmented N2 Activation at Iron. *Journal of the American Chemical Society* **2017,** *139* (16), 5952-5956.
223. Ruddy, A. J.; Ould, D. M. C.; Newman, P. D.; Melen, R. L., Push and pull: the potential role of boron in N2 activation. *Dalton Transactions* **2018,** *47* (31), 10377-10381.

224. Simonneau, A.; Etienne, M., Enhanced Activation of Coordinated Dinitrogen with p-Block Lewis Acids. *Chemistry – A European Journal* **2018,** *24* (48), 12458-12463.
225. Broere, D. L. J.; Holland, P. L., Boron compounds tackle dinitrogen. *Science* **2018,** *359* (6378), 871-871.
226. Chatt, J.; Dilworth, J. R.; Leigh, G. J., A series of nitrogen complexes of rhenium(I). *Journal of the Chemical Society D: Chemical Communications* **1969,** (13), 687-688.
227. Neyhart, G. A.; Seward, K.; Sullivan, B. P., A Rhenium(I) Dinitrogen Complex Containing a Tertiary Phosphine. In *Inorganic Syntheses*, 1996; pp 262-267.
228. Donovan-Mtunzi, S.; Richards, R. L.; Mason, J., Nitrogen-15 nuclear magnetic resonance spectroscopy of dinitrogen-bridged complexes. *Journal of the Chemical Society, Dalton Transactions* **1984,** (11), 2429-2433.
229. Chatt, J.; Fay, R. C.; Richards, R. L., Preparation and characterisation of the dinuclear dinitrogen complex, trichloro-μ-dinitrogen-bis(tetrahydrofuran){chlorotetrakis[dimethyl-(phenyl)phosphine]rhenium(I)}chromium(III)[(PMe2Ph)4ClReN2CrCl3(thf)2]. *Journal of the Chemical Society A: Inorganic, Physical, Theoretical* **1971,** (0), 702-704.
230. Lv, Z.-J.; Wei, J.; Zhang, W.-X.; Chen, P.; Deng, D.; Shi, Z.-J.; Xi, Z., Direct transformation of dinitrogen: synthesis of N-containing organic compounds via N–C bond formation. *National Science Review* **2020,** *7* (10), 1564-1583.
231. Khoenkhoen, N.; de Bruin, B.; Reek, J. N. H.; Dzik, W. I., Reactivity of Dinitrogen Bound to Mid- and Late-Transition-Metal Centers. *European Journal of Inorganic Chemistry* **2015,** *2015* (4), 567-598.
232. Junge, J.; Froitzheim, S.; Engesser, T. A.; Krahmer, J.; Näther, C.; Le Poul, N.; Tuczek, F., Tungsten and molybdenum dinitrogen complexes supported by a pentadentate tetrapodal phosphine ligand: comparative spectroscopic, electrochemical and reactivity studies. *Dalton Transactions* **2022,** *51* (16), 6166-6176.
233. Neese, F., The ORCA program system. *WIREs Computational Molecular Science* **2012,** *2* (1), 73-78.
234. Neese, F., Software update: The ORCA program system—Version 5.0. *WIREs Computational Molecular Science* **2022,** *n/a* (n/a), e1606.
235. Neese, F.; Wennmohs, F.; Becker, U.; Riplinger, C., The ORCA quantum chemistry program package. *The Journal of Chemical Physics* **2020,** *152* (22), 224108.
236. Becke, A. D., Density-functional exchange-energy approximation with correct asymptotic behavior. *Physical Review A* **1988,** *38* (6), 3098-3100.
237. Perdew, J. P., Density-functional approximation for the correlation energy of the inhomogeneous electron gas. *Physical Review B* **1986,** *33* (12), 8822-8824.
238. Weigend, F.; Ahlrichs, R., Balanced basis sets of split valence, triple zeta valence and quadruple zeta valence quality for H to Rn: Design and assessment of accuracy. *Physical Chemistry Chemical Physics* **2005,** *7* (18), 3297-3305.

239. Kendall, R. A.; Früchtl, H. A., The impact of the resolution of the identity approximate integral method on modern ab initio algorithm development. *Theoretical Chemistry Accounts* **1997,** *97* (1), 158-163.
240. Caldeweyher, E.; Bannwarth, C.; Grimme, S., Extension of the D3 dispersion coefficient model. *The Journal of Chemical Physics* **2017,** *147* (3), 034112.
241. Barone, V.; Cossi, M., Quantum Calculation of Molecular Energies and Energy Gradients in Solution by a Conductor Solvent Model. *The Journal of Physical Chemistry A* **1998,** *102* (11), 1995-2001.
242. van Alten, R. S.; Wätjen, F.; Demeshko, S.; Miller, A. J. M.; Würtele, C.; Siewert, I.; Schneider, S., (Electro-)chemical Splitting of Dinitrogen with a Rhenium Pincer Complex. *European Journal of Inorganic Chemistry* **2020,** *2020* (15-16), 1402-1410.
243. Alig, L.; Eisenlohr, K. A.; Zelenkova, Y.; Rosendahl, S.; Herbst-Irmer, R.; Demeshko, S.; Holthausen, M. C.; Schneider, S., Rhenium-Mediated Conversion of Dinitrogen and Nitric Oxide to Nitrous Oxide. *Angewandte Chemie International Edition* **2022,** *61* (2), e202113340.
244. Schluschaß, B.; Borter, J.-H.; Rupp, S.; Demeshko, S.; Herwig, C.; Limberg, C.; Maciulis, N. A.; Schneider, J.; Würtele, C.; Krewald, V.; Schwarzer, D.; Schneider, S., Cyanate Formation via Photolytic Splitting of Dinitrogen. *JACS Au* **2021,** *1* (6), 879-894.
245. Lindley, B. M.; van Alten, R. S.; Finger, M.; Schendzielorz, F.; Würtele, C.; Miller, A. J. M.; Siewert, I.; Schneider, S., Mechanism of Chemical and Electrochemical N2 Splitting by a Rhenium Pincer Complex. *Journal of the American Chemical Society* **2018,** *140* (25), 7922-7935.
246. Bruch, Q. J.; Lindley, B. M.; Askevold, B.; Schneider, S.; Miller, A. J. M., A Ruthenium Hydrido Dinitrogen Core Conserved across Multielectron/Multiproton Changes to the Pincer Ligand Backbone. *Inorganic Chemistry* **2018,** *57* (4), 1964-1975.
247. J. L. Pombeiro, A.; Teresa A. R. S. Costa, M.; Wang, Y.; F. Nixon, J., Syntheses and redox properties of the first phosphirene–dinitrogen and phosphirene–diazenide complexes. *Journal of the Chemical Society, Dalton Transactions* **1999,** (21), 3755-3758.
248. Álvarez-Moreno, M.; de Graaf, C.; López, N.; Maseras, F.; Poblet, J. M.; Bo, C., Managing the Computational Chemistry Big Data Problem: The ioChem-BD Platform. *Journal of Chemical Information and Modeling* **2015,** *55* (1), 95-103.
249. Wilkinson, M. D.; Dumontier, M.; Aalbersberg, I. J.; Appleton, G.; Axton, M.; Baak, A.; Blomberg, N.; Boiten, J.-W.; da Silva Santos, L. B.; Bourne, P. E.; Bouwman, J.; Brookes, A. J.; Clark, T.; Crosas, M.; Dillo, I.; Dumon, O.; Edmunds, S.; Evelo, C. T.; Finkers, R.; Gonzalez-Beltran, A.; Gray, A. J. G.; Groth, P.; Goble, C.; Grethe, J. S.; Heringa, J.; 't Hoen, P. A. C.; Hooft, R.; Kuhn, T.; Kok, R.; Kok, J.; Lusher, S. J.; Martone, M. E.; Mons, A.; Packer, A. L.; Persson, B.; Rocca-Serra, P.; Roos, M.; van Schaik, R.; Sansone, S.-A.; Schultes, E.; Sengstag, T.; Slater, T.; Strawn, G.; Swertz, M. A.; Thompson, M.; van der Lei, J.; van Mulligen, E.; Velterop, J.; Waagmeester,

A.; Wittenburg, P.; Wolstencroft, K.; Zhao, J.; Mons, B., The FAIR Guiding Principles for scientific data management and stewardship. *Scientific Data* **2016,** *3* (1), 160018.
250. Greb, L., Lewis Superacids: Classifications, Candidates, and Applications. *Chemistry – A European Journal* **2018,** *24* (68), 17881-17896.
251. Mayer, R. J.; Hampel, N.; Ofial, A. R., Lewis Acidic Boranes, Lewis Bases, and Equilibrium Constants: A Reliable Scaffold for a Quantitative Lewis Acidity/Basicity Scale. *Chemistry – A European Journal* **2021,** *27* (12), 4070-4080.
252. Gaffen, J., The Complexity of Simple: Measuring Lewis Acidity. *Chem* **2019,** *5* (6), 1355-1356.
253. Gaffen, J. R.; Bentley, J. N.; Torres, L. C.; Chu, C.; Baumgartner, T.; Caputo, C. B., A Simple and Effective Method of Determining Lewis Acidity by Using Fluorescence. *Chem* **2019,** *5* (6), 1567-1583.
254. Willcox, D.; Melen, R. L., Illuminating Lewis Acidity Strength. *Chem* **2019,** *5* (6), 1362-1363.
255. Mayer, U.; Gutmann, V.; Gerger, W., The acceptor number — A quantitative empirical parameter for the electrophilic properties of solvents. *Monatshefte für Chemie / Chemical Monthly* **1975,** *106* (6), 1235-1257.
256. Pelmenschikov, A. G.; van Santen, R. A.; Janchen, J.; Meijer, E., Acetonitrile-d3 as a probe of Lewis and Broensted acidity of zeolites. *The Journal of Physical Chemistry* **1993,** *97* (42), 11071-11074.
257. Fenwick, J. T. F.; Wilson, J. W., Thermochemical investigation into the Lewis acidity of the boron atom in some triaryloxyboranes. *Inorganic Chemistry* **1975,** *14* (7), 1602-1604.
258. Christe, K. O.; Dixon, D. A.; McLemore, D.; Wilson, W. W.; Sheehy, J. A.; Boatz, J. A., On a quantitative scale for Lewis acidity and recent progress in polynitrogen chemistry. *Journal of Fluorine Chemistry* **2000,** *101* (2), 151-153.
259. Haartz, J. C.; McDaniel, D. H., Fluoride ion affinity of some Lewis acids. *Journal of the American Chemical Society* **1973,** *95* (26), 8562-8565.
260. Yatsimirskii, K. B., Hydride affinity as a measure of acidity (electrophilicity). *Theoretical and Experimental Chemistry* **1981,** *17* (1), 75-79.
261. Böhrer, H.; Trapp, N.; Himmel, D.; Schleep, M.; Krossing, I., From unsuccessful H_2-activation with FLPs containing $B(Ohfip)_3$ to a systematic evaluation of the Lewis acidity of 33 Lewis acids based on fluoride, chloride, hydride and methyl ion affinities. *Dalton Transactions* **2015,** *44* (16), 7489-7499.
262. Krespan, C. G.; Dixon, D. A., Fluoroolefin condensation catalyzed by aluminum chlorofluoride. *Journal of Fluorine Chemistry* **1996,** *77* (2), 117-126.
263. Pearson, R. G., Hard and Soft Acids and Bases. *Journal of the American Chemical Society* **1963,** *85* (22), 3533-3539.
264. Campodónico, P. R.; Aizman, A.; Contreras, R., Electrophilicity of quinones and its relationship with hydride affinity. *Chemical Physics Letters* **2009,** *471* (1), 168-173.

265. Clark, E. R.; Del Grosso, A.; Ingleson, M. J., The Hydride-Ion Affinity of Borenium Cations and Their Propensity to Activate H2 in Frustrated Lewis Pairs. *Chemistry – A European Journal* **2013,** *19* (7), 2462-2466.
266. Saeidian, H.; Malekian, H.; Vessally, E., Density functional estimation of hydride and proton affinities of substituted allenes and heteroallenes. *Journal of Physical Organic Chemistry* **2021,** *34* (10), e4251.
267. Vianello, R.; Peran, N.; Maksić, Z. B., Hydride Affinities of Some Substituted Alkynes: Prediction by DFT Calculations and Rationalization by Triadic Formula. *The Journal of Physical Chemistry A* **2006,** *110* (47), 12870-12881.
268. Erdmann, P.; Leitner, J.; Schwarz, J.; Greb, L., An Extensive Set of Accurate Fluoride Ion Affinities for p-Block Element Lewis Acids and Basic Design Principles for Strong Fluoride Ion Acceptors. *ChemPhysChem* **2020,** *21* (10), 987-994.
269. Neese, F.; Hansen, A.; Liakos, D. G., Efficient and accurate approximations to the local coupled cluster singles doubles method using a truncated pair natural orbital basis. *The Journal of Chemical Physics* **2009,** *131* (6).
270. Neese, F.; Wennmohs, F.; Hansen, A., Efficient and accurate local approximations to coupled-electron pair approaches: An attempt to revive the pair natural orbital method. *The Journal of Chemical Physics* **2009,** *130* (11).
271. Riplinger, C.; Neese, F., An efficient and near linear scaling pair natural orbital based local coupled cluster method. *The Journal of Chemical Physics* **2013,** *138* (3).
272. Erdmann, P.; Greb, L., Multidimensional Lewis Acidity: A Consistent Data Set of Chloride, Hydride, Methide, Water and Ammonia Affinities for 183 p-Block Element Lewis Acids. *ChemPhysChem* **2021,** *22* (10), 935-943.
273. Laurence, C.; Graton, J.; Gal, J.-F., An Overview of Lewis Basicity and Affinity Scales. *Journal of Chemical Education* **2011,** *88* (12), 1651-1657.
274. Rupp, S.; Plasser, F.; Krewald, V., Multi-Tier Electronic Structure Analysis of Sita's Mo and W Complexes Capable of Thermal or Photochemical N2 Splitting. *European Journal of Inorganic Chemistry* **2020,** *2020* (15-16), 1506-1518.
275. Wasada-Tsutsui, Y.; Wasada, H.; Suzuki, T.; Katayama, A.; Kajita, Y.; Inomata, T.; Ozawa, T.; Masuda, H., Efficient Electronic Structure to Stabilize N2-Bridged Dinuclear Complexes Intended for N2 Activation: Iminophosphorane Iron(I) and Cobalt(I). *European Journal of Inorganic Chemistry* **2020,** *2020* (15-16), 1411-1417.
276. Laplaza, C. E.; Cummins, C. C., Dinitrogen Cleavage by a Three-Coordinate Molybdenum(III) Complex. *Science* **1995,** *268* (5212), 861-863.
277. Huss, A. S.; Curley, J. J.; Cummins, C. C.; Blank, D. A., Relaxation and Dissociation Following Photoexcitation of the (μ-N2)[Mo(N[t-Bu]Ar)3]2 Dinitrogen Cleavage Intermediate. *The Journal of Physical Chemistry B* **2013,** *117* (5), 1429-1436.
278. Christian, G.; Stranger, R.; Yates, B. F., A Comparison of N_2 Cleavage in Schrock's Mo[N_3N] and Laplaza–Cummins' Mo[N(R)Ar]$_3$ Systems. *Chemistry – A European Journal* **2009,** *15* (3), 646-655.

279. Hinrichsen, S.; Schnoor, A.-C.; Grund, K.; Flöser, B.; Schlimm, A.; Näther, C.; Krahmer, J.; Tuczek, F., Molybdenum dinitrogen complexes facially coordinated by linear tridentate PEP ligands (E = N or P): impact of the central E donor in trans-position to N2. *Dalton Transactions* **2016,** *45* (37), 14801-14813.
280. Egi, A.; Tanaka, H.; Konomi, A.; Nishibayashi, Y.; Yoshizawa, K., Nitrogen Fixation Catalyzed by Dinitrogen-Bridged Dimolybdenum Complexes Bearing PCP- and PNP-Type Pincer Ligands: A Shortcut Pathway Deduced from Free Energy Profiles. *European Journal of Inorganic Chemistry* **2020,** *2020* (15-16), 1490-1498.
281. Pun, D.; Lobkovsky, E.; Chirik, P. J., Indenyl Zirconium Dinitrogen Chemistry: N2 Coordination to an Isolated Zirconium Sandwich and Synthesis of Side-on, End-on Dinitrogen Compounds. *Journal of the American Chemical Society* **2008,** *130* (18), 6047-6054.
282. Vidyaratne, I.; Gambarotta, S.; Korobkov, I.; Budzelaar, P. H. M., Dinitrogen Partial Reduction by Formally Zero- and Divalent Vanadium Complexes Supported by the Bis-iminopyridine System. *Inorganic Chemistry* **2005,** *44* (5), 1187-1189.
283. Vidyaratne, I.; Scott, J.; Gambarotta, S.; Budzelaar, P. H. M., Dinitrogen Activation, Partial Reduction, and Formation of Coordinated Imide Promoted by a Chromium Diiminepyridine Complex. *Inorganic Chemistry* **2007,** *46* (17), 7040-7049.
284. Holland, P. L., Metal–dioxygen and metal–dinitrogen complexes: where are the electrons? *Dalton Transactions* **2010,** *39* (23), 5415-5425.
285. Peters, J. C.; Cherry, J.-P. F.; Thomas, J. C.; Baraldo, L.; Mindiola, D. J.; Davis, W. M.; Cummins, C. C., Redox-Catalyzed Binding of Dinitrogen by Molybdenum N-tert-Hydrocarbylanilide Complexes: Implications for Dinitrogen Functionalization and Reductive Cleavage. *Journal of the American Chemical Society* **1999,** *121* (43), 10053-10067.
286. Stucke, N.; Weyrich, T.; Pfeil, M.; Grund, K.; Kindjajev, A.; Tuczek, F., Synthetic Nitrogen Fixation with Mononuclear Molybdenum(0) Phosphine Complexes: Occupying the trans-Position of Coordinated N2. In *Nitrogen Fixation*, Nishibayashi, Y., Ed. Springer International Publishing: Cham, 2017; pp 113-152.
287. Hohenberg, P.; Kohn, W., Inhomogeneous Electron Gas. *Physical Review* **1964,** *136* (3B), B864-B871.